The Development and Application of Microanalytical (U-Th)/He Thermochronology

by

Jeremy Welles Boyce

B.S. in Geology, 1997
M.S. in Geochemistry, 2000
University of California, Los Angeles

SUBMITTED TO THE DEPARTMENT OF EARTH, ATMOSPHERIC, AND PLANETARY SCIENCES IN PARTIAL FULFILLMENT OF THE REQUIREMENTS FOR THE DEGREE OF

DOCTOR OF PHILOSOPHY
AT THE
MASSACHUSETTS INSTITUTE OF TECHNOLOGY

FEBRUARY, 2006

Signature of Author:_____
Department of Earth, Atmospheric, and Planetary Sciences
January 11th, 2006

Certified by:_____
Kip V. Hodges
Professor of Geology
Thesis Supervisor

Accepted by:_____
Maria Zuber
E. A. Griswold Professor of Geophysics
Department Head

The Development and Application of Microanalytical (U-Th)/He Thermochronology

by

Jeremy Welles Boyce

Submitted to the Department of Earth, Atmospheric, and Planetary Sciences in partial fulfillment of the requirements for the degree of Doctor of Philosophy in Geochemistry

January 11th, 2005

Abstract

The (U-Th)/He thermochronmeter is the foremost tool available to geoscientists for the purposes of constraining the thermal evolution of the crust below 250°C. However, the potential of the technique is far from fully explored.

The existing *de facto* (U-Th)/He age standard, the fluorapatite of Cerro de Mercado (Durango, Mexico), does not yield reproducible dates, an observation confirmed at several laboratories. A series of experiments combining analytical and numerical techniques suggests that variations in U and Th measured in a single sectioned crystal could result in several percent apparent age variation due to unequal alpha recoil exchange across internal zone boundaries.

Heterogeneities may also play a role in the variability observed in the diffusive behavior of He in strongly zoned minerals, such as monazite. He diffusion experiments on monazite indicate that the closure temperature for (U-Th)/He thermochronometry is between 206°C and 286°C, but varies from grain to grain, even within suites of crystals obtained from one rock. This may be due to compositional variations in the host monazite. Typically heterogeneous monazite crystals may have different closure temperatures, and single crystals may preserve large portions of the cooling history of a rock. None the less, monazite appears to have great potential for (U-Th)/He chronometry, and because of the high U and Th (and therefore ^{4}He) concentrations observed in many monazites, it is a prime candidate for microanalytical (U-Th)/He.

A microanalytical protocol for (U-Th)/He chronometry has been developed by applying the laser microprobe to polished crystals or crystal fragments of monazite. Agreement with conventional (U-Th)/He ages is to within ~1.3%, with previously unavailable spatial resolution of ~30μm. Large numbers of laser microprobe (U-Th)/He ages can be generated more rapidly than by conventional means, and this technique allows the dating of grains that would not be acceptable for conventional (U-Th)/He. Application of laser microprobe (U-Th)/He to monazites from Nanga Parbat, Pakistan, yields highly reproducible cooling ages within and between single crystals. Mean ages of 0.746 ± 0.049 Ma and 0.753 ± 0.036 Ma from two crystals, and the direct observation of negligible (U-Th)/He age gradients, support minimum mean cooling rates of > 325 K/m.y., and minimum mean rock uplift rates of > 4 km/m.y..

Laser microprobe (U-Th)/He of zircon produces no geologically useful dates, a consequence of the poor U and Th measurements provided by LA-ICPMS. Future efforts should employ better calibrated LA-ICPMS approaches or next-generation electron microprobe techniques, which can provide more accurate U and Th concentrations than LA-ICPMS, even for the low concentrations found in zircon.

Thesis Supervisior: Kip V. Hodges
Title: Professor of Geology

Acknowledgements

First and foremost thanks go to Kip Hodges for taking a chance, and admitting me to MIT. Kip also had the vision to attempt laser microprobe (U-Th)/He when the rest of the scientific community was mired in the preconceived notion that it was impossible. I would also like to thank my former advisor, Mary Reid, who encouraged me to apply to MIT even though I didn't want to apply, then encouraged me to visit even though I didn't want to visit, then encouraged me to stay and finish even though I really wanted to leave after my first general exam.

All of the chapters here benefited from the assistance of many people, including but not limited to my excellent coauthors: Kip Hodges, William Olszewski, Michael Jercinovic (University of Massachusetts), Peter Reiners (Yale University), Dan King (Carl Zeiss) and Brian Carpenter (ADE Phase Shift). Many thanks to Terry Plank (Boston University) for her generous allotments of time on the LA-ICPMS. Terry's cohorts (Jennifer Wade, Linda Farr, and Louise Bolge) also were of great assistance in making and interpreting U and Th data gathered at Boston University. At MIT, the contributions of Julia Baldwin, Sam Bowring, Neel Chatterjee, Jim Crowley, Jahan Ramezani, and Mark Schmitz are greatly appreciated. Megan Andrews (Yale) also contributed to this effort, and her unrewarded effort is greatly appreciated.

The time-integrated noble gas research group at MIT (Arthur White, José Hurtado, Karen Viskupic, Cameron Wobus, Kate Ruhl (Huntington), Ryan Clark, Taylor Schildgen and Malcolm Pringle, as well as the aforementioned Hodges and Olszewski) are thanked for so many different contributions that I can't even begin to name them all. But you folks are great, and without you I would never have finished. I entered MIT with a spectacular class of scientists, and their support has been instrumental in my surviving two General Exams and more than five years of late nights, and zero-day weekends, with far too few beers at the Muddy in between. Special thanks to Maureen Long for introducing me to my wife, in addition to being a great friend. Go Sox!

Many thanks to Phi Delta Theta for years of entertainment, "free" lodging, and brotherhood (even though I could never join, you guys always treated me like a brother, and I will never forget that).

I have received support from my wonderful family, as well as my "second family" of great friends from high school and UCLA: Brett, Ann, J.T., Lauren, David, Amy, Julie, Tim, Carrie, Joel, Garrett, Jorge, Kari, Jon, Frank(s), Kurt, Liz, Doug, Mike(s), R.J. ... you are all awesome. There's no other way to put it.

Music is a big part of my life, so thanks must also go out to the many bands that have kept me going through the years: The Clash, Social Distortion, The Ramones, Bad Religion, The Damned, Stiff Little Fingers, The Swingin' Utters, Rancid, NoFX, Flogging Molly, U.S. Bombs, Throw Rag, Brain Failure, The Dropkick Murphys, Good Riddance, The Pogues, Youth Brigade, The Descendents, Me First and the Gimme Gimmes, and The Bouncing Souls. Special thanks go out to Bob Dylan and Johnny Cash for being so damn punk before punk even existed, and for not caring whether they were punk or folk or country or neither or both.

And finally, thank you to my lovely wife Caroline. You are my sunshine.

To my parents, the four most inspirational people I have ever met.

Table of Contents

Introduction

The chronometry of geologic processes, and the relationship between that chronometry (as derived from isotope geochemistry) and the thermal state of the rocks being studied is fundamental to the the study of the evolution of the near-surface regime of our planet. Geochronometers based on isotope decay provide the widest range of temporal constraint available, from 10^1 to more than 10^9 years, and in combination with diffusion theory allow us to constrain the thermal evolution of many geologic regimes. There are many mineral-isotope systems that contribute to our knowledge of the thermal evolution of the mantle and crust, over a range of more than 700 K. The low-temperature end of the thermal spectrum (< 250 °C) is constrained by the (U-Th)/He thermochronometer, which takes advantage of the production of ^{4}He by alpha decay of U, Th, and Sm in common accessory minerals such as apatite (nominal closure temperature of ~ 70 °C; Farley 2000), titanite (~ 200 °C; Reiners and Farley, 1999), and zircon (~ 200 °C; Reiners 2005). (U-Th)/He thermochronometry now produces the most robust constraints on the low temperature evolution of both mountain ranges and basins alike, but it was a hard-won victory that took over 100 years. In the following chapters, my co-authors and I contribute to the continuing development of the (U-Th)/He chronometer. In particular, this thesis includes the results of the first attempts to use laser microprobe technology in (U-Th)/He chronometry.

One of the greatest problems facing (U-Th)/He thermochronometry is the inability of many laboratories to accurately reproduce ages determined for the Durango apatite standard within the analytical precision of the technique. This not only makes interlaboratory calibration difficult, but also limits the confidence one can have in the analyses of unknowns. In Chapter 1 (coauthored with my advisor, K.V. Hodges), we explore one possible source of error: as a

consequence of U and Th zoning, the recoil redistribution of ^{4}He may lead to local changes in parent/daughter ratios that may result in variable apparent ages for crushed fragments from a single crystal of Durango fluorapatite. Areas with low concentration may receive excess ^{4}He from neighboring zones with high U and Th concentrations, while zones with high U and Th may be depleted in ^{4}He. When the grain is broken, individual pieces of the crystal might therefore have too much or too little ^{4}He for the amount of U and Th in each fragment, and thus might yield erroneous (U-Th)/He dates. In order to test this hypothesis, we measured U and Th variations in a Durango megacryst, then used numerical techniques to simulate thousands of virtual fragment analyses. Although measured U and Th variations cannot explain the age deviations reported from all laboratories in their entirety, U and Th zoning is a likely cause of much of the discrepancy. As the effect of zoning is greater for smaller fragments, it will become an even more significant problem as we move towards analyzing ever smaller fragments or ablation pits, as described in Chapter 3.

A mineral that has not yet received as much attention as apatite, zircon, and titanite for (U-Th)/He thermochronology is monazite. Although typical monazites are small (~100μm), they are also very rich in U, Th, and Sm - in some cases containing weight percent concentrations of those elements. In Chapter 2 (coauthored with K.V. Hodges, W.J. Olszewski, and M.J. Jercinovic at the University of Massachusetts, Amherst), we describe experiments designed to determine the rate at which ^{4}He diffuses from monazite crystals, and, in turn, the effective closure temperature for (U-Th)/He of monazite. Three single-crystal diffusion experiments on the 554 monazite (a UCLA SIMS standard from Arizona, USA) yield three sets of Arrhenius parameters than are statistically distinguishable from one another. The data, when combined with nominal grain sizes and cooling rates yield closure temperatures that range from 206 °C to

286 °C. The variation from grain to grain within a single aliquot suggests that the diffusion of ^{4}He in monazite is not as simple as other (U-Th)/He systems. Possible causes of the variation in He diffusivity are explored, in particular the role of monazite composition on He diffusivity, in as much as the 554 monazite displays strong compositional zoning.

The potential influence of compositional heterogeneities in (U-Th)/He of monazite, combined with the small size of typical monazites suggests that the best way to determine (U-Th)/He cooling ages on monazite may be to apply a microanalytical technique. In Chapter 3 (coauthored with K.V. Hodges, W.J. Olszewski, N. Chatterjee, B.D. Carpenter at ADE Phase Shift, M.J. Jercinovic at the University of Massachusetts - Amherst, and P.W. Reiners at Yale University), we discuss the first application of the laser microprobe to (U-Th)/He chronometry, using grains of gem quality monazite from Brazil. Compared to the conventional laser-heating (U-Th)/He closure age of 449.6 ± 9.8 Ma (2SE), laser microprobe (U-Th)/He yields an indistinguishable cooling age of 455.3 ± 3.7 Ma (2SE) for this material. The total variation from the mean is observed to always be less than 7%, a reproducibility similar to previous conventional (U-Th)/He applications. Laser microprobe (U-Th)/He can be used to date large numbers of grains in a short amount of time, which will promote acquisition of large datasets for detrital thermochronology studies, and make it more likely that researchers will attempt to reproduce individual analyses. Laser microprobe (U-Th)/He will also enable us to date "ugly duckling" (broken, included, abraded, or malformed) grains, which are not amenable to conventional analyses because of more stringent requirements. Finally, in the near future, it should be possible to measure ^{4}He depth profiles in single unpolished crystal faces, which can be inverted to constrain cooling histories.

Chapter 4 (coauthored with K.V. Hodges, D. King at Zeiss Instruments, J.L. Crowley, M.J. Jercinovic, N. Chatterjee, S.A. Bowring, and M. Searle at Oxford University) details an application of laser microprobe (U-Th)/He to monazite from Nanga Parbat, Pakistan. Nanga Parbat has been the focus of many thermochronometric studies, but to date no one has ever published (U-Th)/He data on rocks from the massif. High cooling rates and young cooling ages have long hinted at very rapid rock uplift rates for rocks from Nanga Parbat (Zeitler et al. 1993; Hubbard et al. 1995; Winslow et al. 1996; Treloar et al. 2000), but much of the low-temperature thermochronology is within uncertainty of zero age (i.e. 0.5 ± 0.5 Ma). In this study, we demonstrate the ability to determine precise cooling ages for very young monazites. Two monazite crystals with ~1.5 Ma crystallization ages yield 7 and 14 cooling ages per crystal, with indistinguishable weighted mean dates (0.746 ± 0.049 Ma and 0.753 ± 0.036 Ma, 2σ). Taken together, the two crystals yield a single weighted mean cooling age of 0.748 ± 0.019 Ma (2.5% at 2SE). This is the most precise low-temperature cooling age ever determined for Nanga Parbat, and is also the first time that the intracrystalline spatial distribution of ^{4}He has been directly measured. As important as the high precision of the result is the fact that no diffusion gradients are observed in the monazites. In conjunction with the diffusion data described in Chapter 2, this allows us to constrain the minimum mean cooling rate (~325-375 K/m.y.) experienced by these crystals. Presuming a maximum mean geothermal gradient (~ 100 K/km) for Nanga Parbat (Winslow et al. 1994), we can calculate a minimum estimate for mean rock uplift rate over the last ~750 ka of > 4 km/m.y.

Finally, in Chapter 5 (coauthored by K.V. Hodges, W.J. Olszewski, B.D. Carpenter at ADE Phase Shift, and J.M. Hanchar at Memorial University, Newfoundland) we describe the first attempts to date the mineral zircon by laser microprobe (U-Th)/He. Four zircons suites were

chosen, three having well-constrained crystallization ages from ~200 to ~2000 Ma. The fourth is less well-dated, with an approximate age of ~ 0.5 Ma. The (U-Th)/He dates from this study were inconsistent, and strongly dependent on the protocols used to generate and reduce the U and Th data used to produce the (U-Th)/He dates. Three key factors have been identified as important to obtaining precise and accurate U and Th concentrations via LA-ICPMS. First, the use of Zr as an internal standard is not recommended, as U and Th values generated with Hf as the internal standard resulted in dates that were far more consistent with predicted (U-Th)/He ages. Second, the use of NIST standard glasses may be in part responsible for the general trend of U and Th concentrations resulting in (U-Th)/He dates that are too young. Homogeneous minerals standards, while difficult to obtain, may be worth locating, or synthesizing, if possible. Finally, attempting laser microprobe (U-Th)/He on strongly zoned crystals such as many zircons requires careful placement of both the He ablation pit and the subsequent U and Th laser pit. Laser microprobe (U-Th)/He of zircon is technically feasible, but successful application will require the development of a better analytical protocols for U and Th microanalysis, which will yield more accurate and precise concentration measurements.

Chapter 1 of this thesis was published last year: Boyce and Hodges (2005). *U and Th zoning in Cerro de Mercado (Durango, Mexico) fluorapatite: Insights regarding the impact of recoil distribution of radiogenic ^{4}He on (U-Th)/He thermochronology.* Chemical Geology, v. 219, pp. 261-274. Chapter 2 is now published as: Boyce J.W., Hodges K.V., Olszewski, W.J., and Jercinovic, M.J. (2005). *He diffusion in Monazite: Implications for (U-Th)/He thermochronometry.* Geochemistry, Geophysics, Geosystems, v. 6, Q12004, doi: 10.1029/2005GC001058. Chapter 3 is currently in review at Geochimica Cosmochimica Acta. Chapter 4 is in the final stages of preparation to be submitted to a short-format journal in early

2006. Chapter 5 is considered to be a major step towards being able to date zircons by laser microprobe (U-Th)/He but is not intended for publication.

References

Boyce, J. W. and K. V. Hodges (2005). "U and Th zoning in Cerro de Mercado (Durango, Mexico) fluorapatite: Insights regarding the impact of recoil redistribution of radiogenic ^{4}He on (U–Th)/He thermochronology." Chemical Geology **219**: 261-274.

Boyce, J. W., K. V. Hodges, et al. (2005). "He diffusion in monazite: Implications for (U-Th)/He thermochronometry." G-Cubed **6**(Q12004).

Farley, K. A. (2000). "Helium diffusion from apatite; general behavior as illustrated by Durango fluorapatite." Journal of Geophysical Research, B, Solid Earth and Planets **105**(2): 2903-2914.

Hubbard, M. S., D. A. Spencer, et al. (1995). "Tectonic exhumation of the Nanga Parbat Massif, northern Pakistan." Earth and Planetary Science Letters **133**(1-2): 213-225.

Reiners, P. W. (2005). Zircon (U-Th)/He thermochronometry. Thermochronology: Reviews in Mineralogy and Geochemistry. P. W. Reiners and T. A. Ehlers. Washington, D.C., Mineralogical Society of America. **59:** 151-179.

Reiners, P. W. and K. A. Farley (1999). "Helium diffusion and (U-Th)/He thermochronometry of titanite." Geochimica et Cosmochimica Acta **63**(22): 3845-3859.

Treloar, P. J., D. C. Rex, et al. (2000). Geochronological constraints on the evolution of the Nanga Parbat syntaxis, Pakistan Himalaya. Tectonics of the Nagna Parbat syntaxis and the western Himalaya. M. A. Khan, P. J. Treloar, M. P. Searle and M. Q. Jan. London, UK, The Geological Soceity of London. **170:** 137-162.

Winslow, D. M., P. K. Zeitler, et al. (1994). "Direct evidence for a steep geotherm under conditions of rapid denudation, western Himalaya, Pakistan." Geology (Boulder) **22**(12): 1075-1078.

Winslow, D. M., P. K. Zeitler, et al. (1996). "Geochronologic constraints on syntaxial development in the Nanga Parbat region, Pakistan." Tectonics **15**(6): 1292-1308.

Zeitler, P. K., C. P. Chamberlain, et al. (1993). "Synchronous anatexis, metamorphism, and rapid denudation at Nanga Parbat (Pakistan Himalaya)." Geology (Boulder) **21**(4): 347-350.

CHAPTER 1

U and Th zoning in Cerro de Mercado (Durango, Mexico) fluorapatite: Insights regarding the impact of recoil redistribution of radiogenic ^{4}He on (U-Th)/He thermochronology

Boyce, J. W., and Hodges, K. V.

As published in:

Chemical Geology, volume 219 (2005), pages 261 - 274

ABSTRACT

Fluorapatite from Cerro de Mercado, Durango, Mexico has been used in several important diffusion studies aimed at calibrating the closure temperature of the (U-Th)/He apatite thermochronometer and has become a *de facto* standard for (U-Th)/He laboratories. Nevertheless, replicate laser fusion analyses of small crystal fragments of the "Durango fluorapatite" typically yield a range of (U-Th)/He dates that cannot be explained by reported analytical imprecision alone. Laser ablation ICPMS measurements of U and Th of a section cut through a representative crystal of Durango fluorapatite (perpendicular to the **c** axis) reveal the existence of significant zoning in these elements. Since alpha-stopping distances in apatite are comparable to the scale of this zoning, the ejection of radiogenic ^{4}He from one zone to another may explain some of the reported fragment-to-fragment variation in (U-Th)/He dates. Two-dimensional numerical models of the recoil redistribution of ^{4}He in a crystal with the zoning we observed lead to predicted age variations of several percent for fragments with sizes and aspect ratios typical of those used for laser-fusion of Durango fluorapatite. It is likely that large crystals (or large aliquots of small fragments) of zoned materials may be acceptable as "bulk" interlaboratory standards. However, the current trend is toward the use of smaller and smaller sample sizes, including broken crystals, for (U-Th)/He thermochronology. Our work indicates that heterogeneities in the U and Th concentrations of such samples are a serious concern, so much so that high-precision (U-Th)/He geochronologic studies should include a concerted effort to characterize the the extent of U and Th zoning in analyzed crystals.

Introduction

For the (U-Th)/He geochronometer, the most commonly chosen standard is the fluorapatite of Cerro de Mercado, Durango, Mexico (here referred to as the Durango fluorapatite). Because the Durango fluorapatite is relatively free of inclusions, and because crystals in excess of a centimeter in diameter are easily obtained, Zeitler et al. (1990), Wolf et al. (1996), and Farley (2000) selected this material for their landmark studies of the diffusion of helium in apatite. Their results demonstrate straightforward and reproducible diffusive behavior of ^{4}He in the Durango fluorapatite, which suggests that the material should be a suitable interlaboratory standard. However, conventional furnace and laser fusion (U-Th)/He dating of small (~180 μm) fragments of crystals of Durango fluorapatite yield apparent ages that vary by more than 8% (House et al. 2000). This variability, at least a factor of two greater than might be expected to result from analytical uncertainty, implies that crystals of the Durango fluorapatite are heterogeneous in U, Th, He, or some combination of the three elements.

One possible explanation for this behavior — that the crystals contain diffusive loss gradients in ^{4}He related to slow cooling after crystallization — can be dismissed given the volcanic origin and subsequent geologic history of the Durango deposit (Young et al. 1969). Another possibility is that the apparent age variation is related to the preferential loss of radiogenic ^{4}He from the rims of crystals through alpha particle ejection (Farley et al. 1996). This also seems improbable because (U-Th)/He studies of Durango fluorapatites typically involve the removal of crystal margins prior to crushing the material into fragments for analysis. Instead, the most likely possibility is that there are significant intragranular variations in uranium and/or thorium in Durango fluorapatites. As it happens, the Durango fluorapatite is highly zoned — in some cases strongly enough to be visible to the naked eye. If the chemical variations causing

this zoning extend to U and Th, then this might compromise the integrity of (U-Th)/He ages measured on small fragments of these megacrysts.

Figure 1 illustrates how U+Th zoning might lead to inconsistencies in measured (U-Th)/He ages for crystal fragments from any zoned crystal. The two shaded fields represent adjacent zones of a crystal, one with higher U+Th than the other. With time, radioactive decay should produce a higher concentration of ^{4}He in the zone with more U+Th than in the zone with less U+Th. If the two zones are closed systems, then (U-Th)/He analysis of each should yield the same age. However, two processes act to redistribute ^{4}He in the crystal: 1) diffusive transfer driven by the concentration gradient across the boundary between the two zones; and 2) alpha ejection across the boundary. Both processes would result in higher concentrations of ^{4}He in the low-U+Th zone (and lower concentrations of ^{4}He in the high-U+Th zone) than would be expected from *in situ* decay. The probability of alpha particle ejection per event from the left-hand zone to the right-hand zone in Figure 1 is equal to that from the right-hand zone to the left-hand zone, but the higher concentration of U+Th in the left-hand zone means that the net effect of alpha ejection would be to produce additional unsupported or "excess" ^{4}He in the low-U+Th zone and a deficiency of ^{4}He in the high-U+Th zone. Thus, both ^{4}He redistribution mechanisms would lead to an anomalously old (U-Th)/He age for the low-U+Th zone and an anomalously young (U-Th)/He age for the high-U+Th zone. The age differences for fragments of crystals zoned in U and/or Th would depend on: 1) the post-crystallization thermal history of the crystal (since diffusion is a temperature-dependent process); 2) the scale of the zoning; 3) the size distribution of the fragments; 4) the orientation of fragments (with respect to the zoning); and 5) the magnitude of variations in U and Th concentration.

Of course, this problem would not be limited to the Durango fluorapatite, but rather would affect the parent/daughter ratios of any zoned material. In order to test the hypothesis that (U-Th)/He age differences for crystal fragments could result from U+Th zoning, we have performed a geochemical investigation of single, large crystals of the Durango fluorapatite at the sub-grain scale using backscattered electron (BSE) and x-ray elemental (XRE) mapping and *in situ* laser-ablation inductively coupled mass spectrometry (LA-ICPMS). Our LA-ICPMS results demonstrate the existence of nearly 50% variability in U and over 60% variability in Th in a single crystal of Durango fluorapatite. Qualitative x-ray mapping of other crystals strongly suggests that this magnitiude of chemical zoning is characteristic of the material in general. We used the observed spatial variations in U and Th in the well-characterized sample to model the consequence of He redistribution on measured ages of fragments derived from crystals with such zoning, concentrating on the effects of alpha ejection since Durango fluorapatite cooled so rapidly that diffusional redistribution should be negligible. The results indicate that the alpha ejection process alone can account for up to eight percent variation in apparent ages of Durango fluorapatite fragments, but not as great of a mean variation as that reported by House (2000). Furthermore, the possibility that zoning of this magnitude is present in crystals of unknown age and thermal history suggests that material characterization should be emphasized in all future (U-Th)/He studies.

Analytical Studies

Our work focused on four sections, cut perpendicular to the **c** axis, from four distinct large (5-10mm), yellow crystals of Durango fluorapatite. Each section was mounted in epoxy, and polished flat using standard procedures. XRE maps were prepared for Si, Cl, F, Th, and U

using a JEOL JXA-733 Superprobe at MIT. Analytical conditions were as follows: accelerating voltage - 15 kV; beam current - 20 nA; dwell time - 30 ms/pixel. Using these settings, each set of maps took about ten hours to complete. Additional Y, Si, Cl, F, Ca, and Th XRE maps were made at the University of Massachusetts, Department of Geosciences Electron Microprobe/SEM Facility using the same accelerating voltage but a much higher beam currrent (~350 nA) and longer dwell time (145 ms/pixel). The additional dwell time increased the total time necessary to produce each map to more than twenty hours.

In order to quantify spatial variations in the concentrations of U and Th, we selected one of the sections for detailed study using the LA-ICPMS facility at the Department of Geological Sciences at Boston University. Laser ablation was accomplished by focusing a frequency-quintupled Nd-YAG laser, (λ = 213 nm), on the sample surface. The laser was operated with 20 or 100 μm spot sizes, and 40% or 60% output at 10 Hz. Microscopic observation showed that the resulting ablation pits are conical, with circular surface expressions of approximately 35 to 100 μm. The ablated material was carried into the plasma source for ionization with an Ar-gas stream. In addition to U and Th, a number of other elements were analyzed: Ca (for internal standardization), Fe and Ti (for the potential correction for contamination by Fe oxide inclusions), and the trace elements Dy, Sm, and Sr (Table 1). All analyses were externally standardized to the National Institute of Standards and Technologies (NIST) glass 612, with the standard reanalyzed after every 5 unknowns to account for drift. Concentration errors are reported throughout this paper at the 2σ level and represent propagated analytical errors and uncertainties in standard compositions.

Analytical Results

Backscattered Electron and X-ray Elemental Maps

For many minerals, BSE imaging is a powerful tool for revealing compositional heterogeneities that produce variations in mean atomic weight. Unfortunately, subtle zoning in U and Th in a REE-rich mineral like apatite produces such little variation in mean atomic weight that BSE methods yield useful images of such zoning in only a few cases. Some of the Durango fluorapatite sections we studied displayed faint, concentric, zoning. In apatite, growth zoning in REE might be the primary cause of such variations in mean atomic weight, and therefore other qualitative and quantitative methods are necessary to establish the potential role of U and Th in BSE zoning.

High-resolution XRE maps of U and Th would be most desirable in this regard, but the concentrations of both elements are so low in Durango fluorapatite (Young et al. 1969) that little information can be gleaned from such maps. Figure 2a, for example, shows a Th map of one section. Although faint suggestions of zoning are present in the image, substantial variations may be masked by the low sensitivity of the technique. The data of Bea and Montero (1999) and others suggest that the distribution of yttrium (Y) can serve as a proxy for the distribution of U in apatite. The relatively high abundance of this element in the Durango material prompted us to create Y maps for all analyzed sections. We postulate that Si may be a similarly useful proxy for Th because Si is involved in a substitution mechanism that is plausibly responsible for the incorporation of Th into the apatite structure: $Th^{4+} + Si^{4+} \Leftrightarrow REE^{3+} + P^{5+}$ (Nekrasov 1973).

Figure 2b shows the pattern of Si variations in a representative section of Durango fluorapatite. While the Y maps show generally concentric, oscillatory zoning on the scale of tens to hundreds of micrometers, zoning within this crystal is most clearly expressed in the Si map. Three domains may be identified: 1) an apparently homogeneous, slightly off-center core region

(≤ 35% of the crystal section by area); mantled by 2) a domain that is relatively enriched in these elements, but which exhibits strong oscillatory zoning; rimmed by 3) a relatively depleted zone with weaker oscillatory zoning. There is a distinct angular discontinuity between the first and second domains, which may be the result of intersection of a termination face with the *c*-parallel prism faces. Similar relationships have been observed in BSE, Y, or Si maps for the other crystals of Durango fluorapatite that we have studied. XRE maps of chlorine (and to a lesser extent, fluorine) display a consistent zoning pattern, but calcium maps show no discernable variations.

LA-ICPMS Trace Element Abundances

Elemental abundances determined by LA-ICPMS are shown in Table 1. Uranium and thorium concentrations varied across the sample section in a systematic way which correlated well with Y and Si zoning as revealed by XRE analysis. The core, intermediate, and rim domains of the crystal have U compositions ranging from 11.0-12.6 ppm, 10.1-15.0 ppm and 10.9-12.0 ppm, while Th concentrations were found to be 278-312 ppm, 245-329 ppm, and 203-219 ppm, respectively. Minor inconsistencies in the correlation between the U and Th concentrations and the Si and Y maps occurred near domain boundaries and in regions of fine-scaled growth zoning. These discrepancies are most likely due to the three-dimensionality of the zoning and the limited spatial resolution of the laser microprobe, which was imposed by the need to ablate sufficient material to obtain a measurable signal.

Overall, the ranges of U and Th concentrations measured by LA-ICPMS (10.1-15.0 ppm and 203-329 ppm, respectively) are of similar magnitude to the variations observed by Young et al. (1969) in bulk sample U and Th analyses of Durango fluorapatite (9.7-12.3 ppm and 167-238

ppm). The slightly higher absolute concentrations of U and Th measured in our study may reflect intercrystalline variability or, potentially, our use of a silicate glass rather than a crystalline phosphate for external standardization. Regardless, the data demonstrate significant variability in U and Th in a single crystal of Durango fluorapatite. We have explored how these variations may impact the apparent (U-Th)/He ages for fragments of Durango fluorapatite through the development of a two-dimensional numerical alpha-recoil model.

Numerical Experimentation

Model Parameters

The steps involved in developing our numerical experiment are illustrated in Figure 3. We began by creating a synthetic map of the distribution of U and Th of a crystal of Durango fluorapatite. Since the spatial resolution of the LA-ICPMS was inadequate to constrain fully the distribution of U and Th, we assumed that measured counts per second of Si for each pixel on the XRE map was correlated to the concentration of Th at the position of that pixel (Figure 3a,b). Counts per second of Si were translated to parts per million of Th with a calibration algorithm based on Th concentrations measured by LA-ICPMS for relatively broad regions of the section with little fine-scale oscillatory zoning (Figure 3c). This process involved processing a 16-bit grayscale Si map in Adobe Photoshop™ in order to bring out contrast in the original image. The resulting image was smoothed (mean values for each zone were used to eliminate the random noise inherent in XRE maps) and resampled at a scale of 1μm per pixel for modeling purposes. Because Th/U ratios implied by our ICPMS data vary by only a factor of two, we assumed a constant Th/U ratio (25:1) to make a conversion from Si intensity to U+Th content. Using this

Th/U ratio, ~85% of the radiogenic ^{4}He produced in this material over the past 32.1 million years (Farley et al. 1995) comes from the ^{232}Th decay series.

The next step in our analysis involved extracting a ~2mm region of the resulting U and Th maps for numerical modeling (Figure 3d). This was done because, as we describe below, the modeling is computationally intensive, and the size of modeled fragments is much smaller than the size of the sample. As a consequence, modeling the entire grain would have been prohibitively time consuming. Nevertheless, the region chosen for study is representative of the nature of zoning over the entire grain, as the extracted region and the entire crystal section have approximately the same ratio of highly zoned and unzoned areas.

Using the U+Th distribution map for this region (Figure 3e), we then created a map of ^{4}He. After a period of 32.1 million years, each element in the matrix would have produced a proportional abundance of ^{4}He. However, the recoil process would have redistributed these a particles an average distance of 22μm away from their point of origin assuming a 25:1 Th/U ratio (Farley et al. 1996). While this process is stochastic in nature, the large number of decays that would occur over 32.1 million years would lead to an essentially uniform broadcast of ^{4}He in all directions. We modeled this by redistributing the radiogenic ^{4}He in our synthetic matrix uniformly among the elements lying ~22 μm from the element of origin (the average likely distance for an alpha particle to travel due to ejection). Thus, the ^{238}U, ^{235}U, and ^{232}Th abundances at any given position in the crystal are governed by the primary zoning structure, but the ^{4}He abundance at that position depends on the integrated ^{238}U, ^{235}U, and ^{232}Th abundances in the surrounding region. As a consequence, the (U-Th)/He age for that position will be different from 32.1 Ma. Note that a proportion of the ^{4}He produced at nodes $\leq$ 22 μm from the margin of the grid leaves the system altogether, as is the case in nature (Farley et al., 1996). Fragments

containing these points are omitted from the model results to simulate the common practice of removing alpha-depleted margins of large crystals of Durango fluorapatiite prior to crushing them into fragments for (U-Th)/He analysis. Our assumption that all alphas travel exactly 22μm does not reflect the three-dimensionality of the problem; helium generated above or below the plane of interest could be ejected into this plane, and some alpha particles within the model plane would be lost to other parts of the crystal. As we discuss in Section 5.2, it is difficult to know what impact this would have on the net redistribution of ^{4}He in the modeled plane with out a better knowledge of the nature of zoning in the third dimension.

The next step in the modeling process involves "breaking" the two-dimensional matrices into domains that simulate the small fragments used for laser-heating (U-Th)/He analysis (Figure 3f). We were guided in our choice of the geometry of these domains by studying fragments of Durango fluorapatite from a standard aliquot prepared at the California Institute of Technology and provided to us by P. Reiners (Yale University). When a representative sample from this aliquot is sprinkled on a glass slide and observed under a microscope, most fragments have an irregular shape, defined (rarely) by the poor cleavages [0001] and [101bar0], and (more commonly) by the conchoidal fracture of apatite. Their shapes can be modeled reasonably well in two dimensions as parallelograms. Many grains had an approximate long dimension of 180 µm, (similar to those in the aliquot used by (Farley 2000) but observed sizes ranged from ~ 50 µm to ~ 400 µm. Aspect ratios varied widely, from 1:1 to about 10:1, This range is undoubtedly a minimum because fragments sprinkled on a slide preferentially lay on a more elongate side, and thus commonly the shortest axial length is perpendicular to the stage. Observations of the grains under crossed polars indicate no obvious correlation between elongation direction and crystallographic orientation.

Our first model was run assuming parallelogram-shaped, two-dimensional fragments, each with a long dimension of 180 μm and an aspect ratio of 4:1. A set of 5000 randomly oriented parallelograms of this size and shape were extracted (in a virtual sense) from the matrix of parent/daughter ratios, and were used to calculate a (U-Th)/He age for that "virtual fragment" Finally, the 5000 dates were used to determine a frequency distribution of apparent ages (Figure 3g) that would represent the domain depicted in Figure 3d.

Numerical Results

The 5000 fragments generated in each of our numerical experiments yielded parent and daughter elemental abundances corresponding to apparent ages ranging from 31.1 to 33.4 Ma, with a mean of 32.1 Ma (Figure 4). The distribution of dates about the mean is highly kurtotic and does not resemble a Gaussian, or normal, distribution; as a consequence, the familiar "standard deviation" is a rather poor description of distribution about the mean. Instead, we rely on the mean average deviation (MAD), which is not model-dependent (Press et al. 1992). For this experiment, the MAD is 0.07 Ma., or about half the conventional standard deviation (Table 2).

The correspondence of the mean age with the accepted age of Durango fluorapatite, not to mention the very small MAD of the distribution, implies that laser-heating (U-Th)/He analysis of many (e.g., 5000), average (e.g., 180 x 45 μm) fragments of Durango fluorapatite should yield consistent ages with a small uncertainty. However, the synthetic distribution in Figure 4 includes individual fragments with ages as much as 1.25 Ma different from the accepted age. As a consequence, the likelihood of a set of laser-heating experiments reproducing the accepted age with high fidelity should depend critically on the number of fragments in the set. For example,

House et al., (2000) analyzed 27 fragments of Durango fluorapatite in their study which resulted in an age range with a standard deviation that exceeded nominal analytical imprecision by more than 6%. Could this result have been a consequence of analyzing a small set of fragments from a crystal of Durango fluorapatite that was strongly zoned in U and Th? If the level of zoning we observed in our study is characteristic of Durango fluorapatite in general, the answer is probably no. When we simulated 5000 sets of fragments of comparable size to those used in the House et al. (2000) study, selecting each at random from the population in Figure 4, we found no sets with standard deviations as high or higher than that observed by House and co-workers. According to the model results, the analysis of fewer than five fragments is necessary to increase the expected imprecision to this level. As discussed further below, additional factors must contribute to the discrepancy between the measured and predicted deviations.

Sensitivity analysis

In order to evaluate the sensitivity of the result to model assumptions, we also ran models with parallelogram-shaped fragments ranging from 400 μm to 50 μm in long dimension while maintaining a 4:1 aspect ratio. Another set of models were run at a fixed long dimension of 180 μm and aspect rations ranging from 1:1 to 16:1. One set of numerical experiments was done assuming a rectangular fragment shape with a 4:1 aspect ratio at length of 180 μm and a width of 45 mm. so that we could explore the effect of a different fragment geometry on the frequency distribution. This shape has a smaller perimeter/area ratio than a 180 μm long parallelogram, representing a different surface area/volume ratio for real three-dimensional fragments.

The effects of such changes in model assumptions are shown in Table 2. MAD values range from 0.03 to 0.18 Ma for different-sized grains with a fixed aspect ratio of 4:1, while

varying the aspect ratio from 1:1 to 16:1 only results in a change in MADs from 0.03 to 0.09 Ma. Maximum observed error values also increase in a similar manner, from 0.22 Ma (300x300μm) to 2.9 Ma (50x12μm). Maximum errors correlate strongly (and inversely) with the minimum dimension of the fragment, with 180μm long fragments displaying nearly the complete range of observed maximum error values seen in the constant aspect ratio models: While 180 x 180 μm fragments have a maximum age dispersion of 0.35 Ma (1.1%), ages for 180 x 11 μm pieces of Durango range to 2.6 Ma (8%).

It is clear that fragment shape, as well as the scale and magnitude of zoning have a measurable impact on the model results. Predictably, rectangular fragments are less prone to age variations than parallelograms, while increasing the scale and magnitude of parent element zoning increases the width of the age distributions produced. Changing the grain shape from parallelograms to rectangles insignificantly decreases the MAD from 0.07 to 0.05 Ma. A similar decrease from 1.25 to 0.87 Ma is observed in the maximum errors, while the population with deviation > 1% decreases by less than a factor of 2. Decreasing the scale of zoning by a factor of two results in a small increase in MAD (0.07 to 0.09 Ma) and an increase in maximum dispersion (1.25 to 1.65 Ma). Further decreasing the scale of zoning by another factor of two increases the MAD to 0.14 Ma, but decreases the maximum error to 1.45 Ma.

Doubling the parent element contrast within the sample grain doubles the MAD to 0.15 Ma, while the maximum error observed increases by more than a factor of three (1.25 to 3.88 Ma). Further increases in the contrast of the parent-element zoning result in further increases in the MAD, standard, and maximum deviations. At extreme values, fragments with extremely low U and Th contents result in unreasonable model ages (> 1 Ga).

It is more difficult to assess the impact of out-of-plane alpha redistribution on our model results. If we make the simpest assumption that all zoning in Durango fluorapatite is perpendicular to the **c** axis direction, it would be possible to create a three-dimensional model similar to the two-dimensional model discussed here. Although we have not done this full experiment, the impact on apparent alpha redistribution in a two-dimensional, **c**-perpendicular section would be analogous to a decrease in the mean ejection distance for alpha particles in two dimensions. (To understand why this would result in an apparent decrease, rather than an increase, note that while most alpha particles ejected from a U or Th site on the plane leaves the two-dimensional section, many more arrive on the plane from surrounding regions.) In a semi-quantitative sense, modeling this effect as the intersection of spherical "ejection volumes" on a single **c**-perpendicular section is the same as decreasing the average ejection distance in two dimensions from 22 μm to approximately 17 μm. The effect of this on our model would be to reduce the MAD from 0.07 to 0.04, and the 1% population threshold to approximately one-half the value derived from modeling with a 22μm ejection length.

5.3 The Probability of Measuring Incorrect Dates

The recognition that U and Th zoning can impact significantly the apparent ages of Durango fluorapatite fragments has important implications for how we design (U-Th)/He studies of less well-characterized samples. Suppose a rock sample of interest contains relatively large crystals that are broken during sample crushing. Even if these apatites exhibit fine-scale U+Th zoning, analysis of a large aliquot of fragments should yield the "correct" (U-Th)/He age. However, the analysis of single crystal fragments using increasingly popular laser-degassing

approaches House et al., (2000) could lead to spurious results unless a large number of grains were analyzed and the results combined statistically. A valuable way to think about the magnitude of this problem is to ask the question: what is the likelihood (in a statistical sense) of analyzing a fragment with an unacceptably high deviation from the "correct" age? In this section, we illustrate how this might be done using our model results.

In any of our model populations, dates can be classified as "good" or "bad" by defining some threshold beyond which a date is unacceptably different from the mean. It is possible to then calculate the probability that a particular number of "bad" dates would be encountered in any sub-sampling of the population. We have done this for three cases: 180x45μm (4:1), 180x11μm (16:1), and 50x12μm (4:1). The first two cases were chosen because they represent reasonable fragment geometries for typical fragments of Durango fluorapatite used for geochronology, while the last was chosen assuming that the smallest dimension of real fragments, which is difficult to observe, is four times smaller than the intermediate value observed. The calculated probability of drawing a single unacceptable date is shown for 0.5%, 1%, and 2% thresholds in Figure 5. The odds of encountering one fragment with $\geq$ 0.5% dispersion from the true age decreases with increasing grain dimension, with small fragments having a nearly 100% probability of at least one "failure" after only ~20 shards are run. For the same probability of encountering a "bad" date, the number of 180μm long fragments required increases to sixty. The number of fragments necessary for a given odds of failure increases for 1% and 2% thresholds, as would be expected. In the course of running 100 samples, even 180x45 μm fragments, there is over a 90% probability of encountering a date outside the 1% probability envelope.

Possible Causes for Inconsistent Durango Fluorapatite Dates

Our modeling results indicate that the observed U and Th inhomogeneity of Durango fluorapatite, while significant, is not likely to be the sole cause of the large dispersion of grain fragment ages obtained by House et al. (2000). In this section we explore a number of the most likely causes for the remaining dispersion

An Underestimation of the Magnitude of U and Th Variations

Our method of measuring spatial variations in U and Th concentrations in Durango fluorapatite – laser ablation ICPMS – had a resolution of roughly 100μm, which is significantly larger than scale of zoning observed in XRE maps. It is not only possible, but rather likely, that our laser pits homogenized small-scale variations. The effect of this is to dampen the absolute magnitiude of U and Th variations, which would, in turn, lead to an underestimation of the dispersion of dates in our synthetic populations.

An Inability to Resolve the True Scale of Compositional Heterogeneities

Although XRE mapping provides better resolving power (nominally 10μm), this still may be larger than the true scale of U and Th zoning in Durango fluorapatite. Zoning at a scale smaller than the alpha ejection length scale (~22 μm) would have a disproportionately profound impact on apparent age dispersions, making our estimates unreasonably low.

Possible Control of Fragment Orientation by Zone and Cleavage Boundaries

Because of the hexagonal symmetry of fluorapatite, it is not easy to determine optically if a prismatic or tabular fragment is oriented parallel to zone boundaries in the crystal. The

possibility that apatite shards are preferentially oriented during crushing would raise the fraction of fragments displaying maximum or near maximum errors. Because Th variations coincide with variations in other elements (e.g., Si, Cl, and REE), it is likely that there is a change in the unit cell parameters of the apatite at the zone boundaries. Adjacent unit cells with different compositions will be bounded by a high-strain region, which would be more likely to fracture due to a structural mismatch. It is therefore possible that fragments might form preferentially along zone boundaries, a hypothesis backed up by the observation of roughly concentric fractures matching the observed zoning in certain sections. This preferred orientation would increase the magnitude of the fragment age dispersion.

Systematic Underestimation of Analytical Uncertainties

If the variation in U and Th zoning in Durango fluorapatite is not responsible for the large variation encountered in measured fragment dates, the only other possible explanation is that there is a widespread underestimation of analytical uncertainties in (U-Th)/He laboratories that have documented such variations. We think that this is improbable, but the possibility cannot be ruled out altogether and it seems prudent for all laboratories to review their approach to analytical error estimation just to make certain that all uncertainties are being propagated appropriately. Ultimately, the best method of ensuring correct and consistent error estimation among different laboratories would be to develop a well-characterized interlaboratory standard. We now turn to a new question: What can our assessment of the variations present in the Durango fluorapatite tell us about apatites (and other mineral phases) we might encounter during a thermochronologic study?

Impact of Chemical Variations on the (U-Th)/He Thermochronology of "Unknowns"

There is no reason to believe that the U and Th zoning that we have observed in the Durango example is a unique phenomenon. Many natural apatites may display trace element zoning (Kempe and Gotze 2002). For at least one collection of apatites from the late Caledonian Shap granite of northern England (Dempster et al. 2003), intracrystalline variations in U and Th exceed those reported here for Durango fluorapatite. It has been suggested elsewhere that otherwise inexplicable ages for natural samples may be a result of zoning effects on diffusive loss and/or alpha ejection (Reiners 2002).

As suggested by Farley et al. (Farley et al. 1996), one approach to dealing with zoned crystals is to physically remove zoned domains through a process such as air-abrasion or laser milling. Unfortunately, this solution is only viable when suitably large homogeneous volumes can be identified and isolated. It has not been standard practice for apatite (U-Th)/He geochronologic studies to include chemical characterization of the analyzed materials. Given our modeling results, this omission could substantially compromise the reliability of apatite (U-Th)/He dates if the analyzed grains were strongly zoned.

Even if zoning is recognized in materials destined for (U-Th)/He dating, it may not be practical to employ physical methods to isolate chemically homogeneous domains if the scale of zoning is very small or if the zoning is oscillatory. Such problems are magnified further if different kinds of zoning occur in different apatites from the same specimen. Consider, for example, the BSE and cathodoluminesence images of three apatite crystals in Figure 6. All of these grains are from a single granodiorite sample from the Kaapvaal craton in South Africa. One crystal fragment (Figure 6a) shows a complex pattern of compositional heterogeneities. A grain with this type of irregular U + Th distribution would likely have a different pattern of

diffusive loss than a homogeneous solid, resulting in an incorrect bulk closure temperature estimate. In addition, as this grain was clearly broken during extraction from the host rock, there is no way to adequately determine what effect, if any, alpha-exchange may have had on the ^{4}He content of the remaining fragment. The apatite shown in Figure 6b, while euhedral, has an irregular metamorphic overgrowth over an igneous core, which again would be difficult to model – broken or not. Even the third, more elongate apatite (Figure 6c), with its characteristic igneous symmetrical oscillatory zoning could pose problems to a geochronologist if broken. The high compositional contrast at the terminations are not present in all such crystals, thus prohibiting an accurate ejection correction on a broken fragment. An additional problem that would be faced by someone attempting to date this grain is the large zircon inclusion. As the grain is fractured exactly where the zircon is located, it is likely that the apatite would contain considerable unsupported ^{4}He despite the fact that the larger section of the crystal would appear to be inclusion-free.

Such issues are even more significant for zircon, titanite, and the orthophosphates monazite and xenotime, minerals which hold great promise for (U-Th)/He dating but are quite frequently zoned in U and Th (Franz et al. 1996; Hawkins and Bowring 1997; Foster et al. 2002; Aleinikoff et al. 2002) Ultimately, the most effective way to avoid complications associated with U and Th zoning in accessory minerals may be high spatial-resolution (U-Th)/He dating using laser microprobe technology (Boyce and Hodges 2003; Hodges and Boyce 2003)

Conclusions

Fluorapatite from Cerro de Mercado, Durango, Mexico, displays complex compositional zoning at a variety of scales. Laser ablation ICPMS analysis of representative crystal sections cut

perpendicular to the **c** axis reveals variations of 50% in U and over 60% in Th in single large grains. As a consequence of intrcrystalline alpha-particle recoil, such variations should lead to ^{4}He inhomogeneities that are not completely spatially corrrelated with U and Th heterogeneities. If large grains of Durango fluorapatite are crushed to a small grain size and the fragments are analyzed individually, these fragments would be expected to yield several percent variation in apparent ages. Thus, intercrystalline zoning may, in part, explain the dispersion of Durango fluorapatite fragment ages reported by many laboratories (e.g., House et al., 2000). However, numerical experiments designed to evaluate the magnituide of this effect suggest that it alone is not sufficient to explain all of the observed dispersion *if* the degree of U and Th zoning found in our study is indeed representative of all Durango fluorapatite samples.

The observed U and Th zoning in Durango fluorapatite and the numerical experiments reviewed here demonstrate that intracrystalline zoning may severely complicate (U-Th)/He geochronologic studies. Most accessory minerals dated using this technique are compositionally zoned. While the dating of large zoned crystals or the statistical combination of many dates of fragments from such crystals would eliminate the problem, the trend in (U-Th)/He geochronology is toward the analysis of smaller and smaller, single-crystal fragments. For such studies, it is advisable to characterize the degree and scale of intracrystalline U and Th zoning before evaluating the geologic significance of the resulting dates.

Acknowledgements

The authors would like to thank Terry Plank, Linda Farr, and Joel Sparks (Boston University) for their advice and assistance in performing and reducing LA-ICPMS analyses.

Neel Chatterjee (MIT) and Mike Jercinovic (University of Massachusetts, Amherst) are thanked for their expertise and effort in making BSE and XRE maps. R. Blair Schoene is thanked for his photographic contributions as well as his general counsel. Many thanks to Peter Reiners (Yale) for providing samples of the Durango fluorapatite. James Ziegler, Adam Kent, Sam Bowring, John Hanchar, and graduate students at both MIT and UCLA are thanked for their valuable discussions. Reviews by Tony Hurford, Fred McDowell, and Ken Farley helped to refine the initial manuscript, while the revised version was further inproved by the input of Malcolm Pringle and Peter Reiners. Their time and effort is greatly appreciated. This research was funded in part by a grant from the National Science Foundation.

Figure Captions

Figure 1. Depiction of processes responsible for the redistribution of ^{4}He in natural zoned crystals. Diffusion operates in all crystals at all times, but probably can be ignored at the low temperatures experienced by Durango fluorapatite after crystallization. Recoil or alpha-ejection is approximately a temperature-independent process which can significantly effect the parent/daughter ratios near zone boundaries because of the greater flux out of parent-enriched zones than out of parent-poor zones.

Figure 2. XRE maps of Durango fluorapatite, 11μm/pixel. a) Th map. b) Si map. Small point and linear light-colored features on Si map are laser-ablation scars, other features (dark on Si map, light on Th) are Fe-oxide inclusions.

Figure 3. Flow chart cartoon depicting the steps taken in the model. High-resolution Si XRE map (a) and lower resolution LA-ICPMS Th data (b) are combined to form a model map of

Th variations in the crystal (c). This map of Th is then subsampled (d) because of computational limitations, and ejection corrected assuming an isotropic weighted average of ^{235}U, ^{238}U and ^{232}Th ejection distances (e). The matrices of parent and daughter are then subsampled 5,000 times in randomly located and oriented regions of varying size (f). Ages are then calculated for each virtual fragment, and populations of ages are used to draw conclusions about the effect of zoning on fragments of Durango fluorapatite (g).

Figure 4. Distribution of ages produced for the model results. a) 180x45μm. b) 180x11μm. c) 50x12μm

Figure 5. Cumulative probability modeling curves depicting the probability of drawing an "unacceptable" grain for 0.5% (thin solid line), 1% (heavy dashed line), and 2% (heavy solid line) thresholds. a) 180x45μm. b) 180x11μm. c) 50x12μm

Figure 6. BSE and CL images of three apatites from the same grandiorite, Kaapvaal craton, S. Africa, collected and imaged by R. Blair Schoene. Scale bars are 100μm, and correspond to both CL and BSE images. Variably complex zoning in the apatites from this sample demonstrates the difficulty in assuming homogeneity in U and Th for the purposes of ejection and diffusion modeling. Bright spot in (c) indicates a large zircon inclusion, a further complication.

References

Aleinikoff, J. N., R. P. Wintsch, et al. (2002). "U–Pb geochronology of zircon and polygenetic titanite from the Glastonbury Complex, Connecticut, USA: an integrated SEM, EMPA, TIMS, and SHRIMP study." Chemical Geology 188: 125-147.

Bea, F. and P. Montero (1999). "Behavior of accessory phases and redistribution of Zr, REE, Y, Th, and U during metamorphism and partial melting of metapelites in the lower crust: An example from the Kinzigite Formation of Ivrea-Verbano, NW Italy." Geochimica et Cosmochimica Acta 63(7-8): 1133-1153.

Boyce, J. W. and K. V. Hodges (2003). "The present status and not-too-distant future of laser ablation (U-Th)/He geochronology." EOS, Transactions of the American Geophysical Union 84(Fall Meeting Supplement): V32C-1028.

Dempster, T. J., M. Jolivet, et al. (2003). "Magmatic zoning in apatite: a monitor of porosity and permeability changes in granites." Contributions to Mineralogy and Petrology 145: 568-577.

Farley, K. A. (2000). "Helium diffusion from apatite; general behavior as illustrated by Durango fluorapatite." Journal of Geophysical Research, B, Solid Earth and Planets 105(2): 2903-2914.

Farley, K. A., R. A. Wolf, et al. (1995). (U-Th)/He dating; overview of the system and analytical techniques. Geological Society of America, 1995 annual meeting, New Orleans, LA, United States.

Farley, K. A., R. A. Wolf, et al. (1996). "The effects of long alpha-stopping distances on (U-Th)/He ages." Geochimica et Cosmochimica Acta 60(21): 4223-4229.

Foster, G., H. D. Gibson, et al. (2002). "Textural, chemical and isotopic insights into the nature and behaviour of metamorphic monazite." Chemical Geology 191: 183-207.

Franz, G., G. Andrehs, et al. (1996). "Crystal chemistry of monazite and xenotime from Saxothuringian-Moldanubian metapelites, NE Bavaria, Germany." European Journal of Mineralogy 8: 1097-1118.

Hawkins, D. P. and S. A. Bowring (1997). "U-Pb systematics of monazite and xenotime: case studies from the Paleoproterozoic of the Grand Canyon, Arizona." Contributions to Mineralogy and Petrology 127: 87-103.

Hodges, K. V. and J. W. Boyce (2003). "Laser-Ablation (U-Th)/He Geochronology." EOS, Transactions of the American Geophysical Union 84(Fall Meeting Supplement): V22G-05.

House, M. A., K. A. Farley, et al. (2000). "Helium chronometry of apatite and titanite using Nd-YAG laser heating." Earth and Planetary Science Letters 183: 365-368.

Kempe, U. and J. Gotze (2002). "Cathodoluminesence (CL) behaviour and crystal chemistry of apatite from rare-metal deposits." Mineralogical Magazine 66: 151-172.

Nekrasov, I. Y. (1973). "New data on a mineral of the monazite-cheralite-huttonite group." Transactions (Doklady) of the U.S.S.R. Academy of Sciences: Earth Science Sections 204: 134-136.

Press, W. H., S. A. Teukolsky, et al. (1992). Numerical Recipes in C: The Art of Scientific Computing. Cambridge, Cambridge University Press.

Reiners, P. W. (2002). "(U-Th)/He chronometry experiences a renaissance." EOS, Transactions of the American Geophysical Union 83(3): 21-27.

Wolf, R. A., K. A. Farley, et al. (1996). "Helium diffusion and low-temperature thermochronometry of apatite." Geochimica et Cosmochimica Acta 60(21): 4231-4240.

Young, E. J., A. T. Myers, et al. (1969). Mineralogy and geochemistry of fluorapatite from Cerro de Mercado, Durango, Mexico, United States Geological Survey: D84-D93.

Zeitler, P. K., A. L. Herczeg, et al. (1990). "U-Th-He dating of apatite: A potential Thermochronometer." Geochimica et Cosmochimica Acta 51: 2865-2868.

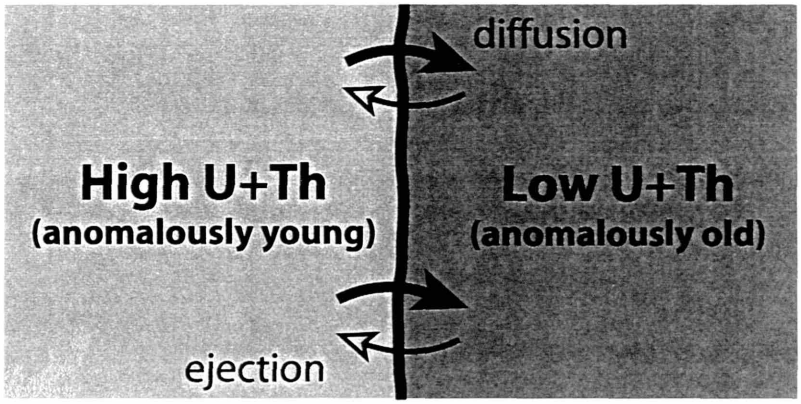
diffusion
High U+Th
(anomalously young)
Low U+Th
(anomalously old)
ejection

Figure 1

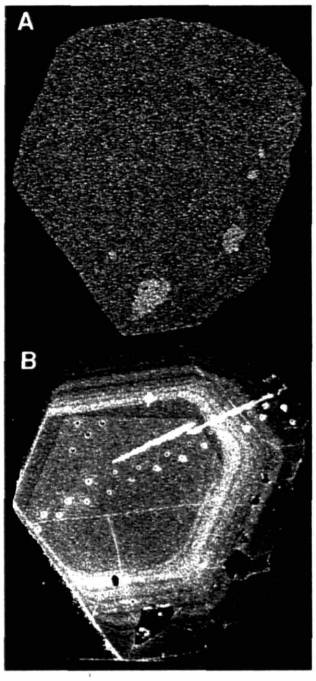

Figure 2

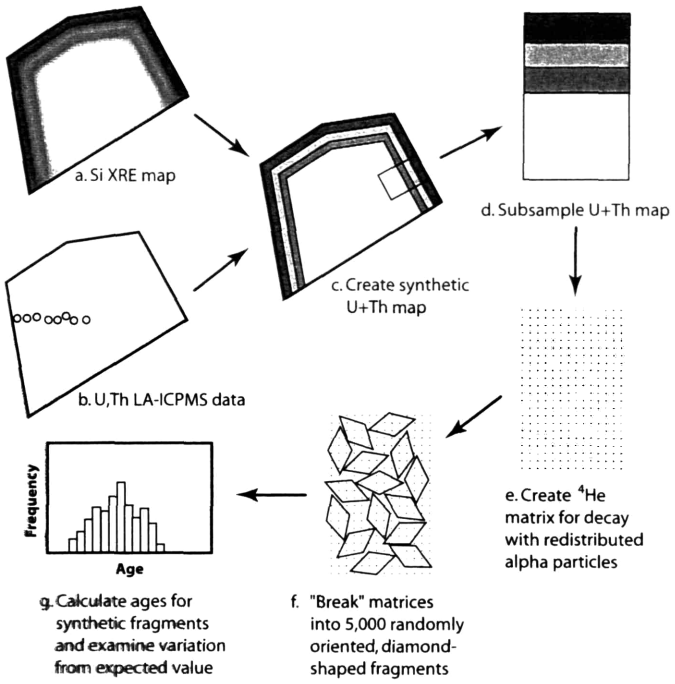

Sensitivity Analysis

h. Repeat steps f-g for fragments of different sizes
i. Repeat steps f-g for fragments with different aspect ratios
j. Repeat steps f-g for rectangular fragments
k. Repeat steps a-g assuming 2x, 4x the observed variation in U,Th
l. Repeat steps a-g with the scale of zoning reduced by 50%, 25%

Figure 3

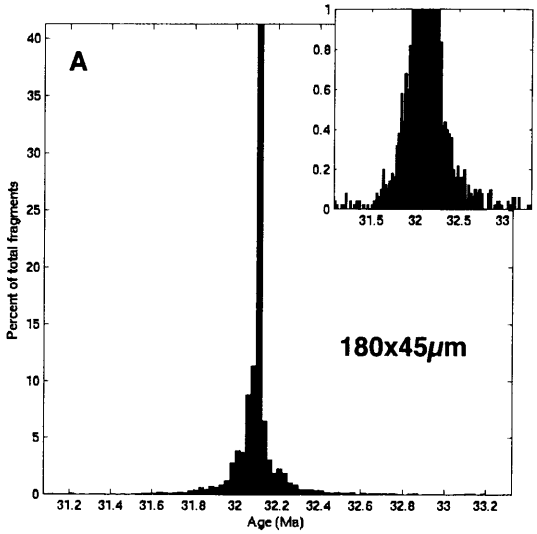
A
180x45μm
Percent of total fragments
Age (Ma)

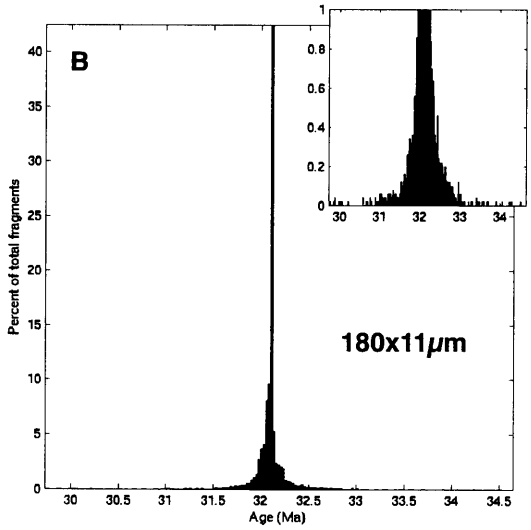
B
180x11μm
Percent of total fragments
Age (Ma)

Figure 4

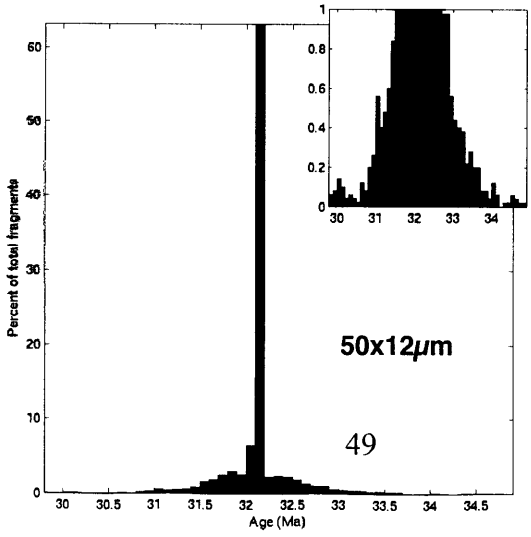
50x12μm
Percent of total fragments
Age (Ma)

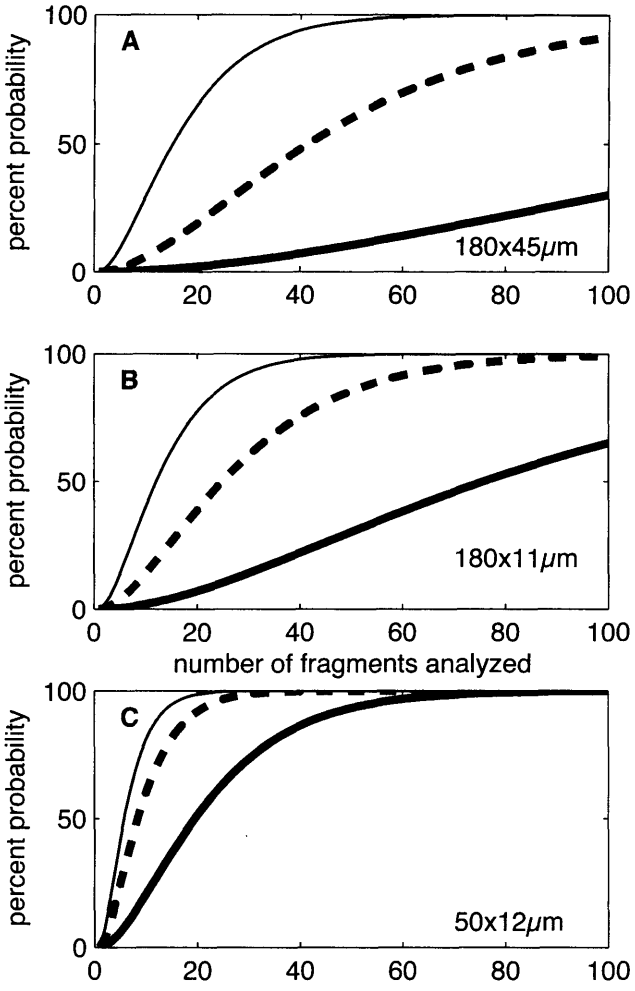
A
B
C
percent probability
100
50
0
0
20
40
60
80
100
180x45μm
180x11μm
50x12μm
number of fragments analyzed

Figure 5

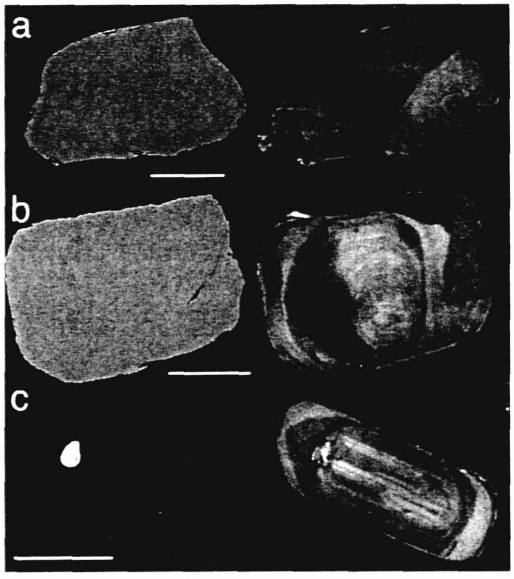

Figure 6

Table 1 Laser-ablation ICPMS data (ppm)

Spot	Sr	2σ	Sm	2σ	Dy	2σ	Th	2σ	U	2σ
B4	428	20	180	9	137	6	214	7	10.9	0.8
B5	438	20	182	9	151	6	311	10	15.0	0.7
B6	441	20	192	10	161	6	281	9	14.7	0.7
B7	453	20	217	11	190	7	329	11	14.7	0.7
B8	454	20	199	10	180	7	312	10	12.3	0.7
C4	449	20	191	9	180	7	301	10	11.7	0.6
C5	455	20	188	9	179	7	311	10	12.2	0.6
C6	443	20	186	9	176	7	304	10	12.0	0.6
C7	438	20	184	9	175	7	298	10	11.4	0.7
C8	455	21	190	9	180	7	300	10	11.6	0.8
D4	448	20	192	9	171	7	288	9	11.3	0.5
E1	447	20	190	9	167	6	286	9	11.2	0.5
E2	447	20	186	9	162	6	278	9	11.8	0.6
E3	444	20	190	9	167	6	283	9	11.7	0.5
E4	447	20	191	9	168	7	285	9	11.7	0.7
F4	436	21	186	10	175	7	290	10	11.8	0.7
F5	450	23	186	11	174	8	292	10	12.6	1.1
F6	451	23	189	11	177	8	292	10	12.7	1.1
F7	440	23	183	10	168	8	278	9	11.9	1.1
F8	437	24	173	10	153	7	246	8	10.2	1.3
G4	430	23	210	12	179	8	267	9	13.8	1.4
G5	421	23	184	11	152	7	253	8	12.6	1.2
G6	412	19	155	8	129	5	203	7	11.4	0.6
G8	430	21	165	9	126	5	219	7	12.0	0.8
J5	451	20	202	10	186	8	310	10	11.1	0.9
J6	454	21	203	10	188	8	305	10	11.0	1.0
J7	450	21	199	11	186	8	311	10	11.4	1.1
J8	440	25	194	12	178	9	297	10	11.1	1.7

TABLE 2 Results of numerical model described in the text.

Parallelograms	L	W	AR	AREA (μm2)	N	MEAN (Ma)	STD (Ma)	MAD (Ma)	MAX (Ma)	Percent dispersion greater than threshold (%) 0.5	1	2	3	4	5	6
	400	100	4	20000	5000	32.1	0.06	0.03	0.44	3.0	0.6	-	-	-	-	-
	300	75	4	11250	5000	32.1	0.08	0.04	0.70	4.1	1.6	0.5	0.1	-	-	-
	200	50	4	5000	5000	32.1	0.13	0.06	1.08	9.0	3.6	0.9	0.1	-	-	-
	100	25	4	1250	5000	32.1	0.25	0.12	2.29	23.4	12.1	3.0	1.3	0.8	0.4	0.1
	50	12	~4	300	5000	32.1	0.39	0.18	2.90	27.5	19.2	8.5	4.4	2.1	1.1	0.7
	180	180	1	16200	5000	32.1	0.06	0.03	0.35	2.1	-	-	-	-	-	-
	180	90	2	8100	5000	32.1	0.10	0.05	0.65	7.1	2	-	-	-	-	-
	180	45	4	4050	5000	32.1	0.14	0.07	1.25	10.8	4.0	1.1	-	-	-	-
	180	23	~8	2025	5000	32.1	0.17	0.08	1.68	11.9	5.3	1.5	0.3	0.2	-	-
	180	11	~16	1012.5	5000	32.1	0.22	0.09	2.57	13.5	6.6	2.2	1.0	0.6	0.3	0.3
Sensitivity Analysis																
2x Th contrast	180	45	4	4050	5000	32.1	0.33	0.15	3.88	25.6	12.1	5.2	2.5	1.5	0.8	0.5
4x Th contrast	180	45	4	4050	5000	34.4	28.00	4.48	1168	36.7	28.9	17.7	13.2	10.9	9.4	8.0
half zonewidth	180	45	4	4050	5000	32.1	0.17	0.09	1.65	15.6	5.5	1.5	0.5	0.1	-	-
quarter zonewidth	180	45	4	4050	5000	32.1	0.24	0.14	1.49	27.7	10.7	3.5	1.1	0.2	-	-
rectangles	180	45	4	8100	5000	32.1	0.10	0.05	0.87	8.8	2.4	0.2	-	-	-	-
17μm ejection radius	180	45	4	4050	5000	32.1	0.09	0.04	0.94	5.9	1.8	0.3	-	-	-	-

Table 2. Results of numerical modeling described in the text, with abbreviations as follows: L, fragment length; W, fragment width; AR, fragment aspect ratio; N, number of model runs performed.

CHAPTER 2

He diffusion in Monazite: Implications for (U-Th)/He thermochronometry

Boyce, J. W., Hodges, K.V., Olszewski, W.J., and Jercinovic, M.J.

As published in:

Geochemistry, Geophysics, Geosystems, v. 6, Q12004,

doi:10.1029/2005GC001058

Abstract

The light rare-earth phosphate mineral monazite contains high concentrations of Th and U and thus should have potential as a (U-Th)/He thermochronometer. New ^{4}He diffusion experiments confirm this potential, but suggest that the bulk closure temperature may be so strongly compositionally dependent that successful applications will require careful sample characterization prior to (U-Th)/He dating. Three experiments were performed on single crystals of Monazite 554, a material that has been used as a standard for Th-Pb ion microprobe geochronology. The data from each experiment yielded a linear array on an Arrhenius diagram, consistent with simple diffusion behavior. However, the diffusion parameters indicated for each grain were statistically different, indicating closure temperatures (assuming a cooling rate of 10°C/my) of 206 ± 24°C, 230 ± 4°C, and 286 ± 13°C. X-ray compositional maps of Monazite 554 illustrate a possible cause of this discrepancy: strong and geometrically complex chemical zoning that varies from grain to grain and likely corresponds to several episodes of growth and dissolution. If He diffusivity in monazite is compositionally controlled, individual crystals with such inconsistent zoning – which is typical of naturally occurring monazites – should have different bulk closure temperatures.

Introduction

Most (U-Th)/He thermochronometric studies focus on the minerals titanite, zircon, and apatite, all of which have bulk closure temperatures (Dodson 1973; Hodges 2003) that have been defined well through ^{4}He volume diffusion experiments and empirical studies. For titanite, the data indicate a bulk closure temperature of ~190-220°C for commonly encountered grain sizes and a cooling rate of 10°C/my (Reiners and Farley 1999; Stockli and Farley 2004). For the same cooling rate and nominal grain size ranges, the bulk closure temperatures for zircon and apatite

are ~170-190°C and ~70-80°C, respectively (Farley 2000; Reiners et al. 2002; Reiners et al. 2004; Reiners in press). Although these three mineral-isotopic systems are useful for a wide range of thermochronologic studies, there is considerable interest in expanding the temperature range of (U-Th)/He thermochronology to higher temperatures in order to allow more direct comparisons with $^{40}Ar/^{39}Ar$ thermochronometers. One mineral that offers considerable promise in this regard is monazite.

A light rare-earth element phosphate, monazite is frequently found as an accessory mineral in peraluminous granites and in pelitic rocks metamorphosed over a wide range of pressure and temperature conditions (Overstreet 1967; Rapp and Watson 1986; Spear and Pyle 2002). Owing to its high Th and U content (up to several weight percent), monazite is a commonly utilized and well-studied U-Th-Pb chronometer (Parrish 1990; Harrison et al. 2002). In theory, the rapid ingrowth of radiogenic ^{4}He in a typical monazite should make it possible to date very young igneous and metamorphic crystals using conventional (U-Th)/He methods, or to date very small intracrystalline domains using emerging microanalytical technqiues such as those made possible with the laser microprobe (Boyce et al. 2005).

The crystal structure of monazite is more densely packed than that of apatite, such that the diffusion rate of ^{4}He might be expected to be slower in monazite than in apatite. For example, (Dowty 1980) suggested that the mobility of elements in minerals is strongly dependent on a parameter he referred to as "anion porosity", which can be defined as the percentage of the unit cell volume not occupied by anions. This prediction is borne out by experimental data (cited above) showing that ^{4}He diffusion is much slower in titanite and zircon – with nominal ionic porosities of 33.8% and 28.8% respectively – than in apatite (37.8%). The expected ^{4}He diffusivity for end-member $CePO_4$ monazite (with an ionic porosity of 31.7%) would be

expected to be similar to, but somewhat lower than, titanite. However, as noted by Dahl (1997), the wide range of possible light rare earth element and Th substitutions in the monazite structure results in a compositonally dependent range of ionic porosities (at least 28.6% to 32.3%) that implies a compositionally dependent range of ^{4}He diffusion rates. Dahl (1997) described a simple method by which the bulk closure temperature of an unstudied mineral-isotopic system could be predicted from pre-existing experimental datasets for other systems using ionic porosity. Following this approach – and using the Reiners and Farley (1999) and Farley (2000) ^{4}He diffusion parameters for titanite and apatite, ionic porosity values from Dahl (1997), and a cooling rate of 10°C/my – we estimate a ~226-333°C range of (U-Th)/He bulk closure temperatures for various compositions of monazite. The fact that this temperature is higher than the nominal ~170-190°C range for zircon based on the work of Reiners et al. (2004) is problematic: zircon has a lower ionic porosity than monazite and therefore should have a higher (U-Th)/He closure temperature. One possible explanation for this inconsistency is that ionic porosity is only a crude predictor of ^{4}He diffusivity. Alternatively, natural zircons may have a lower than predicted (U-Th)/He closure temperature due to radiation damage (Reiners in press). Clearly, direct studies of ^{4}He diffusivity in natural monazites over a range of compositions will be required to calibrate this potentially important thermochronometer.

In this paper, we report the results of such a study for Monazite 554, a material that is commonly used as a standard for ion microprobe Th-Pb dating (Harrison et al. 1999; Catlos et al. 2002). Interestingly, replicate experiments on three separate grains of Monazite 554 yielded statistically significant differences in diffusion parameters. Moreover, all three parameter sets were different from those obtained by Stockli and Farley (2005) in a separate study. In the pages

that follow, we discuss the likely cause of these discrepancies and its ramifications for (U-Th)/He thermochronology of monazite.

Characteristics of Monazite 554

Our study focused on an aliquot of Monazite 554 obtained from the UCLA National Ion Microprobe Facility courtesy of Dr. Axel Schmitt. This mineral was separated from a peraluminous granodiorite cropping out in the Santa Catalina Mountains of Arizona (Force 1997). Crystals from another split of Monazite 554 have yielded a $^{232}Th/^{208}Pb$ age – determined by isotope dilution, thermal ionization mass spectrometry (Harrison et al. 1999) – of 45.3 ± 1.4 Ma (2σ). Our aliquot includes gem-quality, 100-500 μm, euhedral to anhedral grains (Figure 1).

Although individual crystals of Monazite 554 have sufficiently uniform Th/Pb ratios to make them suitable as ion microprobe age standards (Harrison et al. 1999), they are distinctively zoned in backscattered electron images (Catlos et al. 2002). In order to determine the nature of such zoning, we produced x-ray compositional maps of representative grains of Monazite 554 using the Cameca SX-Ultrachron electron microprobe at the University of Massachusetts at Amherst (Figure 2). Maps of yttrium (using the characteristic Lα x-ray line), calcium (Kα), thorium (Mα), and uranium (Mβ) were obtained using a focused beam in rastering mode; for these measurements, the accelerating voltage was 15 kV and the Faraday cup current was 200nA. In large part, the zoning observed in backscattered electron images can be attributed to intracrystalline concentration variations of the rare-earth elements and thorium. Two kinds of zoning were observed (Figure 2): 1) concentric growth zoning, especially well expressed in the yttrium map of Grain 1; and 2) patchy or irregular zoning that locally truncates concentric growth zoning, as is apparent in the yttrium map of Grain 2. Following Hawkins and Bowring

(1997; 1999), we interpret the two zoning types and the truncation of one by the other as evidence of at least two episodes of precipitation and at least one intervening episode of dissolution during the paragenetic evolution of Monazite 554.

The thorium $M\alpha$ maps clearly demonstrate substantial intragranular variations in the concentration of this element in Monazite 554, but uranium $M\beta$ maps show less internal variation. (Note that the grayscales are not the same for each of the two crystals in Figure 2, so that the lighter shading of the U $M\beta$ map for Crystal 1 is not significant.) Catlos et al. (2002) published quantitative electron microprobe spot analyses of zoned Monazite 554 that demonstrated ThO_2 contents ranging from 2.90 to 4.31 wt. %, and UO_2 contents ranging from an undetectable amount to 0.12 wt. %. For our grains 1 and 2, reconnaissance analyses indicated comparable variations of ThO_2 (2.7-3.7 wt. %) and U contents that are uniformly <100 ppm.

The Th $M\alpha$ map of Grain 2 also reveals a small, Th-rich inclusion which is possibly thorite or a Th-rich representative of the monazite-huttonite solid-solution series (Förster 1998; Finch and Hanchar 2003). Similar inclusions are relatively common in individual grains of Monazite 554. Obviously, such inclusions would compromise diffusion studies, so we elected to perform our experiments on three hand-picked, subequant, inclusion-free crystal fragments that we refer to as Grain 3 (~140 μm), Grain 4 (~156 μm), and Grain 5 (~166 μm).

Experimental Methods

We measured the diffusivity of ^{4}He in the three grains using an incremental-heating approach similar to that previously employed for other He diffusion studies of silicates and phosphates (Lippolt et al. 1994; Wolf et al. 1996; Warnock et al. 1997; Reiners and Farley 1999; Farley 2000; Reiners et al. 2002). Each grain was cleaned in an ultrasonic bath, first with distilled water and then with ethanol, before being sealed in a double-vacuum resistance furnace

(Staudacher et al. 1978) for heating. Temperatures were monitored during the experiments by an R-type thermocouple outside of and in direct contact with the crucible. In order to account for potential thermal gradients between the inside and outside of the crucible, this thermocouple was calibrated against a second thermocouple (C-type) on the interior of the crucible prior to the experiments. The effects of temperature equilibration lag and overshoot due to the design of the double-vacuum furnace were minimized by utilizing short ramp times, long step durations, and sequential isothermal steps. Table 1 contains the temperatures employed and the duration of heating at that temperature for the three experiments. Gases released from the samples during each heating increment were purified by active metal gettering, and were spiked with a known amount of ^{3}He for measurement of ^{4}He concentrations by isotope dilution on a Balzers Prisma QMS200 quadrupole mass spectrometer. All measurements were corrected for blanks (as a function of temperature and step duration) and mass fractionation. Signal-to-blank ratios varied from ~10 to ~3500, with values of 30 to 100 for most measurements.

After sufficient incremental heating to fully degas each grain, the cumulative concentration of ^{4}He was used to establish the fractional loss of ^{4}He during each step. Assuming a spherical geometry, fractional losses can be related to diffusivity using Equation 1:

$$f \approx 1-\left(\frac{6}{\pi^2}\right)\sum_1^{\infty}\left[\left(\frac{1}{n^2}\right)\exp\left(-n^2\pi^2\frac{Dt}{a^2}\right)\right] \qquad \text{(all } f\text{)} \qquad (1)$$

Which can be approximated by:

$$f \approx 1-\left(\frac{6}{\pi^2}\right)\exp\left[-\pi^2\left(\frac{Dt}{a^2}\right)\right] \qquad (0.85 < f < 1) \qquad (2a)$$

$$f \approx 6\pi^{1/2}\left(\frac{Dt}{a^2}\right)^{1/2} - 3\left(\frac{Dt}{a^2}\right) \qquad (f < 0.85) \qquad (2b)$$

(Fechtig and Kalbitzer 1966; McDougall and Harrison 1999). Fractional losses for each step were used to calculate the Fourier number, a dimensionless parameter given by:

$$Fo = \frac{Dt}{a^2} \tag{3}$$

where D is diffusivity, t is the duration of the heating step, and a is the effective radius of diffusion. The ratio $\frac{D}{a^2}$ for ith increment in an experiment was determined by the following relationship:

$$\left(\frac{D}{a^2}\right)_i = \frac{\left[Fo_i - Fo_{(i-1)}\right]}{t_i} \tag{4}$$

and the natural logarithm of D/a^2 was plotted against inverse temperature to produce the familiar Arrhenius diagram. We anticipate a linear relationship for the data from an experiment of this kind:

$$\ln\left(\frac{D}{a^2}\right) = \left(\frac{-E}{R}\right)\left(\frac{1}{T}\right) + \ln\left(\frac{D_0}{a^2}\right) \tag{5}$$

where D_o represents diffusivity at infinite temperature, E is the activation energy, and R is the universal gas constant. Values of the diffusion parameters D_o and E were determined through error-weighted, least-squares linear regression of the experimental data. Uncertainties in $\ln(D/a^2)$ for each increment were based on propagated uncertainties in measured ^{4}He concentrations and blank values. Uncertainties in T for each step were conservatively estimated to be ±5°C. The resulting uncertainties are shown at the 2σ (~95% confidence) level in the Arrhenius diagram shown in Figure 4; for many experimental steps, the error bars are smaller than the symbol size. On this diagram, we show the best-fit line for each experimental dataset and the 2σ uncertainty hyperbolae for the fits. The quality of these fits was evaluated using the MSWD (mean squared weighted deviation) parameter, with assumed significance bounds as suggested by Wendt and

Carl (Wendt and Carl 1991). Uncertainties in D_0 and E reported here, also at 2σ, are based on measurement uncertainties as well as the fitting uncertainties for the linear regressions.

Experimental Results

For Grain 3, we performed a 17-step diffusion experiment over the temperature range 397 to 497°C (Figure 3a). The results define a statistically significant (MSWD = 0.72) linear array with a slope and $\ln(D/a^2)$-intercept indicative of an activation energy of 248 ± 11 kJ/mol and $\ln(D_o/a^2)$ of 27.4 ± 1.8 s^{-1}. For Grain 4 (Figure 3b), the results of a 104-step diffusion experiment (515-764°C) yield a statistically significant (MSWD = 1.22) linear array indicating E = 179.6 ± 1.2 kJ/mol and $\ln(D_o/a^2)$ = 7.66 ± 0.16 s^{-1}. The 23 steps of our Grain 5 experiment (498-724°C; Figure 3c) showed a good linear correlation, but there is some excess scatter in the fit (MSWD = 6.37). The steps with large uncertainties were measured at intermediate temperatures after the sample had been heated to higher temperatures, and the magnitude of the errors reflect low ^4He yields relative to the system blank. However, the results for these steps lie on top of the results for measurements at the same temperatures earlier in the experiment, masking them in Figure 3c. Thus, the reproducibility of different isothermal steps is significantly better than the large uncertainties of the second measurements would suggest. For Grain 5, the modeled diffusion parameters are: E = 216.5 ± 4.9 kJ/mol and $\ln(D_o/a^2)$ of 11.32 ± 0.56 s^{-1}.

The data for the three experiments (shown at the same scale in Figure 4) may be used to calculate bulk closure temperatures for each of the three grains (Dodson 1973) assuming a nominal cooling rate of 10°C/my: 206 ± 24°C (Grain 3), 230 ± 4°C (Grain 4), 286 ± 13°C (Grain 5). This range of closure temperatures overlaps with that predicted by ionic porosity theory, and is higher than the range of closure temperatures calculated for all other potential (U-Th)/He

thermochronometers except titanite and garnet (Dunai and Roselieb 1996; Reiners and Farley 1999). Unfortunately, the uncertainty hyperbolae in Figure 4 demonstrate that the results of these experiments do not agree with one another in a statistical sense, and the spreads of values for E, $\ln(D_o/a^2)$, and bulk closure temperature are much greater than that which could be explained by experimental imprecision alone. In the following paragraphs, we review the possible explanations for this result.

Grain Size Dependence of ^{4}He Diffusivity

Empirical and experimental studies of titanite, apatite, and zircon have suggested that the physical grain size corresponds to the effective ^{4}He diffusion dimension for these minerals (Reiners and Farley 1999; Farley 2000; Reiners and Farley 2001). Since the three grains we studied were of three slightly different sizes, we have replotted $\ln(D_o/a^2)$ in Figure 5 using the physical half-grain size (70, 78, and 83 μm for grains 3, 4, and 5, respectively) to normalize the abscissa to $\ln(D_o)$. Although there may be a grain-size dependence of ^{4}He diffusivity in Monazite 554, Figure 5 shows that such a dependency does not eliminate the discrepancy among the experimental runs.

Inappropriate Choice of Diffusion Geometry

As noted by McDougall and Harrison (1999), grain geometry does not play a prominent role in fractional loss of a diffusive species, with losses as calculated using the equations of Fechtig and Kalbitzer (1966) converging rapidly with increasing fractional loss for various geometries. The resulting differences in calculated Fo produce a negligible effect on the calculated diffusion coefficients.

The monazite crystals used for our experiments are nearly spherical solids, with only slightly larger surface area/volume ratios than spheres (Figure 1). These deviations from

sphericity would result in a slight increase in ^{4}He release during the early portion of the experiments, but would have little overall effect on the calculated diffusion parameters and the grain-to-grain discrepancy among them. Moreover, a variety of workers have demonstrated that grains with shapes that do not correspond to simple geometric solids still yield robust and reproducible He diffusion data for minerals other than monazite (Reiners and Farley 1999; Farley 2000; Reiners et al. 2002).

Failure to Account for α-ejection Redistribution of Radiogenic ^{4}He

When an α particle (^{4}He) is produced by radioactive decay, the energy liberated as a result propels the α particle a distance that is intrinsic to the chemistry and structure of the mineral in which it is produced (Farley et al. 1996). For monazite, that distance is 16-19 μm (Ziegler et al., 2003). Thus, natural, pristine crystals of monazite should have a depletion rim of ^{4}He simply due to the α-ejection process. By not correcting for this effect in our experiments, could we have induced the different diffusive behaviors evident in Figures 4 and 5? We would argue that the answer is no. Any amount of near-rim depletion would serve simply to reduce the apparent fractional loss of ^{4}He per unit time in the early stages of an experiment. Since most of the data used to define the linear fits on the Arrhenius diagrams pertain to relatively large fractional losses, such effects have little impact on the overall diffusive behavior of our grains of Monazite 554.

Contamination by Inclusions

Although we were careful to select samples free of inclusions that were visible under the microscope, we cannot preclude the possibility that microinclusions were missed. During our reconaissance study, we observed only high-Th inclusions that are interpreted to be Th-rich phases in the monazite-huttonite solid-solution series or thorite. Any grain-to-grain variability in

^{4}He diffusivity related to such inclusions would imply a significant dependence of diffusivity on composition, since such inclusions are not volumetrically significant and are not uniformly distributed among grains in the aliquot. Microinclusions would simply provide excess helium to the surrounding monazite, and thus another explanation is required.

Multiple Diffusion Domains

Another possibility is that the effective diffusion dimension of monazite is less than the physical grain size, and that the three studied grains had different distributions of diffusion domains of different sizes. Such behavior has been proposed to explain the variable diffusivity of ^{40}Ar in natural K-feldspars (e.g. Lovera and Richter 1991; e.g. Lovera et al. 1997). In this interpretation, the different grains should produce subparallel Arrhenius lines suggestive of a constant activation energy but different values of ln(Do/a^2). Statistically speaking, the observed variations in slope are inconsistent with this interpretation. If the grain-to-grain discrepancy can be attributed to the existence of variably sampled multiple diffusion domains, it seems likely that such domains have different inherent diffusivities and are not simply of different sizes.

Intergranular Compositional Variability

We think the most likely explanation for the observed inconsistencies among the three experimental runs is evident in Figure 2: a geometrically complex, intragranular variability in calcium, yttrium, thorium and – to a much lesser extent – in uranium that is different in different grains. Although experiments on natural and synthetic monazites show little dependence of Pb diffusivity on composition (Cherniak et al. 2004), we might expect the impact of structural changes related to chemical substitutions to have a greater impact on the diffusivity of a neutral species like He (Dowty 1980). In fact, recent independent studies by Stockli and Farley (2005) also suggest that there is a dependence of ^{4}He diffusion in monazite on composition, with

diffusivity increasing with increasing Th content. If this is the case, and if the compositional variability shown in Figure 2 is representative of Monazite 554, we would expect every crystal to display different He diffusion characteristics.

Compounding this effect is that internal Th+U zoning in Monazite 554 will naturally produce a non-uniform concentration of ^{4}He. Along with the internal redistribution of ^{4}He as a consequence of α-recoil (Boyce and Hodges 2005), this variation substantially complicates the interpretation of each diffusion experiment. It is tempting to assume that, if a diffusion study is conducted on a crystal with a non-uniform initial concentration of the diffusant being studied, the resulting data will show a predictable non-linearity on an Arrhenius diagram. Unfortunately, this is only the case if the zoning is geometrically simple and concentric, such as in the case of near-rim α-ejection depletion. The zoning in Monazite 554 is clearly not of this form, and it is probable that the linear arrays on Figure 4 are the result of the homogenization of ^{4}He liberated from a variety of domains with a variety of intrinsic ^{4}He diffusivities throughout much of the experiment (Lovera et al. 2002). Subtle suggestions in the dataset of deviations from non-linearity at the highest and lowest temperatures are likely to be due to a lack of ^{4}He liberation from more retentive domains at low temperatures and the progressive depletion of less retentive domains at higher temperatures.

Implications of the Results for (U-Th)/He Thermochronometry

Given the previously documented chemical variability of Monazite 554 (Catlos et al. 2002), it reasonable to question why we expended the time and energy to conduct these experiments on such an "inappropriate" material. Obviously, compositionally uniform monazites would yield more easily interpretable results, but the simple fact is that naturally occuring

monazites are rarely compositionally homogeneous. The complexity and magnitude of the compositional zoning shown in Figure 2 is not at all unusual in metamorphic and igneous monazites (e.g., DeWolf et al. 1993; Hawkins and Bowring 1997; Hawkins and Bowring 1999; Zhu and O'Nions 1999; Viskupic and Hodges 2001; Viskupic et al. 2005). In fact, in the course of our search for compositionally uniform monazites for ^{4}He diffusion studies, we have found only one example. While a set of experiments on that material is underway, it must be noted that the results will be of limited significance to (U-Th)/He thermochronology unless homogeneous monazites of a variety of compositions can be studied. One fruitful approach may be to utilize synthetic monazites, which could be impregnated with helium either by diffusion or by proton-irradiation (Shuster et al. 2004).

For now, we can say only that there is no single bulk closure temperature for the (U-Th)/He monazite thermochronometer; our results indicate that individual crystals from the same aliquot of Monazite 554 have closure temperatures that range from ~200-290°C, and it is quite likely that additional experiments on different crystal fragments from the same aliquot would extend that range. This has two important implications for thermochronometric applications. First, until on-going studies in our laboratory and elsewhere can better define the compositional and grain-size dependence of ^{4}He diffusion in monazite, the most effective applications of the thermochronometer will necessitate incremental heating experiments on individual crystals – followed by U, Th, and Sm analysis – in order to determine simultaneously a closure temperature and a cooling age for an individual crystal. Second, the grain-to-grain variability in closure temperature documented here can be turned to our advantage because it implies that (U-Th)/He studies of a variety of monazite crystals from a single sample can be used to recover a significant portion of the cooling history of the sample. Ultimately, when we better understand He

diffusivity as a function of composition, it should be possible to obtain similar histories from single, complexly zoned monazite crystals by employing microanalytical techniques such as those described by Boyce et al. (2005).

One additional concern that must be addressed before monazite becomes a widely applied thermochronometer is the impact of radiation damage on ^{4}He diffusivity. As is the case with zircon [*Reiners*, in press; *Reiners, et al.*, 2002], high concentrations of radioactive elements - especially Th in the case of monazite - could damage the crystal structure, resulting in the development of fast diffusion pathways over geologic time, A monazite effected in this way might lose substantial ^{4}He well below its nominal closure temperature and yield a "thermochronometrically meaningless" age. Fortunately, numerous studies of the annealing of radiation damage in monazite have been done in order to evaluate the suitability of the monazite structure for isolating radioactive wastes (e.g. Meldrum et al. 1998; e.g. Meldrum et al. 2000). The results indicate that monazite anneals readily at temperatures greater than about 175°C, such that radiation damage in this mineral is substantially less common than in zircon. As a consequence, we might anticipate that radiation damage will not compromise the utility of the (U-Th)/He monazite thermochronometer, but more experiments are necessary to confirm this prediction.

Conclusions

The ion microprobe standard Monazite 554 displays complex chemical zoning suggestive of multiple episodes of precipitation and dissolution. For example, intracrystalline variations in Th vary by a factor of two. In addition, some crystals contain inclusions of a high-Th mineral interpreted as huttonite or huttonitic monazite.

Incremental-heating experiments on three, apparently inclusion-free crystal fragments of Monazite 554 each yield linear arrays suggestive of simple, thermally activated diffusive loss of ^{4}He. However, the diffusion parameters determined from these arrays are significntly different, implying closure temperatures of 206°C, 230°C, and 286°C assuming a 10°C/m.y. cooling rate. These discrepancies are most simply explained by a strong dependence of ^{4}He diffusivity on monazite composition, such that each complexly zoned crystal has a different bulk diffusion behavior and thus (U-Th)/He closure temperature.

Figure Captions

Figure 1: Photomicrographs of monazites used in diffusion experiments. A) Grain 3 (note that this grain split along the prominent fracture into two equal-sized fragments during loading). B) Grain 4. C) Grain 5.

Figure 2: X-ray maps of Y, Ca, Th, and U in 554 monazite grains 1 and 2. Note prominent inclusion in Th map of Grain 2, likely huttonite.

Figure 3: Arrhenius diagrams of each diffusion experiment with 2σ uncertainties, and 2σ uncertainty-hyperbole (shaded regions).

Figure 4: Arrhenius diagram showing data for all three experiments at the same scale with 2σ uncertainties, error-weighted best fit lines, and 2σ uncertainty-hyperbole (shaded regions).

Figure 5: Arrhenius diagram normalized to grain radius (assuming grain size is effective diffusion dimension), again showing uncertainties at 2σ.

References Cited

Boyce, J. W. and K. V. Hodges (2005). "U and Th zoning in Cerro de Mercado (Durango, Mexico) fluorapatite: Insights regarding the impact of recoil redistribution of radiogenic ^{4}He on (U–Th)/He thermochronology." Chemical Geology **219**: 261-274.

Boyce, J. W., K. V. Hodges, et al. (2005). "Laser microprobe (U-Th)/He thermochronometry of monazite." Geochimica et Cosmochimica Acta **69**: A298.

Catlos, E. J., L. D. Gilley, et al. (2002). "Interpretation of monazite ages obtained via in situ analysis." Chemical Geology **188**: 193-215.

Cherniak, D. J., E. B. Watson, et al. (2004). "Pb diffusion in monazite: A combined RBS/SIMS study." Geochimica et Cosmochimica Acta **68**: 829-840.

Dahl, P. S. (1997). "A crystal-chemical basis for Pb retention and fission-track annealing systematics in U-bearing minerals, with implications for geochronology." Earth and Planetary Science Letters **150**(3-4): 277-290.

DeWolf, C. P., N. Belshaw, et al. (1993). "A metamorphic history from micron-scale ^{207}Pb/^{206}Pb chronometry of Archean monazite." Earth and Planetary Science Letters **120**: 207-220.

Dodson, M. H. (1973). "Closure temperature in cooling geochronological and petrological systems." Contributions to Mineralogy and Petrology **40**: 259-274.

Dowty, E. (1980). "Crystal-chemical factors affecting the mobility of ions in minerals." American Mineralogist **65**: 174-182.

Dunai, T. J. and K. Roselieb (1996). "Sorption and diffusion of helium in garnet: implications for volatile tracing and dating." Earth and Planetary Science Letters **139**: 411-421.

Farley, K. A. (2000). "Helium diffusion from apatite: General behavior as illustrated by Durango fluorapatite." Journal of Geophysical Research **105**: 2903-2914.

Farley, K. A. (2000). "Helium diffusion from apatite; general behavior as illustrated by Durango fluorapatite." Journal of Geophysical Research, B, Solid Earth and Planets **105**(2): 2903-2914.

Farley, K. A., R. A. Wolf, et al. (1996). "The effects of long alpha-stopping distances on (U-Th)/He ages." Geochimica et Cosmochimica Acta **60**(21): 4223-4229.

Fechtig, H. and S. Kalbitzer (1966). The diffusion of argon in potassium-bearing solids. Potassium Argon Dating. O. A. Schaeffer and J. Zahringer. New York, Springer-Verlag**:** 68-107.

Finch, R. J. and J. M. Hanchar (2003). "Structure and chemistry of zircon and zircon-group minerals." Reviews in Mineralogy and Geochemistry **53**: 1-25.

Force, E. R. (1997). Geology and Mineral Resources of the Santa Catalina Mountains, Southeastern Arizona. Tucson, AZ, Center for Mineral Resources, Monographs in Mineral Science 1.

Förster, H.-J. (1998). "The chemical composition of REE-Y-Th-U-rich accessory minerals in peraluminous granites of the Erzgebirge-Fichtelgebirge region, Germany, Part I: The monazite-(Ce)-brabantite solid solution series." American Mineralogist **83**: 259-272.

Harrison, T. M., E. J. Catlos, et al. (2002). "U-Th-Pb dating of phosphate minerals." Reviews in Mineralogy and Geochemistry **48**: 523-558.

Harrison, T. M., M. Grove, et al. (1999). "Origin and episodic emplacement of the Manaslu intrusive complex, central Himalaya." Journal of Petrology **40**: 3-19.

Hawkins, D. P. and S. A. Bowring (1997). "U-Pb systematics of monazite and xenotime: case studies from the Paleoproterozoic of the Grand Canyon, Arizona." Contributions to Mineralogy and Petrology **127**: 87-103.

Hawkins, D. P. and S. A. Bowring (1999). "U-Pb monazite, xenotime and titanite geochronological constraints on the prograde to post-peak metamorphic thermal history of Paleoproterozoic migmatites from the Grand Canyon, Arizona." Contributions to Mineralogy and Petrology **134**: 150-169.

Hodges, K. V. (2003). Geochronology and Thermochronology in Orogenic Systems. The Crust. R. L. Rudnick. Amsterdam, Elsevier Science. **3:** 263-292.

Lippolt, H. J., M. Leitz, et al. (1994). "(Uranium+thorium)/helium dating of apatite; experience with samples from different geochemical environments." Chemical Geology **112**(1-2): 179-191.

Lovera, O. M., M. Grove, et al. (2002). "Systematic analysis of K-feldspar $^{40}Ar/^{39}Ar$ step-heating results II: Relevance of laboratory argon diffusion properties to nature." Geochimica Cosmochimica Acta **66**: 1237-1255.

Lovera, O. M., M. Grove, et al. (1997). "Systematic analysis of K-feldspar 40Ar/39Ar step heating results: I. Significance of activation energy determinations." Geochimica et Cosmochimica Acta **61**(15): 3171-3192.

Lovera, O. M. and F. M. Richter (1991). "Diffusion domains determined by ^{39}Ar released during step heating." Journal of Geophysical Research, B, Solid Earth and Planets **96**: 2057-2069.

McDougall, I. and T. M. Harrison (1999). Geochronology and thermochronology by the $^{40}Ar/^{39}Ar$ method. New York, Oxford University Press.

Meldrum, A., L. A. Boatner, et al. (2000). "A comparison of radiation effects in crystalline ABO (sub 4) -type phosphates and silicates." Mineralogical Magazine **64**(2(423)): 185-194.

Meldrum, A., L. A. Boatner, et al. (1998). "Radiation damage in zircon and monazite." Geochimica et Cosmochimica Acta **62**(14): 2509-2520.

Overstreet, W. C. (1967). The geologic occurrence of monazite, United States Geological Survey: 327.

Parrish, R. (1990). "U-Pb dating of monazite and its application to geological problems." Canadian Journal of Earth Sciences **27**: 1431-1450.

Rapp, R. P. and E. B. Watson (1986). "Monazite dissolution kinetics: implications for thorium and light rare earth chemistry of felsic magmas." Contributions to Mineralogy and Petrology **94**: 304-316.

Reiners, P. W. (in press). Zircon (U-Th)/He thermochronometry. Thermochronology: Reviews in Mineralogy and Geochemistry. P. W. Reiners and T. A. Ehlers. Washington, D.C., Mineralogical Society of America. **59**.

Reiners, P. W. and K. A. Farley (1999). "Helium diffusion and (U-Th)/He thermochronometry of titanite." Geochimica et Cosmochimica Acta **63**(22): 3845-3859.

Reiners, P. W. and K. A. Farley (2001). "Influence of crystal size on apatite (U-Th)/He thermochronology: an example from the Bighorn Mountains, Wyoming." Earth and Planetary Science Letters **188**(3-4): 413-420.

Reiners, P. W., K. A. Farley, et al. (2002). "He diffusion and (U-Th)/He thermochronometry of zircon: Initial results from Fish Canyon Tuff and Gold Butte." Tectonophysics **349**: 247-308.

Reiners, P. W., T. L. Spell, et al. (2004). "Zircon (U-Th)/He thermochronometry: He diffusion and comparisons with $^{40}Ar/^{39}Ar$ dating." Geochimica et Cosmochimica Acta **68**: 1857-1887.

Shuster, D. L., K. A. Farley, et al. (2004). "Quantifying the diffusion kinetics and spatial distributions of radiogenic ^{4}He in minerals containing proton-induced ^{3}He." Earth and Planetary Science Letters **217**: 19-32.

Spear, F. S. and J. M. Pyle (2002). Apatite, monazite, and xenotime in metamorphic rocks. Phosphates: Geochemical, Geobiological, and Materials Importance. M. J. Kohn, J. Rakovan and J. M. Hughes. Washington, D.C., USA, Mineralogical Society of America. **43:** 293-336.

Staudacher, T., E. K. Jessberger, et al. (1978). "A refined ultra-high vacuum furnace for rare gas analysis." Journal of Physics E: Science Instrumentation **11**: 781-784.

Stockli, D., K. A. Farley, et al. (2005). "He diffusion and (U-Th)/He thermochronometry of monazite and rutile." Geochimica et Cosmochimica Acta **69**: A8.

Stockli, D. F. and K. A. Farley (2004). "Emperical constraints on the titanite (U-Th)/He partial retention zone from the KTB drill hole." Chemical Geology **207**: 223-236.

Viskupic, K. and K. V. Hodges (2001). "Monazite-xenotime thermochronometry: methodology and an example from the Nepalese Himalaya." Contributions to Mineralogy and Petrology **141**: 233-247.

Viskupic, K. M., K. V. Hodges, et al. (2005). "Timescales of melt generation and the thermal evolution of the Himalayan metamorphic core, Everest region, eastern Nepal." Contributions to Mineralogy and Petrology **149**: 1-21.

Warnock, A. C., P. K. Zeitler, et al. (1997). "An evaluation of low-temperature apatite U-Th/He thermochronometry." Geochimica et Cosmochimica Acta **61**: 5371-5377.

Wendt, I. and C. Carl (1991). "The statistical distribution of the mean squared weighted deviation." Chemical Geology **86**: 275-285.

Wolf, R. A., K. A. Farley, et al. (1996). "Helium diffusion and low temperature thermochronometry of apatite." Geochimica et Cosmochimica Acta **60**: 4231-4240.

Zhu, X. K. and R. K. O'Nions (1999). "Zonation of monazite in metamorphic rocks and its implications for high temperature thermochronology: a case study from the Lewisian terrain." Earth and Planetary Science Letters **171**: 209-220.

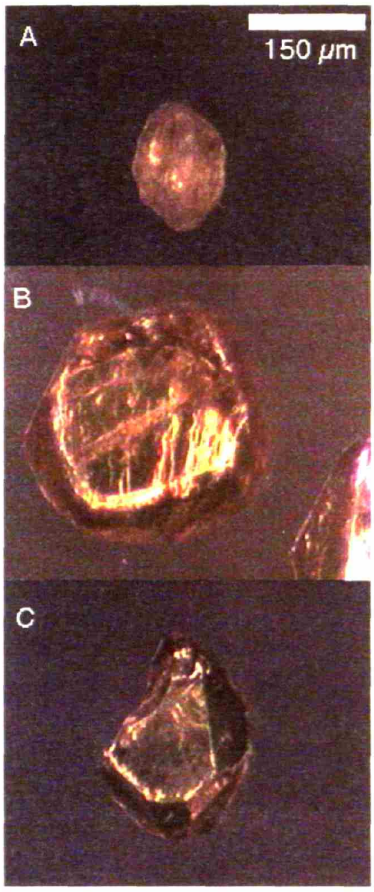

Figure 1

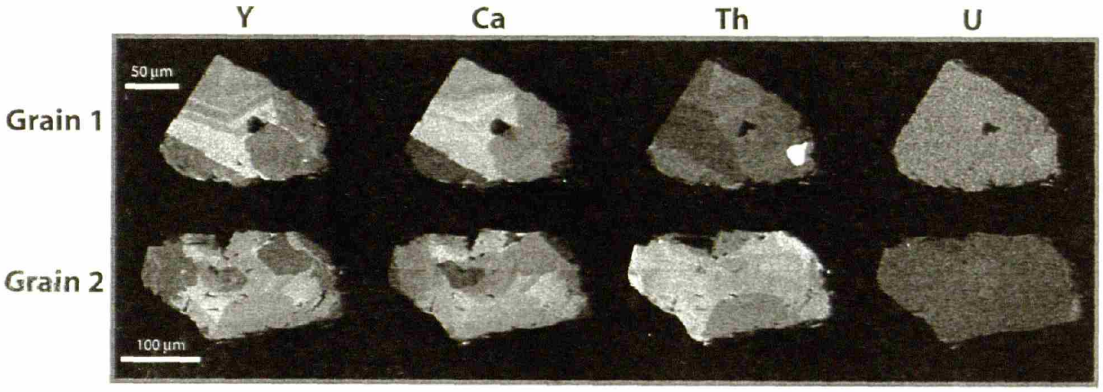

Figure 2

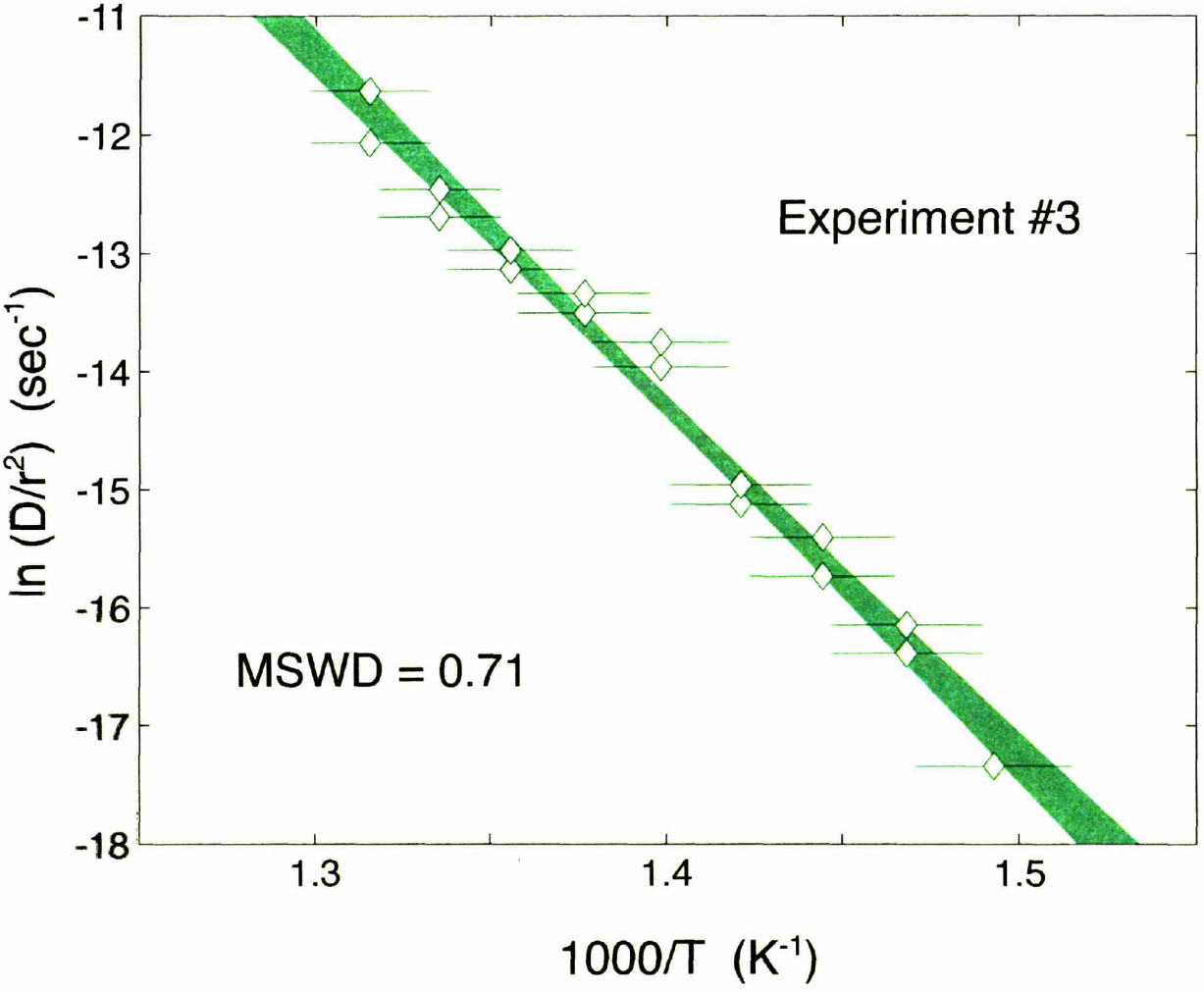
-11
-12
-13
-14
-15
-16
-17
-18
ln (D/r²) (sec⁻¹)
Experiment #3
MSWD = 0.71
1.3
1.4
1.5
1000/T (K⁻¹)

Figure 3a

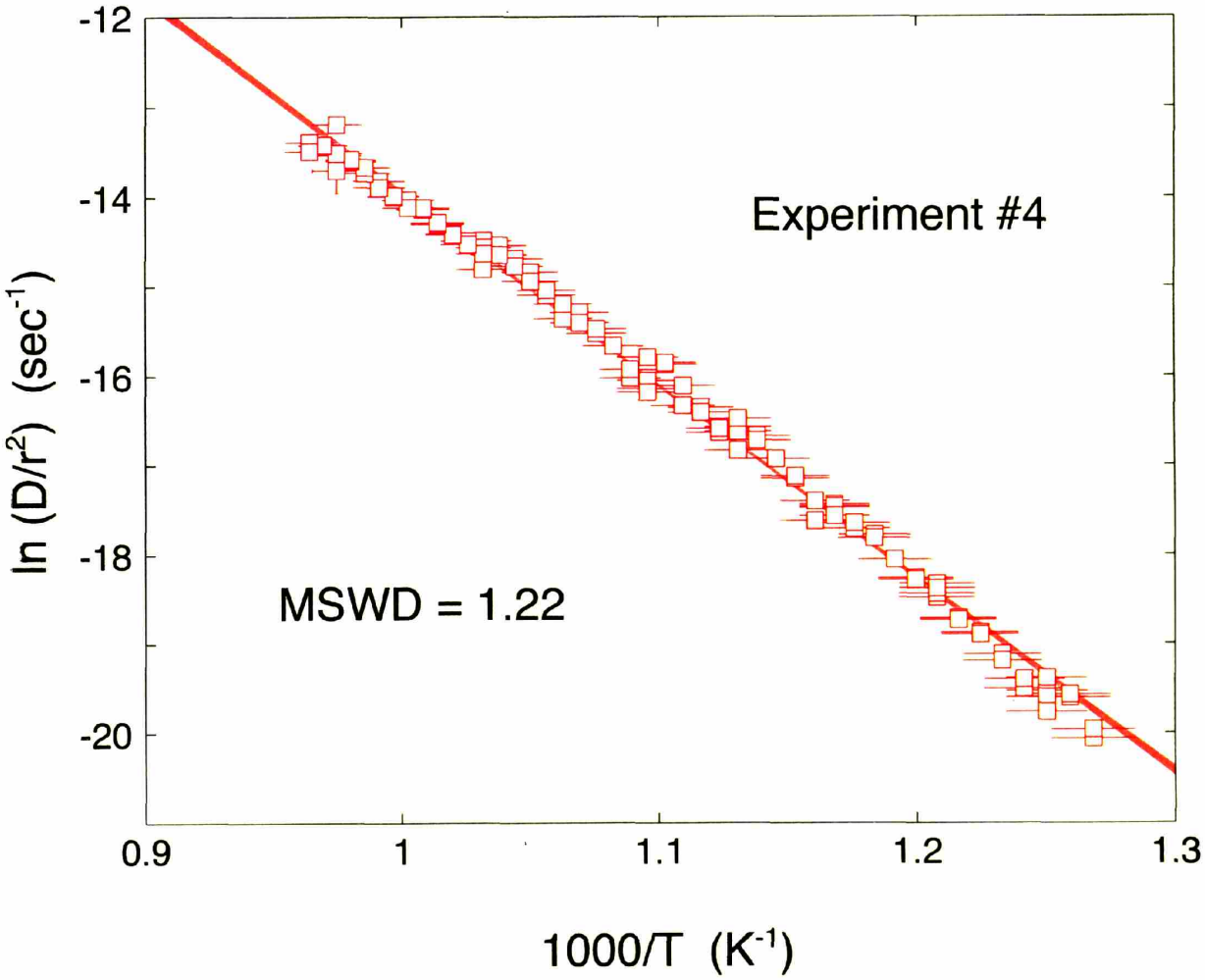
-12
-14
-16
-18
-20
ln (D/r²) (sec⁻¹)
Experiment #4
MSWD = 1.22
0.9
1
1.1
1.2
1.3
1000/T (K⁻¹)

Figure 3b

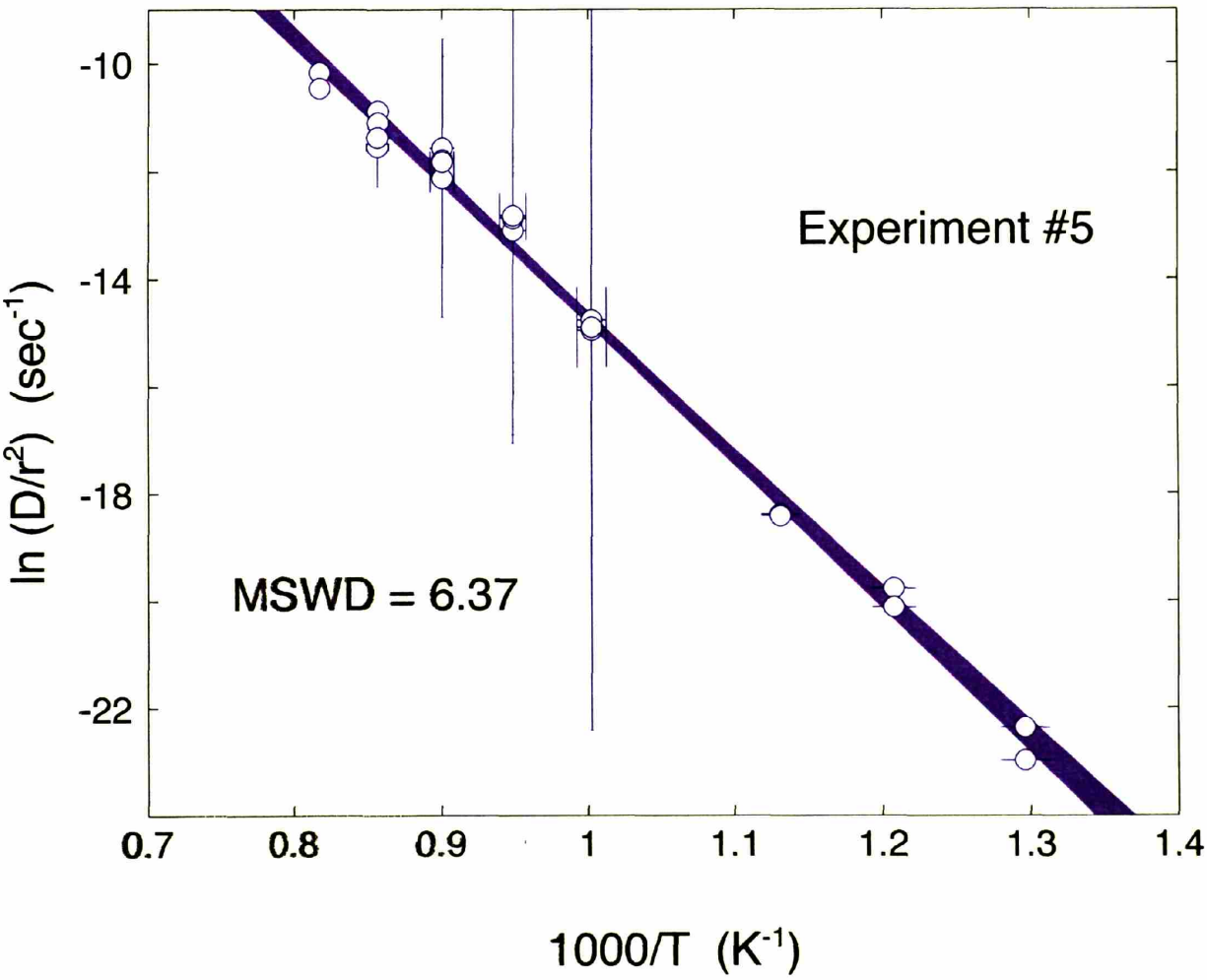
-10
-14
-18
-22
ln (D/r²) (sec⁻¹)
Experiment #5
MSWD = 6.37
0.7
0.8
0.9
1
1.1
1.2
1.3
1.4
1000/T (K⁻¹)

Figure 3c

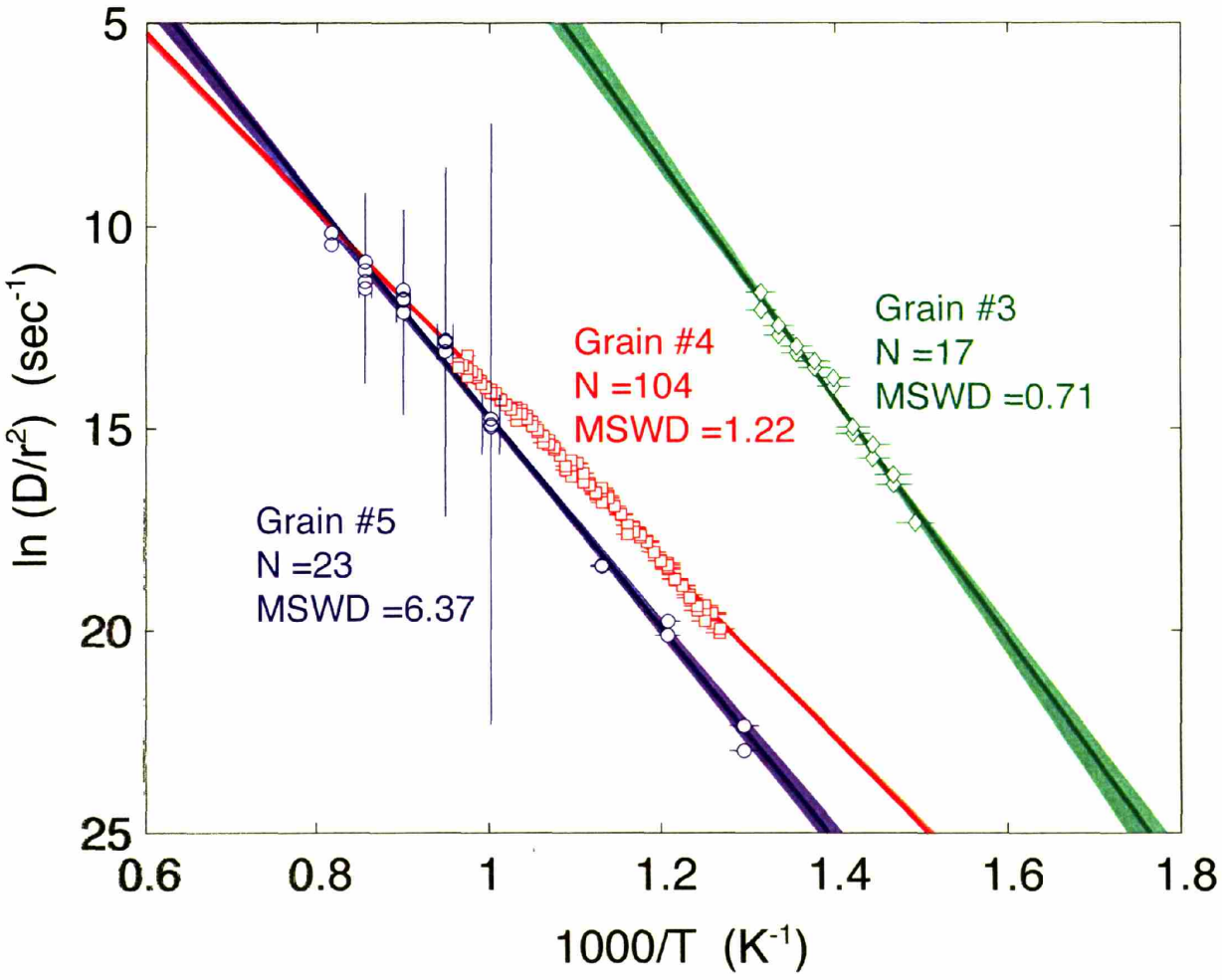
5
10
15
20
25
0.6
0.8
1
1.2
1.4
1.6
1.8
ln (D/r²) (sec⁻¹)
1000/T (K⁻¹)
Grain #3
N =17
MSWD =0.71
Grain #4
N =104
MSWD =1.22
Grain #5
N =23
MSWD =6.37

Figure 4

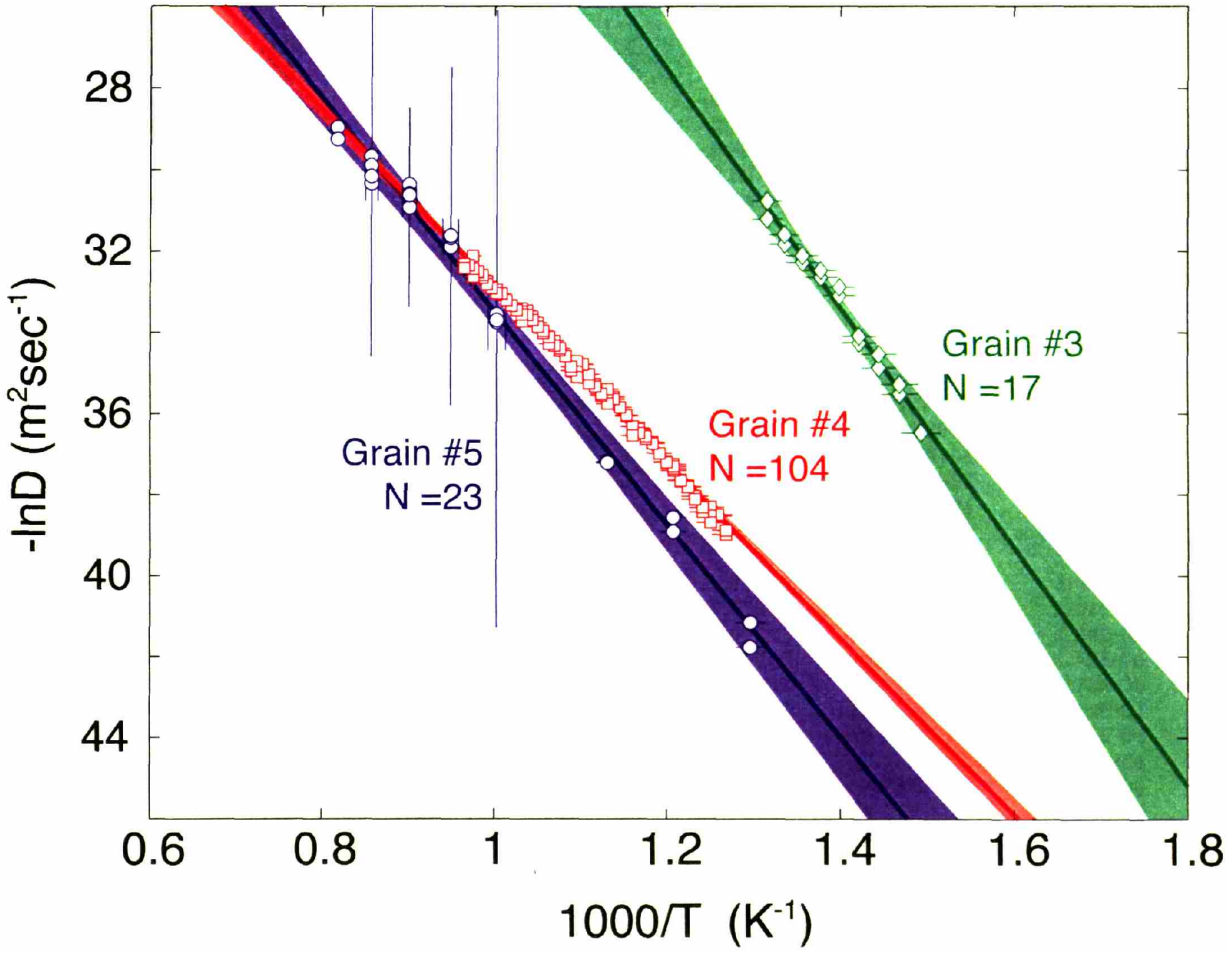
28
32
36
40
44
-lnD (m²sec⁻¹)
0.6
0.8
1
1.2
1.4
1.6
1.8
1000/T (K⁻¹)
Grain #5
N =23
Grain #4
N =104
Grain #3
N =17

Figure 5

Table 1 **Step-heating results**

	Grain 3						
step	**T (C)**	**time (min.)**	**He (moles)**	**He 2s (moles)**	***f***	**ln(D/a2)**	**ln(D/a2) 2s**
1	397	180	1.022E-14	2.0E-16	0.063	-17.3408351	2.24E-06
2	408	180	1.228E-14	1.6E-16	0.113	-16.3864003	4.54E-06
3	408	180	9.94E-15	1.4E-16	0.153	-16.144672	2.37E-05
4	419	180	1.093E-14	2.2E-16	0.198	-15.73379	1.12E-04
5	419	180	1.156E-14	1.1E-16	0.245	-15.40235	1.06E-04
6	431	180	1.197E-14	8.9E-17	0.293	-15.12223	8.14E-05
7	431	180	1.138E-14	1.1E-16	0.340	-14.95832	2.70E-04
8	442	120	1.638E-14	7.7E-17	0.406	-13.95675	1.41E-04
9	442	120	1.580E-14	7.8E-17	0.471	-13.74640	2.13E-04
10	453	120	1.601E-14	6.8E-17	0.536	-13.50051	2.65E-04
11	453	120	1.511E-14	7.8E-17	0.597	-13.33424	4.58E-04
12	465	120	1.485E-14	7.5E-17	0.657	-13.1317	8.77E-04
13	465	120	1.397E-14	1.0E-16	0.714	-12.9693	1.82E-03
14	476	120	1.448E-14	7.7E-17	0.773	-12.6894	3.47E-03
15	476	120	1.377E-14	5.8E-17	0.829	-12.457	5.52E-03
16	487	120	1.426E-14	7.2E-17	0.887	-12.067	8.08E-03
17	487	120	1.302E-14	5.3E-17	0.940	-11.629	1.39E-02

	Grain 4						
step	**T (C)**	**time (min.)**	**He (moles)**	**He 2s (moles)**	***f***	**ln(D/a2)**	**ln(D/a2) 2s**
1	515	120	8.580E-14	1.6E-16	0.025	-20.058774778	4.84E-08
2	515	120	8.300E-14	1.6E-16	0.028	-19.95843673	8.50E-08
3	521	120	1.0400E-13	2.0E-16	0.032	-19.60259601	8.50E-08
4	521	120	9.529E-14	1.4E-16	0.036	-19.56694805	1.13E-07
5	527	120	8.955E-14	1.6E-16	0.040	-19.52642281	2.29E-07
6	527	120	9.440E-14	1.4E-16	0.043	-19.38050538	2.56E-07
7	527	120	7.018E-14	1.3E-16	0.046	-19.59801	1.14E-04
8	527	120	5.635E-14	1.3E-16	0.048	-19.7619557	3.07E-06
9	532	120	6.940E-14	1.4E-16	0.051	-19.5011933	1.91E-06
10	532	120	7.285E-14	1.5E-16	0.054	-19.3960657	1.94E-06
11	538	120	9.060E-14	1.6E-16	0.057	-19.1165140	1.49E-06
12	538	120	7.928E-14	1.3E-16	0.061	-19.1894575	1.75E-06
13	544	120	1.0228E-13	1.3E-16	0.065	-18.8736106	7.18E-07
14	544	120	9.414E-14	1.9E-16	0.068	-18.8938771	2.57E-06
15	549	120	1.0626E-13	1.8E-16	0.072	-18.7123267	2.76E-06
16	549	120	9.843E-14	1.8E-16	0.076	-18.7302950	3.28E-06
17	555	120	1.1924E-13	2.5E-16	0.081	-18.4793895	3.24E-06
18	555	120	1.1698E-13	2.2E-16	0.085	-18.4376468	4.53E-06
19	555	120	1.2328E-13	2.4E-16	0.090	-18.32520	3.37E-04
20	555	120	1.1074E-13	1.9E-16	0.095	-18.377996	1.07E-05
21	561	120	1.1840E-13	2.5E-16	0.099	-18.260072	7.74E-06
22	561	120	1.1068E-13	2.0E-16	0.104	-18.278611	1.01E-05
23	566	120	1.3200E-13	2.4E-16	0.109	-18.052691	7.60E-06
24	566	120	1.2534E-13	2.5E-16	0.114	-18.053895	1.11E-05
25	572	120	1.5720E-13	3.0E-16	0.120	-17.774184	8.54E-06
26	572	120	1.4317E-13	1.8E-16	0.125	-17.813478	1.00E-05
27	577	120	1.5151E-13	1.8E-16	0.131	-17.705903	5.85E-06
28	577	120	1.5313E-13	2.1E-16	0.137	-17.644683	7.76E-06
29	583	120	1.7900E-13	3.1E-16	0.144	-17.435614	1.01E-05
30	583	120	1.6403E-13	2.0E-16	0.151	-17.470426	1.34E-05
31	583	120	1.5825E-13	2.2E-16	0.157	-17.4578	1.02E-03
32	583	120	1.3643E-13	2.1E-16	0.162	-17.56421	6.49E-05
33	589	120	1.5493E-13	2.0E-16	0.168	-17.396740	2.26E-05
34	589	120	1.1942E-13	1.7E-16	0.173	-17.620199	3.96E-05
35	594	120	1.8491E-13	3.1E-16	0.180	-17.143203	2.20E-05
36	594	120	1.8078E-13	2.8E-16	0.187	-17.119378	3.18E-05
37	600	120	2.0915E-13	2.2E-16	0.195	-16.925748	1.89E-05
38	600	60	1.0086E-13	1.8E-16	0.199	-16.92504	1.10E-04

39	606	60	1.2710E-13	1.6E-16	0.204	-16.66717	7.69E-05
40	606	60	1.1745E-13	1.8E-16	0.209	-16.71809	9.88E-05
41	611	60	1.3262E-13	2.2E-16	0.214	-16.56852	1.06E-04
42	611	60	1.2269E-13	2.1E-16	0.219	-16.61811	1.52E-04
43	611	60	1.3734E-13	2.0E-16	0.224	-16.4755	1.78E-03
44	611	60	9.3993E-14	1.4E-16	0.228	-16.83016	4.67E-04
45	617	60	1.1231E-13	1.6E-16	0.232	-16.63047	1.71E-04
46	617	60	1.1458E-13	1.3E-16	0.237	-16.58694	1.41E-04
47	623	60	1.4158E-13	2.2E-16	0.242	-16.34918	1.21E-04
48	623	60	1.3020E-13	1.8E-16	0.247	-16.40565	1.69E-04
49	628	60	1.3691E-13	1.8E-16	0.253	-16.32901	1.18E-04
50	628	60	1.6591E-13	2.1E-16	0.259	-16.10737	9.77E-05
51	634	60	2.0321E-13	1.9E-16	0.267	-15.86930	5.55E-05
52	634	60	1.9956E-13	2.6E-16	0.275	-15.84970	6.21E-05
53	640	60	1.4444E-13	1.7E-16	0.280	-16.14135	1.40E-04
54	640	60	1.9937E-13	2.4E-16	0.288	-15.78796	7.56E-05
55	640	60	1.4869E-13	2.0E-16	0.294	-16.0487	3.52E-03
56	640	60	1.2742E-13	1.7E-16	0.299	-16.1789	7.28E-04
57	645	60	1.4563E-13	2.1E-16	0.305	-16.02164	3.18E-04
58	645	60	1.5627E-13	2.2E-16	0.311	-15.92522	2.23E-04
59	651	60	1.9796E-13	2.4E-16	0.319	-15.65884	1.47E-04
60	651	60	1.9092E-13	2.4E-16	0.326	-15.66263	1.66E-04
61	657	60	2.1254E-13	3.0E-16	0.335	-15.52220	1.78E-04
62	657	60	2.1583E-13	2.4E-16	0.343	-15.47216	1.87E-04
63	662	60	2.5003E-13	3.4E-16	0.353	-15.28791	1.33E-04
64	662	60	2.1503E-13	2.1E-16	0.361	-15.40216	1.83E-04
65	668	60	2.1805E-13	2.2E-16	0.370	-15.35462	1.22E-04
66	668	60	2.4760E-13	3.0E-16	0.379	-15.19180	1.30E-04
67	674	60	2.6331E-13	3.4E-16	0.390	-15.09162	1.62E-04
68	674	60	2.6723E-13	3.0E-16	0.400	-15.03717	1.91E-04
69	679	60	3.1291E-13	3.8E-16	0.412	-14.83652	1.58E-04
70	679	60	2.7149E-13	2.1E-16	0.423	-14.93586	2.06E-04
71	685	60	3.3403E-13	2.3E-16	0.436	-14.68482	6.71E-05
72	685	60	2.9403E-13	3.0E-16	0.447	-14.76751	1.20E-04
73	690	60	3.5399E-13	3.3E-16	0.461	-14.53599	1.06E-04
74	690	60	3.0421E-13	3.7E-16	0.473	-14.64132	2.41E-04
75	696	60	3.4118E-13	4.2E-16	0.486	-14.48154	2.57E-04
76	696	60	3.0230E-13	2.9E-16	0.498	-14.55785	3.60E-04
77	696	60	2.2806E-13	2.3E-16	0.507	-14.801	8.23E-03
78	696	60	2.6180E-13	3.1E-16	0.518	-14.6294	2.34E-03
79	702	60	2.9074E-13	3.1E-16	0.529	-14.4865	9.46E-04
80	702	60	2.6910E-13	3.3E-16	0.539	-14.5253	7.46E-04
81	707	60	2.9243E-13	3.1E-16	0.551	-14.4034	5.14E-04
82	707	60	2.7772E-13	2.7E-16	0.562	-14.4157	5.71E-04
83	713	60	3.0016E-13	3.4E-16	0.573	-14.2980	5.88E-04
84	713	60	2.9275E-13	3.6E-16	0.585	-14.2819	8.70E-04
85	719	60	3.2498E-13	3.4E-16	0.597	-14.1343	7.36E-04
86	719	60	3.1606E-13	3.8E-16	0.610	-14.1171	6.88E-04
87	724	60	3.2984E-13	2.6E-16	0.623	-14.0287	6.60E-04
88	724	60	2.9015E-13	2.9E-16	0.634	-14.1126	7.87E-04
89	730	60	3.1334E-13	3.2E-16	0.646	-13.9921	8.46E-04
90	730	60	3.0283E-13	2.9E-16	0.658	-13.9812	1.13E-03
91	736	60	3.3969E-13	3.9E-16	0.671	-13.8186	9.31E-04
92	736	60	3.0106E-13	3.0E-16	0.683	-13.8910	1.50E-03
93	741	60	3.3720E-13	4.3E-16	0.696	-13.7285	1.79E-03
94	741	60	3.4117E-13	2.8E-16	0.709	-13.6636	1.63E-03
95	747	60	3.4555E-13	4.5E-16	0.723	-13.5955	1.52E-03
96	747	60	3.3205E-13	3.6E-16	0.736	-13.5793	2.24E-03
97	753	60	4.5839E-13	4.9E-16	0.754	-13.1890	1.28E-03
98	753	60	3.0359E-13	3.0E-16	0.765	-13.5333	3.13E-03
99	753	30	1.2285E-13	1.7E-16	0.771	-13.70	2.15E-01
100	753	30	1.4562E-13	1.6E-16	0.776	-13.51	1.08E-01

101	758	30	1.5406E-13	1.9E-16	0.782	-13.42	7.58E-02
102	758	30	1.5005E-13	1.5E-16	0.788	-13.42	5.05E-02
103	764	30	1.5029E-13	2.4E-16	0.794	-13.388	4.01E-02
104	764	30	1.3191E-13	2.3E-16	0.799	-13.49	6.11E-02

	Grain 5						
step	**T (C)**	**time (min.)**	**He (moles)**	**He 2s (moles)**	***f***	**ln(D/a2)**	**ln(D/a2) 2s**
1	498	120	3.019E-14	9.13E-17	0.0029	-22.97232516154	7.09E-11
2	498	120	2.066E-14	7.61E-17	0.0050	-22.3628990614	9.63E-10
3	555	120	1.0684E-13	1.99E-16	0.0154	-19.768828954	1.04E-09
4	555	120	4.354E-14	8.83E-17	0.0196	-20.11835309	1.26E-08
5	611	90	1.2460E-13	1.59E-16	0.0318	-18.388152354	5.02E-09
6	611	90	8.602E-14	1.42E-16	0.0402	-18.414452748	3.56E-08
7	724	60	7.978E-13	1.11E-15	0.1181	-14.952399131	3.75E-08
8	724	60	5.0752E-13	7.77E-16	0.1677	-14.76246886	2.72E-07
9	781	60	1.4589E-12	1.74E-15	0.3101	-13.09235500	3.45E-07
10	781	60	1.0758E-12	1.60E-15	0.4151	-12.8463816	3.42E-06
11	837	60	2.1428E-12	2.20E-15	0.6244	-11.5603013	3.49E-06
12	837	60	9.995E-13	9.23E-16	0.7220	-11.779227	1.86E-05
13	894	60	1.4271E-12	1.81E-15	0.8613	-10.873975	4.25E-05
14	894	60	5.958E-13	6.84E-16	0.9195	-11.08744	3.63E-04
15	950	60	6.158E-13	6.33E-16	0.9796	-10.1614	1.45E-03
16	950	60	1.3414E-13	2.22E-16	0.9927	-10.452	3.52E-02
17	894	120	3.751E-14	8.11E-17	0.9964	-11.5	4.29E+00
18	894	120	2.102E-14	5.24E-17	0.9984	-11.36	2.07E-01
19	837	120	5.235E-15	3.59E-17	0.9989	-12.1	2.29E+00
20	837	120	4.527E-15	3.83E-17	0.9994	-11.8	1.55E+00
21	781	120	1.104E-15	2.67E-17	0.9995	-12.9	4.02E+00
22	781	120	9.64E-16	2.13E-17	0.9996	-12.8	4.58E+00
23	724	180	1.599E-16	2.23E-17	0.9996	-15	7.90E+00

CHAPTER 3

Laser microprobe (U-Th)/He geochronology

Boyce, J.W., Hodges, K.V., Olszewski, W.J., Jercinovic, M.J.,

Carpenter, B.D., and Reiners, P.W.

As submitted to:

Geochimica Cosmochimica Acta (2005)

Abstract

A new analytical method had been developed to enable high-spatial-resolution (U-Th)/He dating of accessory minerals. It involves the use of a focused ArF excimer to ablate pits in a polished grain surface, with the evolved gases spiked for isotope-dilution measurement of radiogenic ^{4}He. These data are converted to concentrations by precise measurement of each pit using an optical interferometric microscope. U, Th, and Sm concentration measurements are made using one of several alternative microanalytical techniques (e.g., wavelength-dispersive electron microprobe analysis or laser-ablation, inductively coupled plasma mass spectrometry). By way of illustration, we present both conventional and laser microprobe (U-Th)/He dating results for a Brazilian monazite sample. Laser microprobe data (28 measurements on two crystal fragments) yield a weighted mean (U-Th)/He date of 455.3 ± 3.7 Ma (2SE). This result is statistically indistinguishable from the mean conventional (U-Th)/He date for three separate grain fragments: 449.6 ± 9.8 Ma (2SE). The agreement of conventional and laser ablation dates should encourage a wide variety of applications of the technique, including: 1) detrital mineral dating for provenance and unroofing studies; 2) the dating of broken, included, highly zoned, or irregular grains which are not easily corrected for alpha-ejection; and 3) measuring ^{4}He loss profiles that can be inverted to determine cooling histories.

Introduction

The oldest method of isotopic dating, (U-Th)/He geochronology has enjoyed a renaissance over the past few years and has become an important tool for a wide variety of earth science studies (e.g. House et al. 1998; Min et al. 2003; e.g. Tagami et al. 2003). Nevertheless, the technique is still in a developmental stage; as new accessory minerals are calibrated for (U-

Th)/He chronometry, efforts continue to refine and improve analytical methodologies. Here we introduce a new analytical approach that addresses two major problems encountered in conventional (U-Th)/He geochronology. The first is the need to correct single-crystal dates for the loss of radiogenic ^{4}He by alpha-particle ejection (Farley et al. 1996). The second is the propensity of accessory minerals to display complex chemical zoning patterns that both complicate the alpha-ejection correction (Hourigan et al. 2005) and cloud the assignment of an unambiguous closure temperature to a particular (U-Th)/He date (e.g. Boyce et al. in press).

Unlike the well-established use of defocused lasers to heat and consequently degas individual crystals for He analysis (House et al. 2000), the new method described here involves the use of an excimer laser to ablate small pits in the polished surface of a mineral in order to extract gas for He isotopic measurements. Concentrations of U, Th, and Sm are then measured on the same surface using one of several microanalytical instruments, the choice of which depends largely on the abundance of the parent elements in the dated mineral. We demonstrate the viability of the method by comparing conventional and laser microprobe dates for gem-quality Brazilian monazite with the application of the two methods yielding statistically indistinguishable results. In addition, this exercise shows how replicate laser microprobe analyses can – in some cases – be combined to increase the precision of (U-Th)/He dates beyond the level normally obtained using the conventional approach.

Method Description

Laser microprobe (U-Th)/He dating involves eight steps, diagrammed in Figure 1: 1) mounting and polishing of a crystal fragment in preparation for electron microprobe analysis; 2) characterizing the crystal via backscattered electron (BSE), cathodoluminescence (CL) or X-ray

mapping; 3) remounting the crystal in indium for helium analysis; 4) ablating pits in the polished surface to extract gasses; 5) isolating and analyzing the extracted He; 6) measuring the volume of the ablated pit; 7) measuring concentrations of U, Th, and Sm in or in close proximity to the pit ablated for He extraction; and finally 8) the calculation of apparent ages and uncertainties.

Sample Selection and Preparation

As is the case for other (U-Th)/He dating techniques, laser microprobe studies require careful hand-picking of crystals or crystal fragments that are free of optically visible inclusions or signs of alteration. The minimum grain size suitable for the technique depends on the concentration of radiogenic ^{4}He in the sample. Unless they are very old or very large, most apatites and titanites – minerals frequently used for conventional (U-Th)/He thermochronology (Reiners and Farley 1999; Farley 2000) – are not sufficiently rich in radiogenic ^{4}He, given current analytical limitations. Zircon, xenotime, and monazite (Farley and Stockli 2002; Reiners in press) have higher concentrations of U and Th (and therefore ^{4}He), and are more amenable to laser microprobe analysis. Practically speaking, samples of these minerals with grain sizes of 200 μm or larger are ideal, but we have worked successfully with samples as small as 60 μm.

The epoxy used to make grain mounts for many kinds of microanalytical projects in geochemistry are unsuitable for (U-Th)/He work because volatiles trapped in cured epoxy can stream off the grain mount in an ultrahigh vacuum extraction line, resulting in poor He isotopic analyses. Thus the technique requires a two-step, grain-mounting process. First, the fragment is mounted in epoxy and polished by hand to 0.05 μm, assuring a flat and smooth starting surface. Then, the grain is plucked from the epoxy and the fragment is placed on a glass slide – polished face down – and a nugget of indium is pressed on to the crystal to form an indium mount. The

two-step approach is necessary because, although indium is sufficiently malleable for this method to produce a relatively sturdy mount for He analysis, the grain is not sufficiently well encased by the indium to permit grinding and polishing without it being plucked out in the process.

Characterization of Samples

Because many accessory minerals exhibit complex chemical zoning that can result in apparent (U-Th)/He age variations, it is advantageous to develop a compositional map of the grain prior to He analysis. This can be done relatively easily by applying a conductive coating material to the surface of the initial epoxy mount and acquiring the desired backscattered electron and/or cathodoluminescence maps with an electron microprobe. One potential problem with adding this step to the sample preparation procedure is the possibility that the electron beam may cause He degassing near the sample surface, but our work thus far has not shown evidence of this phenomenon. The effect is likely minimized by the need to re-polish the sample after imaging to remove the conductive coating of carbon or gold, as the upper micron or two of sample itself is usually removed along with the coating.

Laser Ablation

Helium extraction for (U-Th)/He microanalysis requires the use of an instrument capable of the controlled excavation of a sample pit. Although ion microprobes are suitable for this application, our efforts have focused on the use of laser technology. The way in which a laser beam interacts with a crystal depends on the material's absorbed energy density for the wavelength of interest (Ready 1971). We wish to achieve laser ablation, which can be defined

for our purposes as the vaporization of a well-defined volume without significant heating of the surrounding material. Excimer lasers are excellent tools for ablation for a variety of reasons. First, the short-wavelength energy they produce is absorbed well by all minerals used for (U-Th)/He geochronology. Second, they produce extremely stable and well-defined beams that result in ablation pits that are geometrically simple and easily measured (Figure 2). Finally, they are capable of producing focused beams with extremely high energy densities and thus ablate with no discernable effect on the material outside the ablation pit.

Gas Purification and Helium Isotopic Measurement

Prior to the experiment, the indium grain mount is placed on a copper or stainless steel planchette in a 6.875 cm diameter, ultrahigh-vacuum sample chamber fitted with a silica viewport that permits transmission of the laser beam. The chamber is mounted on a computer-controlled stage and connected to a gas purification system such as those used for conventional (U-Th)/He geochronology. In general, the low sample gas volumes produced during laser ablation mean that less gettering capacity is required than for conventional analyses, and that the gas cleanup may be done more rapidly. As is the case with conventional (U-Th)/He analyses, helium isotopic data can be measured for laser ablation studies with sufficient precision using a small quadrupole mass spectrometer.

Ablation Pit Measurement

After analysis, the sample is removed from vacuum chamber and volumes of ablation pits are measured. A variety of alternative devices can be used for these measurements, including mechanical profilometers, confocal laser microscopes, and optical interferometric microscopes.

In the course of our proof-of-concept study, described here, we found that the precision and accuracy of these measurements contributes greatly to the overall success of the technique. For this reason, we have chosen the optical interferometric microscope for our volume measurements.

U, Th, and Sm Measurements

Once the pits have been measured, the grain mount is ready for U, Th, and Sm measurements. For zircons, one of the most widely available instruments for such measurements is a laser-ablation cell attached to an inductively coupled plasma mass spectrometer (LA-ICPMS), Our preferred protocol for laser microprobe (U-Th)/He dating of zircon involves re-occupying the pre-existing ablation pit with the laser used for LA-ICPMS analysis; by drilling the pre-existing hole slightly wider and deeper to extract material for trace element analysis, this approach minimizes the effects of sample heterogeneity on calculated dates. For monazite and xenotime, measurements of sufficient quality can be done with an electron microprobe. In practice, U, Th, and Sm can be measured prior to He analysis (concurrent with electron microprobe mapping), or a number of spots surrounding the ablation pits can be measured after ablation.

Age Calculation

After calculation of ^{4}He concentrations from ^{4}He molar and pit volume data, parent and daughter concentrations can be combined in the (U-Th)/He decay equation (Farley et al. 2002), in order to solve iteratively for age. Uncertainties are calculated via a *Monte Carlo* method (e.g. Press et al. 1992), assuming normally distributed uncertainties for U, Th, Sm, He, and volume

measurements. For most analyses, at least ~75% of the total age uncertainty stems from the uncertainty in the volume measurement. In contrast, all three parent elements (U, Th, and Sm) contribute no more than a total of ~15%, and helium measurements are responsible for only ~10% of the total uncertainty. In a case where individual pits are expected to yield equivalent ages, such as the proof-of-concept case described here, the weighted mean and standard error of the mean of all of the independent age determinations produces a reliable estimate of the cooling age of the sample.

Comparative Conventional and Laser Microprobe Dating of Brazilian Monazite

In order to demonstrate the laser microprobe method, we present here the results of a study of a gem-quality, orange-brown monazite from Ataleia in the Minas Gerais state of Brazil. We worked on two large (~ 1 cm^3) fragments that exhibited sharp crystal faces, MOM1 and MOM3. Backscattered electron and X-ray mapping using the Cameca SX-Ultrachron at the University of Massachusetts at Amherst showed no discernable indication of chemical zoning in Y, Sm, U, or Th within these crystals. X-ray diffraction analysis of a fragment of MOM1 by M. Donohue in the Department of Physics at Harvard University resulted in values of a = 6.77355 Å, b = 6.9963 Å, c = 6.4850 Å, and ß = 103.627°. The excellent agreement of these results with established values (e.g. Ni et al. 1993; Ni et al. 1995) suggests a well-defined crystal structure that has not been compromised by radiation damage that might affect He retentivity (Garver et al. 2005).

Conventional (U-Th)/He Analyses

The MOM3 crystal was crushed and three fragments were dated at Yale University.

Analytical procedures for the conventional laser-heating monazite (U-Th-Sm)/He ages followed routine procedures used for zircon (Reiners in press), except small crystal fragments were analyzed and no alpha-ejection corrections were made (these fragments were carefully selected to be from the interior of the crystal and more than 20 μm away from the nearest crystal face so as to eliminate the need to correct the He results for alpha-particle ejection (Farley et al. 1996)). Roughly equidimensional, 30 - 60 μm diameter crystal fragments of MOM3 were wrapped in ~ 1 mm Nb foil packets. The foils then were placed in a Cu planchette, the planchette was overlain with a KBr cover slip, and the entire assembly was sealed within an ultrahigh-vacuum ($\sim 10^{-9}$ Torr) sample chamber connected to the He purification/measurement line. For He extraction, each foil was heated to ~ 1000-2000°C for fifteen minutes using a 1064 nm Nd:YAG laser focused through a sapphire viewport. Re-heating and re-extracts of each sample yielded negligible ^{4}He (< 0.05% of initial extraction). Extracted gas was spiked with ~ 8×10^{-13} moles of ^{3}He, cryogenically concentrated, purified additionally by gettering, and expanded into a gas-source quadrupole mass spectrometer. ^{4}He/^{3}He was measured for about ten seconds following gas release and nominal equilibration time. the results were corrected for background and interferences on mass 3 (HD+ and H_3+), and compared with the ^{4}He/^{3}He measured on pipetted aliquots of a manometrically calibrated ^{4}He standard processed by the same methods. ^{4}He in the unknown sample is assumed to be the product of the ^{4}He content of the standard with the ratio of the ^{4}He/^{3}He measurements on the unknown and the standard. Linearity of this calibration approach has been confirmed in the Yale helium lines over about four orders of magnitude of ^{4}He signal. Samples were processed with several "hot blanks" and "line blanks" to check the measured ^{4}He/^{3}He of laser extraction procedures on empty Nb foil envelopes, and ^{4}He/^{3}He of ^{3}He-only shots. Nominal ^{4}He blanks from these procedures range from 0.05 to 0.1 fmol; the

measured ^{4}He of these monazite aliquots was 6-7 pmol).

Parent nuclide contents of degassed monazites were measured by isotope dilution and solution ICPMS. Monazite-bearing Nb-foils were spiked with 0.4 ng of ^{233}U, 0.6 ng of ^{229}Th, and 0.6 ng of ^{147}Sm. Foil, crystal, and spike were bombed in Teflon vials at 225 °C for 72 hours. Samples were then heated to dryness, after which they were re-bombed and dissolved in HCl at 200 °C for 24 hours to re-dissolve refractory fluoride salts. After a final drydown, the sample was re-dissolved in 6% HNO3 and 0.8% HF, and this solution (~ 2 - 4 ml total) was introduced to the ICPMS via an all-PFA sample introduction system with a sapphire injector. Ratios of ^{238}U/^{233}U, ^{232}Th/^{229}Th, and ^{152}Sm/^{147}Sm were quantified by 2000 measurements of the average intensities in the middle 10% of peak widths in low-resolution mode on an Element2 high-resolution ICP-MS. ^{238}U/^{235}U is also measured to check reagents for Pt contamination and mass fractionation. U and Th contents were calculated from multiple determinations of isotope ratios on pure spike and spiked normals containing 1 - 4 ng of isotopically normal U and Th. Procedural blanks for U and Th are determined by processing empty Nb foil envelopes, and average about 2 and 5 pg for U and Th, respectively.

The results of the conventional analyses (Table 1) are statistically indistinguishable and the three derived dates (450 ± 17 Ma (2σ), 449 ± 17, 450 ± 18) can be combined to report a weighted mean (U-Th)/He age of 449.6 Ma for MOM3 with an uncertainty – quoted at two standard errors of the weighted mean (2SE) – of 9.8 Ma.

Laser Microprobe (U-Th)/He Analyses

Sections through MOM1 and MOM3 were polished and mounted in indium for laser ablation. For the proof-of-concept study reported here, we used a Lambda Physik Compex 102

ArF excimer laser fitted to a New Wave Research DUV-193 beam preparation and targeting system at MIT. Lasing in the deep ultraviolet part of the spectrum at 193 nm, this system is capable of producing flux densities of greater than 100 TWm^{-2}. By applying 10 - 20 pulses of 100 mJ energy at a lasing duration of 2 - 4 seconds and pulse frequency of 4 – 10 Hz, we were able to ablate pits into the prepared sample surfaces that are approximately 25 μm in diameter and ~ 3 - 6 μm in depth. In all cases, these pits were more than 20 μm inside the crystal margins and thus the laser microprobe He measurements (like the conventional measurements) need not be corrected for alpha-particle ejection. As described earlier, the liberated gasses were spiked and purified and their isotopic composition measured by isotope dilution analysis. The mixture of ^{3}He and ^{4}He is passed over Saes C-400 and ST-172 cold getters to extract reactive gases, and the remainder is expanded into a Balzers Prisma 200 quadrupole mass spectrometer with a channeltron multiplier for measurement of ^{3}He and ^{4}He with a sensitivity of ~3500 A/mole. Total system blanks for ^{3}He are typically in the range of 1.5 x 10^{-16} moles, while ^{4}He blanks are ~ 3 x 10^{-15} moles. All measurements are made in a fixed-range mode, with unusually large gas loads accommodated by computerized shifts (for measurement of both isotopes) to higher fixed ranges. Analysis times, including ablation, range from 5 to 10 minutes per sample.

The resulting data were converted to ^{4}He concentrations using volume measurements of each pit. For this study, we used an ADE Phase Shift MicroXAM instrument. Vertical-scanning interferometers such as the MicroXAM rely on interference of a primary beam of light (~550 nm) with the light reflected from the surface. The interference pattern (a function of the height of the surface) is captured digitally as the stage is moved vertically, resulting in a 3-D map of the surface (Figure 3). Measurement of an ablation pit can be made in less than one minute, with a nominal lateral resolution of 0.5 μm and a vertical resolution of ~ 1 nm. After initial processing

with MapVue AE™ software to level the surface and interpolate missing pixels, custom software developed at MIT is used to calculate pit volumes. Replicate analyses indicate a reproducibility of ~1.5% (2σ) for volume measurements made with the MicroXAM, and we propagate a more conservative 2% uncertainty into all ages.

Major and trace element concentrations were measured for MOM1 and MOM3 using the Cameca SX-Ultrachron (Table 2). The most important measurements for our purposes were those of U, Th, and Sm, and we closely followed the analytical protocols for these elements outlined in Jercinovic and Williams (2005). In particular, care was taken to correct all U concentrations for overlap of the Th M-γ, Th M3-N4, the associated high energy M3-N4 satellite, and the Th M5-P3 lines with the U M-β peak. These analyses indicate that neither MOM1 and MOM3 are zoned in these three elements, but the two crystals are compositionally distinctive. For MOM1, we determined U = 1516 ± 11 ppm, Th = 83240 ± 130 ppm, and Sm = 30250 ± 370 ppm; for MOM3, the values were U = 1344 ± 14 ppm, Th = 63866 ± 77 ppm, and Sm = 27800 ± 1800 ppm. (For each, the errors are reported at 2SE.) The reason for this grain-to-grain inconsistency in composition is unknown, but we note that the lower average concentration of ^{4}He in pits from MOM3 (which has lower parent element abundances) is consistent with the discrepancy being real and not simply an analytical artifact.

In all, we determined eighteen laser microprobe (U-Th)/He ages for MOM1 (Figure 4, Table 2) with an error-weighted mean for all analyses of 453 ± 14 Ma (2σ). Ten ablation pits on the MOM3 section yield a similar weighted mean, albeit with more scatter, of 459 ± 25 Ma. Despite the compositional differences in MOM1 and MOM3, the two populations of ages are indistinguishable within error, and thus we can combine them all to determine a weighted mean age of 455 Ma for the MOM monazites. While two standard deviations of this mean is ~19 Ma, a

more useful statistic to describe our confidence in the calculated value is the standard error of the weighted mean. Thus, at the ~95% confidence level, we infer the (U-Th)/He age of the sample to be 455.3 ± 3.7 Ma. This result is well within uncertainty of the conventional (U-Th)/He date for MOM3 of 449.6 ± 9.8 Ma.

Discussion

The agreement of the weighted mean laser microprobe and conventional laser heating (U-Th)/He ages on this sample to within 1.3% indicates that laser microprobe (U-Th)/He geochronology can be used to produce robust cooling ages. The amount of scatter observed for individual spot ages is always less than 6% of the weighted mean age, comparable to the reproducibility in previous conventional (U-Th)/He studies (e.g., House et al. 2000; e.g., Reiners in press). However, it must be pointed out that the materials used in the conventional studies (unlike the monazite described here) contain parent element zonation likely responsible for some of their previously observed scatter (Boyce and Hodges 2005; Hourigan et al. 2005). Regardless, these results are encouraging, with the average deviation of the laser microprobe (U-Th)/He age from the weighted mean of the conventional monazite ages being less than 2%, which is approximately equal to the typical uncertainty on an individual spot age.

The variation that is observed (especially in MOM3) is likely caused by errors in the volume measurement. As mentioned in the description of the methodology, the uncertainty in the volume measurement is difficult to quantify. This is primarily because we must rely on the reproducibility of individual hole measurements to constrain the uncertainty. However, this does not account for any accuracy problems that may exist, nor any sensitivity of the volume measurement to the individual hole characteristics such as aspect ratio, wall steepness, pre-

ablation topography of the surface, or material reflectivity, any or all of which may change volume estimates.

One possible concern regarding the method is the extent to which ^{4}He is extracted unintentionally from the region around the ablation pit during the experiment. Ablation without extensive "collateral heating" is absolutely essential to the method because we must quantitatively extract all of the ^{4}He from a measurable volume in order to calculate the ^{4}He concentration, which is in turn used to calculate a date. If heating causes some ^{4}He to diffuse out of the surrounding material during the experiment, then we over-estimate both the concentration of ^{4}He in the volume and the (U-Th)/He age of the sample. Compared to other lasers commonly used in geochemical applications, the nanosecond-scale pulse rate of the ArF excimer implies very limited collateral heating – though more than would be expected from picosecond or femtosecond lasers. The most direct way we have to assess the impact of collateral heating on laser-ablation (U-Th)/He geochronology is through the comparison of laser microprobe (U-Th)/He and conventional (U-Th)/He ages. For the Brazilian monazite, the two techniques yield statistically indistinguishable ages. In addition, if collateral heating were a problem with the technique, we would anticipate different ages for different size ablation pits: larger pits with lower surface-area/volume ratios should yield younger ages than smaller pits. In our study, we ablated pits that varied in surface/volume ratio by roughly 20%, yet we found that the ages for the largest and smallest pits differed by less than 2%, and the pit with the larger surface/volume ratio was slightly younger, not older. Thus, we see no empirical evidence for ^{4}He released from the pit walls, and we conclude that collateral heating does not affect the accuracy of ArF excimer laser microprobe (U-Th)/He geochronology of monazite. However, such collateral heating may be an issue for U-Th)/He microprobe dating using other types of lasers, or ArF excimers

operated at conditions different from those we employed in this study.

The Added Value of Laser Microprobe (U-Th)/He Geochronology

The laser microprobe (U-Th)/He method yields more ages in a given amount of time than conventional methods despite the polishing and remounting required. This is primarily due to the substantial investment of time required to select crystals that are unbroken, inclusion-free, and have a regular geometry – all of which are necessary for robust alpha-ejection corrections. Since the laser microprobe can be used to specifically target portions of a grain that are farther that the nominal alpha-ejection distance from the grain rim, the alpha-ejection correction is rendered unnecessary. Typical alpha-ejection corrections for conventional (U-Th)/He ages range from 10% to more than 60% of the age. Ejection correction uncertainties are rarely propagated into the final age, and in most cases do not take into account possible uncertainties in the measurement of grains or heterogeneous parent element distributions. Such uncertainties – while typically ignored – should contribute substantially to the practical age uncertainty, and eliminating the need for such corrections should lead to improvements in the overall accuracy of (U-Th)/He dating. Because the new technique is insensitive to the external geometry of the crystal, grains that are otherwise difficult to date (or at least to date well) are now tractable. If no inclusion- and fracture-free, euhedral crystals are present in a particular mineral separate, laser-microprobe (U-Th)/He may provide the only means of extracting cooling age information from the sample.

An additional complication in conventional (U-Th)/He dating is chemical zonation. As recently demonstrated by Hourigan et al. (2005), intragrain variations in U and Th can result in errors in the ejection correction of 30% or more, even for "medium-sized" zircon crystals

(200μm x 100μm). Although it is possible to evaluate the likelihood of such errors in some cases through replicate analyses, intragrain variations in U and Th are sometimes systematic within a suite of crystals extracted from a single rock, resulting in a systematic but incorrect ejection correction (Tagami et al. 2003). With the laser microprobe technique, zoning patterns may be carefully characterized by cathodoluminescence or backscattered electron mapping and specific compositional domains can be dated. Such a capacity would be particularly valuable for monazite studies since composition may play a role in that mineral's ability to retain helium (Stockli et al. 2005; Boyce et al. in press). While the monazites used for this study are homogeneous, they are unusual in that regard, with most monazites containing complicated distributions of U, Th, and other trace elements (e.g. Boyce et al. in press). If different zones in a slowly cooled monazite retain radiogenic helium to different degrees, they would have different closure temperatures and therefore different cooling ages. Laser microprobe (U-Th)/He may be able to determine different ages for different zones of a heterogeneous crystal.

It also should be possible to measure ^{4}He depth profiles in minerals directly using the ~ 0.1 μm depth resolution of the excimer. Such profiles can be inverted to constrain cooling histories from single crystals, or simply used to expand the range of a thermochronometer by taking advantage of the core to rim variation in closure temperature (Dodson 1986). Depth profiles also could be used to directly measure alpha ejection profiles, in order to confirm the theoretical ejection distances commonly used in thermochronology. This could be done by sequentially ablating holes, measuring helium, then measuring the pit depth by optical interferometric microscopy as described in this study.

In principle, the technique described here also could be used to date minerals in polished rock sections. Preliminary experiments involving sequential polishing and back-scattered

electron mapping of rock sections suggest that this could be an efficient method for locating large numbers of small U- and Th-rich minerals such as monazite or zircon. Moreover, target minerals can be identified without loss of petrologic context, which may prove to be important in low-temperature thermochronometry when the crystals of interest are found as inclusions in large, highly retentive phases (such as garnet) that may retard ^{4}He diffusive loss from the inclusions.

Ultimately, the ability of this technique to produce large number of ages in a short time may prove to be most useful for the thermochronology of detrital samples. As demonstrated by Vermeesch (2004) and Anderson (2005), the utility of a detrital chronometry study is largely a function of being able to date a sufficient number of grains. In many instances, more than 100 dates are required for an adequate characterization of a polymodal detrital population. Picking more than 100 "perfect" crystals for a conventional (U-Th)/He study is likely to take many weeks of painstaking microscopy – if such crystals can be identified at all, since detrital grains are frequently abraded and or broken by fluvial transport. In the case of zircon, while the requirements for crystal perfection are somewhat more relaxed than for other minerals, the degassing and dissolutions are considerably more time consuming than the equivalent measurements of He, U, and Th using laser microprobes. With laser microprobe (U-Th)/He, detrital studies will be relatively straightforward and should quickly provide useful chronologic constraint for geologic studies of both modern and ancient sediments.

Conclusion

In this paper we have demonstrated that laser microprobe (U-Th)/He chronometry can be used to determine robust and reliable ages that are equivalent to conventional (U-Th)/He

measurements within uncertainties. For the MOM monazites described here, the conventional laser-heating (U-Th)/He age of 449.6 ± 9.8 Ma and the laser microprobe (U-Th)/He age of 455.3 ± 3.7 Ma agree within 1.3%, with the greatest outlier of the 28 individual laser microprobe spot ages corresponding to a deviation of only 7%. This compares favorably to estimates of reproducibility from previous conventional (U-Th)/He studies. The variation in individual ages observed is likely caused in large part by errors in volume measurements, and improvement of volume determinations should be the highest priority in efforts to improve the method. However, laser microprobe (U-Th)/He in its current state can provide large quantities of reliable ages in a short amount of time compared to conventional (U-Th)/He. In addition, use of the laser microprobe permits cooling age determinations from mineral separates lacking the euhedral, inclusion- and fracture-free crystals required for conventional (U-Th)/He. Finally, laser microprobe (U-Th)/He should allow direct measurement of ^{4}He depth profiles, allowing cooling histories and ejection distances to be determined on single crystals.

Acknowledgements

The development of this method over the past few years could not have progressed without the advice and encouragement of many persons, most notably S. Bowring, J. Crowley, and N. Chatterjee. This work was funded by grants from the National Science Foundation.

Figure Captions

Figure 1. Flow chart diagram of steps recommended for laser microprobe (U-Th)/He analyses. Standard flow chart symbols are used: rectangles indicate a process, parallelograms indicate data, and ellipses indicate termination, which in this case corresponds to the calculated age.

Solid lines with arrows represent direction of progress, while dashed lines indicate data paths.

Figure 2. Scanning electron microprobe image of typical ~25μm excimer ablation pits in the Brazilian monazite (MOM1).

Figure 3. Three-dimensional surface plot of an excimer ablation pit (~25μm diameter) in MOM1, as measured by a MicroXAM optical interferometer. Scale on all axes in micrometers.

Figure 4. Probability density (distribution) function (heavy solid black line) of laser microprobe (U-Th)/He analyses (black and white circles with 2σ error bars. Conventional (U-Th)/He data from Yale University shown as vertical line (weighted mean) with grey 95% confidence (2SE) bounds for reference.

Tables

Table 1. U, Th, Sm, He and ages (with 2σ uncertainties) for conventional (U-Th)/He geochronology.

Table 2. U, Th, Sm, He, volume, and ages, with 2σ uncertainties for laser microprobe (U-Th)/He.

References

Andersen, T. (2005). "Detrital zircons as tracers of sedimentary provenance: limiting conditions from statistics and numerical simulation." Chemical Geology **216**: 249-270.

Boyce, J. W. and K. V. Hodges (2005). "U and Th zoning in Cerro de Mercado (Durango, Mexico) fluorapatite: Insights regarding the impact of recoil redistribution of radiogenic ^{4}He on (U–Th)/He thermochronology." Chemical Geology **219**: 261-274.

Boyce, J. W., K. V. Hodges, et al. (in press). "He diffusion in monazite: Implications for (U-Th)/He thermochronometry." G-Cubed.

Dodson, M. H. (1986). "Closure profiles in cooling systems." Materials Science Forum **7**: 145-154.

Farley, K. A. (2000). "Helium diffusion from apatite; general behavior as illustrated by Durango fluorapatite." Journal of Geophysical Research, B, Solid Earth and Planets **105**(2): 2903-2914.

Farley, K. A., B. P. Kohn, et al. (2002). "The effects of secular disequilibrium on (U-Th)/He systematics and dating of Quaternary volcanic zircon and apatite." Earth and Planetary Science Letters **201**: 117-125.

Farley, K. A. and D. Stockli (2002). "(U-Th)/He dating of phosphates: apatite, monazite, and xenotime." Reviews in Mineralogy and Geochemistry **48**: 559-577.

Farley, K. A., R. A. Wolf, et al. (1996). "The effects of long alpha-stopping distances on (U-Th)/He ages." Geochimica et Cosmochimica Acta **60**(21): 4223-4229.

Garver, J. I., P. W. Reiners, et al. (2005). "Implications for timing of andean uplift from thermal resetting of radiation-damaged zircon in the Cordillera Huayhuash, northern Peru." Journal of Geology **113**: 117-138.

Hourigan, J. K., P. W. Reiners, et al. (2005). "U-Th zonation-dependent alpha-ejection in (U-Th)/He chronometry." Geochimica Cosmochimica Acta **69**(13): 3349-3365.

House, M. A., K. A. Farley, et al. (2000). "Helium chronometry of apatite and titanite using Nd-YAG laser heating." Earth and Planetary Science Letters **183**: 365-368.

House, M. A., B. P. Wernicke, et al. (1998). "Dating topography of the Sierra Nevada, California, using apatite (U-Th)/He ages." Nature (London) **396**(6706): 66-69.

Jercinovic, M. J. and M. L. Williams (2005). "Analytical perils (and progress) in electron microprobe trace element analysis applied to geochronology: Background acquisition, interferences, and beam irradiation effects." American Mineralogist **90**: 526-546.

Min, K., K. A. Farley, et al. (2003). "Single grain (U-Th)/He ages from phosphates in Acapulco meteorite and implications for thermal history." Earth and Planetary Science Letters **209**(3-4): 323-336.

Ni, Y., J. M. Hughes, et al. (1993). Crystal chemistry of natural and synthetic monazite-xenotime series. Geological Society of America, 1993 annual meeting, Boston, MA, United States.

Ni, Y., J. M. Hughes, et al. (1995). "Crystal Chemistry of the monazite and xenotime structures." American Mineralogist **80**: 21-26.

Press, W. H., S. A. Teukolsky, et al. (1992). Numerical Recipes in C: The Art of Scientific Computing. Cambridge, Cambridge University Press.

Ready, J. (1971). Effects of High-Power Laser Radiation. New York, Academic Press.

Reiners, P. W. (in press). Zircon (U-Th)/He thermochronometry. Thermochronology: Reviews in Mineralogy and Geochemistry. P. W. Reiners and T. A. Ehlers. Washington, DC, Mineralogical Society of America. **59**.

Reiners, P. W. and K. A. Farley (1999). "Helium diffusion and (U-Th)/He thermochronometry of titanite." Geochimica et Cosmochimica Acta **63**(22): 3845-3859.

Stockli, D., K. A. Farley, et al. (2005). "He diffusion and (U-Th)/He thermochronometry of monazite and rutile." Geochimica et Cosmochimica Acta **69**: A8.

Tagami, T., K. A. Farley, et al. (2003). "(U-Th)/He geochronology of single zircon grains of known Tertiary eruption age." Earth and Planetary Science Letters **207**(1-2): 57-67.
Vermeesch, P. (2004). "How many grains are needed for a provenance study?" Earth and Planetary Science Letters **224**: 441-451.

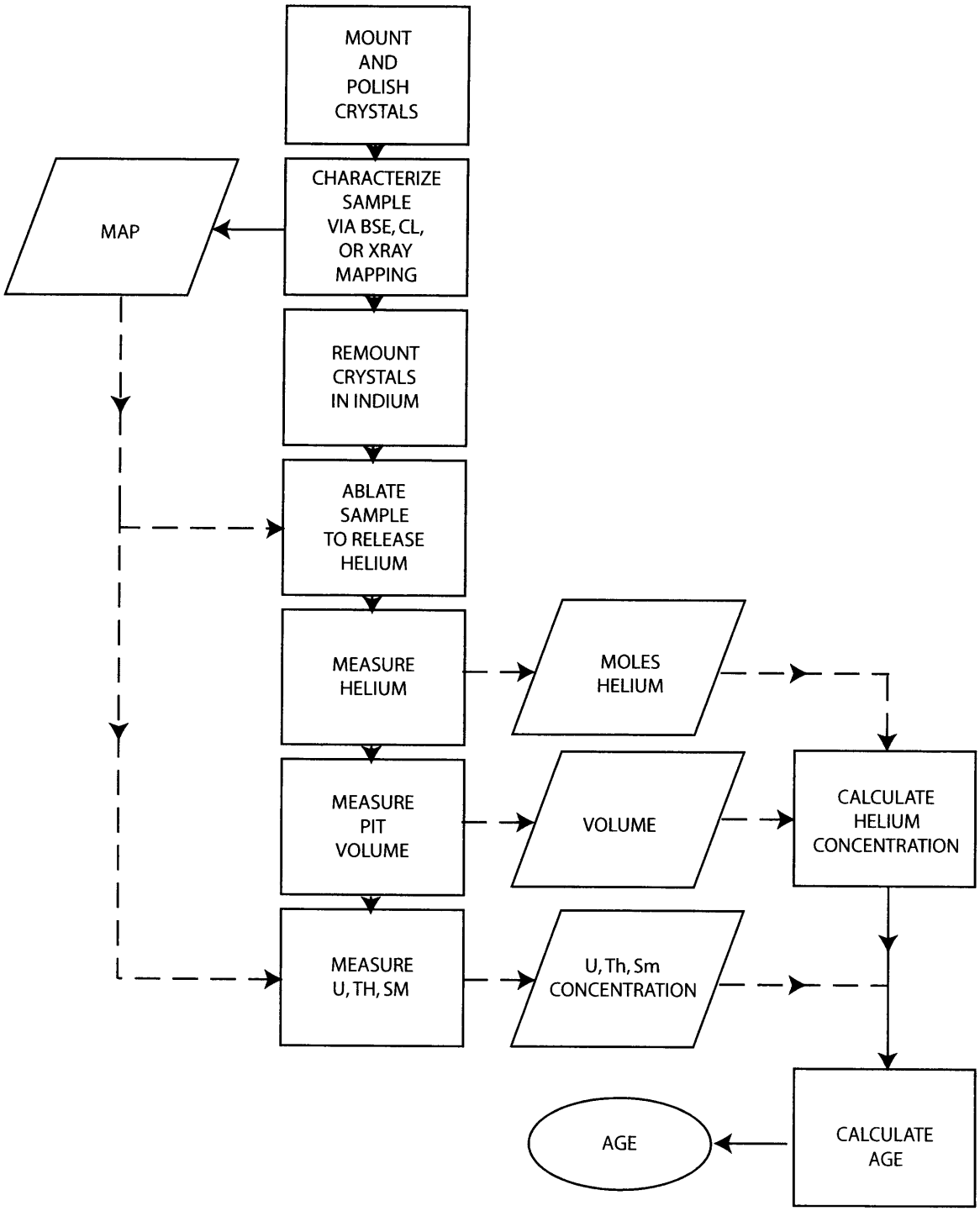
MOUNT AND POLISH CRYSTALS
CHARACTERIZE SAMPLE VIA BSE, CL, OR XRAY MAPPING
MAP
REMOUNT CRYSTALS IN INDIUM
ABLATE SAMPLE TO RELEASE HELIUM
MEASURE HELIUM
MOLES HELIUM
MEASURE PIT VOLUME
VOLUME
CALCULATE HELIUM CONCENTRATION
MEASURE U, TH, SM
U, Th, Sm CONCENTRATION
CALCULATE AGE
AGE

Figure 1

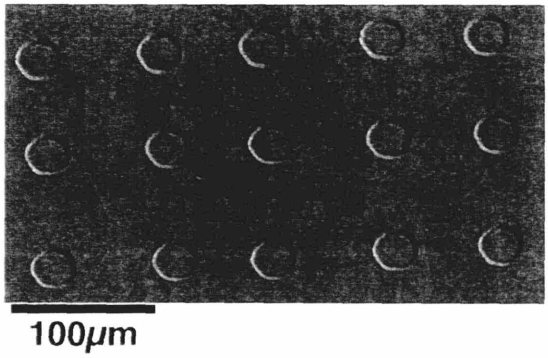

Figure 2

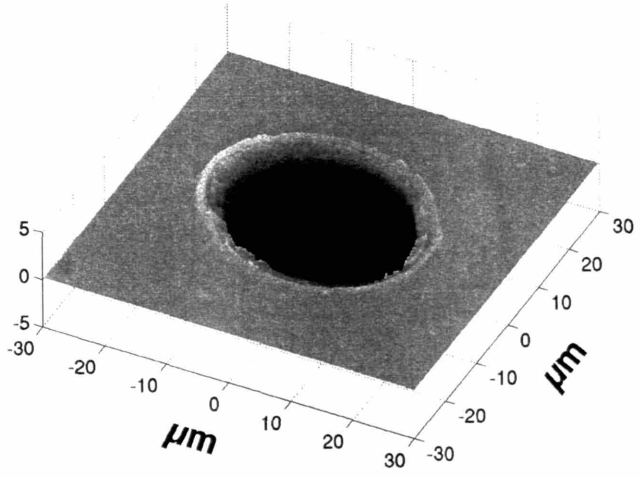

Figure 3

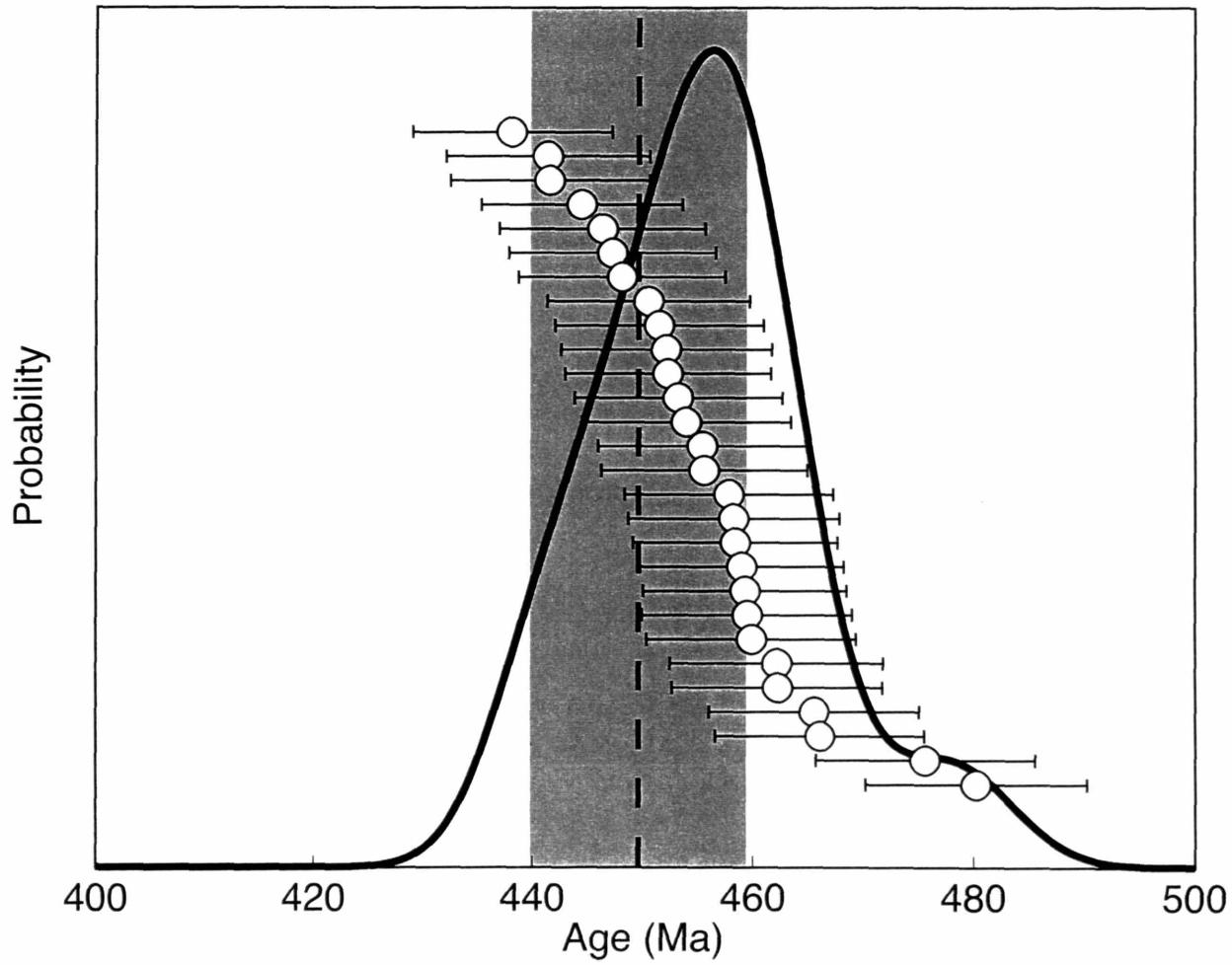

Figure 4

Sample	MOM3C	MOM3A	MOM3B
ncc ^{4}He	130.10	143.80	155.15
^{4}He (2σ)	2.8	3.2	3.4
U (ng)	0.1443	0.1564	0.1709
U (2σ)	0.0054	0.0060	0.0065
Th (ng)	9.33	10.34	11.13
Th (2σ)	0.30	0.33	0.39
Th/U	66.3	67.8	66.8
Sm (ng)	4.33	4.92	5.42
Sm (2σ)	0.13	0.15	0.16
Age (Ma)	**449.7**	**449.2**	**449.8**
Age (2σ)	**16.9**	**16.9**	**18.1**
Percent (2σ)	**3.8%**	**3.8%**	**4.0%**

Table 1
Conventional (U-Th)/He data

Spot #	^{4}He (moles)	^{4}He (2σ)	volume (μm^3)	volume (2σ)	U (ppm)	U (2σ)	Th (ppm)	Th (2σ)	Sm (ppm)	Sm (2σ)	Age (Ma)	Age (2σ)
MOM1 - 1	3.300E-13	1.9E-15	1176	24	1516	11	83243	130	30253	370	466.1	9.5
MOM1 - 2	1.840E-13	1.1E-15	667	13	1516	11	83243	130	30253	370	458.3	9.6
MOM1 - 3	2.625E-13	1.6E-15	978	20	1516	11	83243	130	30253	370	446.3	9.3
MOM1 - 4	2.650E-13	1.6E-15	959	19	1516	11	83243	130	30253	370	459.0	9.3
MOM1 - 5	2.690E-13	1.6E-15	998	20	1516	11	83243	130	30253	370	448.1	9.3
MOM1 - 6	2.675E-13	1.6E-15	983	20	1516	11	83243	130	30253	370	452.1	9.5
MOM1 - 7	2.640E-13	1.6E-15	994	20	1516	11	83243	130	30253	370	441.5	9.0
MOM1 - 8	2.680E-13	1.6E-15	989	20	1516	11	83243	130	30253	370	450.5	9.2
MOM1 - 9	2.800E-13	1.6E-15	1021	20	1516	11	83243	130	30253	370	455.6	9.3
MOM1 - 10	2.640E-13	1.5E-15	972	19	1516	11	83243	130	30253	370	451.5	9.5
MOM1 - 11	2.630E-13	1.6E-15	978	20	1516	11	83243	130	30253	370	447.2	9.4
MOM1 - 12	2.620E-13	1.5E-15	959	19	1516	11	83243	130	30253	370	453.9	9.5
MOM1 - 13	2.800E-13	1.7E-15	1055	21	1516	11	83243	130	30253	370	441.4	9.3
MOM1 - 14	2.660E-13	1.6E-15	956	19	1516	11	83243	130	30253	370	462.2	9.6
MOM1 - 15	2.630E-13	1.5E-15	951	19	1516	11	83243	130	30253	370	459.5	9.6
MOM1 - 16	2.600E-13	1.6E-15	939	19	1516	11	83243	130	30253	370	459.9	9.5
MOM1 - 17	2.600E-13	1.5E-15	955	19	1516	11	83243	130	30253	370	452.3	9.3
MOM1 - 18	2.630E-13	1.5E-15	964	19	1516	11	83243	130	30253	370	453.2	9.4
									MOM1 Weighted Mean		**453.3**	
										2σ	**13.7**	**3.0%**
										2SE	**3.4**	**0.8%**
MOM3 - 1	1.870E-13	1.1E-15	866	17	1344	14	63867	77	27844	1760	462.2	9.7
MOM3 - 2	1.873E-13	1.1E-15	834	17	1344	14	63867	77	27844	1760	480.2	10.0
MOM3 - 3	1.901E-13	1.1E-15	894	18	1344	14	63867	77	27844	1760	455.4	9.5
MOM3 - 4	1.871E-13	1.1E-15	860	17	1344	14	63867	77	27844	1760	465.6	9.6
MOM3 - 5	1.872E-13	1.1E-15	842	17	1344	14	63867	77	27844	1760	475.7	9.9
MOM3 - 6	1.869E-13	1.1E-15	914	18	1344	14	63867	77	27844	1760	438.1	9.1
MOM3 - 7	1.883E-13	1.1E-15	879	18	1344	14	63867	77	27844	1760	458.4	9.3
MOM3 - 8	1.891E-13	1.1E-15	911	18	1344	14	63867	77	27844	1760	444.4	9.1
MOM3 - 9	1.863E-13	1.1E-15	868	17	1344	14	63867	77	27844	1760	459.3	9.3
MOM3 - 10	1.887E-13	1.1E-15	883	18	1344	14	63867	77	27844	1760	457.8	9.5
									MOM3 Weighted Mean		**459.3**	
										2σ	**25.3**	**5.5%**
										2SE	**9.1**	**2.0%**
									MOM1 and MOM3 Weighted Mean		**453.3**	
										2σ	**19.2**	**4.2%**
										2SE	**3.7**	**0.8%**

TABLE 2
Laser Microprobe (U-Th)/He data

CHAPTER 4

Rapid cooling of a Pleistocene granite as revealed by laser microprobe (U-Th)/He thermochronology

Boyce, J.W., Hodges, K.V., King, D., Crowley, J.L., Jercinovic, M, Chatterjee, N., Bowring, S.A., and Searle, M.

To be submitted to:

Science

The newly developed excimer laser microprobe for (U-Th)/He geochronology permits, for the first time, the direct observation of the distribution of ^{4}He in individual crystals of accessory minerals. Such data may be used to map intracrystalline age domains and to understand better the process of thermally activated diffusive loss of ^{4}He during postcrystallization cooling. Applying the technique to monazite crystals from a 1.4-1.2 million year-old granite from the Nanga Parbat massif in the Pakistan Himalaya, we obtained ca. 750 ka (U-Th)/He cooling ages. We observed no evidence for the development of substantial diffusive-loss ^{4}He zoning over 90% of the interior of the monazite crystals during post-crystallization cooling of the granite. Numerical models of diffusive loss of ^{4}He from these crystals suggest that cooling at a minimum rate of ca. 325-375°C/my would be necessary to produce the observed lack of zoning. Such rapid cooling is most easily explained by rapid (>4.1-5.4 km/my) exhumation related to coupled tectonic extrusion and erosion.

The Nanga Parbat-Haramosh region of Pakistan includes dramatic exposures of granitic and high-grade metamorphic rocks that record the development of very high geothermal gradients during the latest stages of Himalayan orogenesis (Zeitler et al. 2001; Koons et al. 2002). Structural, geomorphic, geochemical, and geophysical data suggest that rock uplift and exhumation rates of the Nanga Parbat massif over the past few million years may have been among the highest on Earth, resulting in local relief in excess of 7000m, so better constraints on the maximum rates of exhumation at Nanga Parbat are of broad significance to our

understanding of mountain building processes in general. We describe here a novel approach to obtaining such constraints through the use of laser microprobe (U-Th)/He thermochronometry.

The (U-Th)/He geochronometer relies on the production of ^{4}He from naturally occurring ^{235}U, ^{238}U, ^{232}Th, and ^{147}Sm through alpha decay (e.g., Reiners 2002). Radiogenic ^{4}He diffuses rapidly in minerals at relatively low temperatures compared to the daughter products of chronometers such as U-Pb, Lu-Hf, and Sm-Nd, which typically record the time elapsed since crystallization. Thus, (U-Th)/He dates are usually interpreted as cooling ages, with each mineral assigned a bulk closure temperature based on the cooling rate, the size of the grain (or its effective diffusion dimension), and the temperature-dependent diffusivity of ^{4}He in the mineral (Hodges 2003). Post-crystallization cooling also should produce a ^{4}He concentration gradient in the grain, with a predicted topology that is related to the specific thermal history of the sample (Dodson 1986). Exploiting such gradients for tectonic studies requires the development of effective methods to resolve and quantify intracrystalline ^{4}He. Some progress toward this goal has been made by bombarding natural samples with medium- to high-energy protons to produce ^{3}He through spallation, and by then comparing the bulk diffusive loss patterns of synthetic ^{3}He and natural ^{4}He during step-heating experiments on the irradiated samples (Shuster and Farley 2003). However, the direct resolution of intracrystalline ^{4}He patterns was not possible until the recent development of the laser microprobe method of (U-Th)/He geochronometry {Boyce, submitted #218}.

The laser microprobe protocol involves using a focused ArF excimer laser to ablate pits in the polished surface of a grain under ultrahigh vacuum. The abundance of ^{4}He in the ablated material is determined through isotope dilution using a quadrupole mass spectrometer, and the concentration of ^{4}He in the sample is determined from that abundance by precise measurement of

the ablated pit with a white-light interferometric or laser confocal microscope. Relevant U, Th, and Sm isotopic concentrations are derived from elemental abundances as determined by electron microprobe or inductively coupled, plasma-source, mass spectrometric analysis of the material within or surrounding the ablation pit, and a (U-Th)/He date then can be calculated. For minerals high in U and Th, the effective spatial resolution of the technique is a few tens of microns or less. In addition to providing the means to examine intracrystalline ^{4}He gradients, the technique also eliminates the need to correct (U-Th)/He dates for the affects of alpha-particle ejection (Farley et al. 1996). Such corrections are necessary for conventional (U-Th)/He dating because the kinetic energy released during the nuclear reactions that produce ^{4}He are sufficient to propel these alpha particles out of the rim region of a crystal. By not targeting rim regions during laser microprobe analysis and obviating such corrections, it is possible to avoid major and often underestimated source of uncertainty in conventional (U-Th)/He chronometry (Hourigan et al. 2005).

In order to shed additional light on the evolution of the Nanga Parbat massif, we applied this method to two monazite crystals from a biotite + cordierite + tourmaline leucogranite that transects foliation in the host gneisses above Fairy Meadows Base Camp, north of the summit of Nanga Parbat at an elevation of approximately 3500m. Isotope-dilution, thermal ionization mass spectrometry U-Pb data for accessory minerals from this sample suggest crystallization ages of 1.2-1.4 Ma (Crowley et al. 2005). Backscattered electron images of both crystals (Figure 1) display evidence for chemical zoning that generally corresponds to variations in U and Th concentration (A description of the analytical methods is available as supporting material on Science Online) . In each case, core and rim zones relatively depleted in U+Th (Th = 39,200 - 49,400 ppm; U = 5,700 - 8,000 ppm) are separated by an intervening zone of high U+Th (Th =

55,000 - 58,000; U = 8,100 - 8,200). Targeting regions of the core and intermediate zones with relatively uniform compositions, we were able to determine (U-Th)/He dates for 14 ablation pits in Crystal 1 and 7 pits in Crystal 2. Each pit had a diameter of ~30 μm and a depth of ~12-14 μm. In all cases, the pits were far enough from the rims to avoid regions of extra-crystalline alpha ejection, but some pits were sufficiently close to the intracrystalline zone boundaries as to necessitate minor corrections for zone-to-zone alpha exchange. (See supplemental material for analytical details.)

For such young samples, an additional correction must be made to account for ^{4}He production by "excess" ^{230}Th incorporated into the monazite structure during crystallization (Schärer 1984). Although similar corrections for excess ^{230}Th-derived ^{206}Pb can have a significant effect on calculated U-Pb dates for very young monazites, the corrections for (U-Th)/He dates are small by comparison because ^{4}He diffuses readily out of the system until it cools well below the crystallization temperature and much ^{230}Th – which has a half-life of only ~ 75 ka – decays away in the meantime. For the Nanga Parbat monazites studied here, (U-Th)/He age corrections based on the Th/U ratios for melts calculated to be in equilibrium with monazites from this sample (Crowley et al. 2005) were less than 5,000 years.

All 21 pits analyzed in the two monazite crystals yielded similar ages (Figure 2, Table 1). For Crystal 1, fourteen analyses have an error-weighted mean age of 746 ka. The mean squared weighted deviation (MSWD) for this average is 3.4, a value larger than that which might be explained simply by random experimental error if our estimates for the various error input parameters are correct (Wendt and Carl 1991). In the case of laser microprobe (U-Th)/He geochronology, the least well-known of these parameters is the estimated error in the volume measurement for each pit, which is based on only a small number of replicate analyses and may

be underestimated. As a consequence, we multiplied the nominal uncertainty in the mean by the square-root of the MSWD (Ludwig 2003) to arrive at a conservative estimate of 26,000 years (2SE) for the uncertainty in the error-weighted mean age of Crystal 1. By the same statistical approach, we calculated a mean age of 753 ± 33 ka (MSWD = 2.5) for the seven Crystal 2 analyses. Since the means for the two crystals are statistically indistinguishable, we combined all 21 analyses to arrive at a mean age for both crystals of 748 ± 19 ka.

In conventional (U-Th)/He thermochronology, entire crystals are dated in bulk and it is standard practice is to assign a bulk closure temperature to the determined age (Hodges 2003). For the Nanga Parbat monazites, we instead focus on estimating the closure temperature for the core of the grains using the formalism of Dodson (1986). Such calculations – which presume that the effective diffusion dimension for ^{4}He in monazite is the physical grain size – rely on a knowledge of ^{4}He diffusion kinetics and an estimation of cooling rate. All studies of ^{4}He diffusion in accessory minerals support the presumption that physical grain size is the effective diffusion dimension (Farley and Stockli 2002; Reiners in press). Only two studies of ^{4}He diffusivity in monazite have been done thus far (Stockli et al. 2005; Boyce et al. in press); these preliminary results suggest a strong, but incompletely understood, dependence of diffusion rate on composition. If we assume an intrinsic ^{4}He diffusivity on the high end of the existing experimental results and any reasonable range of cooling rates, the minimum core (U-Th)/He closure temperatures for the Nanga Parbat monazites is likely to be at least 230°C. Accepting this value suggests a minimum average cooling rate for the leucogranite sample since monazite closure of >300°C/my.

A somewhat more sophisticated approach to estimating a cooling rate involves diffusion modeling of the actual closure profile for Crystal 1, the grain for which we have the most data

(Figure 3). The most significant characteristic of this profile is the lack of a resolvable diffusion gradient across roughly 80% of the interior of the crystal, which implies very rapid cooling. Simple modeling of the cooling history as a linear function with time suggests that the data are most compatible with a cooling rate of 325-375°C/my. Again, this estimate is based on the highest diffusivity values from monazite experiments done thus far {Boyce, in press #4027}; the use of diffusivities on the low end of the spectrum would result in cooling rate estimates of 500°C/my or more. In the future, a better understanding of the compositional effects on ^{4}He diffusivity in monazite will permit a more refined cooling rate estimate from these data.

Despite such uncertainties, our results have significant implications regarding the exhumation history of the Nanga Parbat massif. Several lines of evidence have been used to argue for an elevated geothermal gradient (~70-80°C/km) beneath Nanga Parbat that has persisted for several million years (Zeitler et al. 2001; Chamberlain et al. 2002). Accepting this estimate, our data suggest a minimum exhumation rate of 4.1-5.4 km/my averaged over the past ~750,000 years, but the actual rate might easily be a factor of two or more higher. Previous thermochronologic and petrologic work on rocks of the Nanga Parbat metamorphic core has suggested that comparably high exhumation rates occurred over the Pliocene-Early Pleistocene interval, while cosmogenic nuclide dating of strath terraces along the Indus River as it passes through the massif imply comparable rates of river incision since the latest Pleistocene (Winslow et al. 1994; Burbank et al. 1996). The monazite results presented here – which address the rate of bedrock exhumation since the Middle Pleistocene – provide an important link between the timescales represented by previous datasets, suggesting that extremely high river incision and bedrock exhumation rates have been roughly equal at Nanga Parbat for the past few million years. This implies that rock exhumation and erosion have been balanced over the last 750 ka at

Nanga Parbat. The most likely tectonic scenario to explain this balance appears to involve a coupling of mid- to lower-crustal extrusion and focused erosion through river incision (Zeitler et al. 2001; Koons et al. 2002).

Beyond the tectonic significance of the data, this study – which represents the first application of laser microprobe technology in (U-Th)/He thermochronology – confirms the feasibility of directly imaging intracrystalline ^{4}He variations in accessory minerals. For very rapidly cooled minerals with limited ^{4}He diffusive-loss zoning, the laser microprobe offers an opportunity to produce numerous replicate analyses in a short time, increasing the effective analytical precision to levels comparable to the most precise conventional (U-Th)/He results, even for samples less than one million years old. Of special importance to future applications is the capability of using the excimer laser for depth-profiling with a nominal depth resolution of ~0.1 μm. As Figure 3 suggests, most of the temperature-time information preserved in a ^{4}He diffusion profile for more slowly cooled samples is within the outermost 10-15% of the grain, where corrections for alpha-ejection loss are most important. By combining high-resolution depth profiles of ^{4}He concentration with appropriate ejection-production models (Ketcham 2005), it should be possible to develop extremely detailed reconstructions of the thermal evolution of appropriate samples for tectonic and landscape evolution studies.

Figure Captions

Figure 1. BSE intensity maps of the two crystals, showing locations of the ablation pits. Inset: BSE image of ablation pit.

Figure 2. Probability distribution function of Nanga Parbat Laser microprobe (U-Th)/He ages, with individual ages and 2σ uncertainties.

Figure 3. Laser microprobe (U-Th)/He age versus normalized radial position for Crystal 1. Boxes show spot position and ± 2σ uncertainties for each analysis. Shaded horizontal region with white line depicts the weighted mean age and 2σ of the mean of the population of ages. Thin dashed black lines indicate model cooling age variations for cooling rates ranging from 300 - 400 K/my. Dark shaded vertical band indicates region within ejection distance (~17μm) of the edge of the crystal.

References

Boyce, J. W., K. V. Hodges, et al. (in press). "He diffusion in monazite: Implications for (U-Th)/He thermochronometry." G-Cubed.

Burbank, D. W., J. Leland, et al. (1996). "Bedrock incision, rock uplift and threshold hillslopes in the northwestern Himalayas." Nature **379**: 505-510.

Chamberlain, C. P., P. O. Koons, et al. (2002). "Overview of hydrothermal activity associated with active orogenesis and metamorphism: Nanga Parbat, Pakistan himalaya." American Journal of Science **302**: 726-748.

Crowley, J. L., S. A. Bowring, et al. (2005). "U-Th-Pb systematics of monazite, xenotime, and zircon from Pleistocene leucogranites at Nanga Parbat (Pakistan Himalaya)." Geochimica et Cosmochimica Acta **69**: A8.

Dodson, M. H. (1986). "Closure profiles in cooling systems." Materials Science Forum **7**: 145-154.

Farley, K. A. and D. Stockli (2002). "(U-Th)/He dating of phosphates: apatite, monazite, and xenotime." Reviews in Mineralogy and Geochemistry **48**: 559-577.

Farley, K. A., R. A. Wolf, et al. (1996). "The effects of long alpha-stopping distances on (U-Th)/He ages." Geochimica et Cosmochimica Acta **60**(21): 4223-4229.

Hodges, K. V. (2003). Geochronology and Thermochronology in Orogenic Systems. The Crust. R. L. Rudnick. Amsterdam, Elsevier Science. **3:** 263-292.

Hourigan, J. K., P. W. Reiners, et al. (2005). "U-Th zonation-dependent alpha-ejection in (U-Th)/He chronometry." Geochimica Cosmochimica Acta **69**(13): 3349-3365.

Ketcham, R. A. (2005). Forward and inverse modeling of low-temperature thermochronometry data. Reviews in Mineralogy and Geochemistry: Low-temperature thermochrology: Techniques, Interpretations, Applications. P. W. Reiners and T. A. Ehlers, Mineralogical Society of America. **58:** 275-314.

Koons, P. O., P. K. Zeitler, et al. (2002). "Mechanical links between erosion and metamorphism in Nanga Parbat, Pakistan Himalaya." American Journal of Science **302**(9): 749-773.

Ludwig, K. R. (2003). "Mathematical-statistical treatment of data and errors for 230Th/U geochronology." Reviews in Mineralogy and Geochemistry **52**: 631-656.

Reiners, P. W. (2002). "(U-Th)/He chronometry experiences a renaissance." EOS, Transactions of the American Geophysical Union **83**(3): 21-27.

Reiners, P. W. (in press). Zircon (U-Th)/He thermochronometry. Thermochronology: Reviews in Mineralogy and Geochemistry. P. W. Reiners and T. A. Ehlers. Washington, DC, Mineralogical Society of America. **59**.

Schärer, U. (1984). "The effect of initial ^{230}Th disequilibrium on young U-Pb ages: the Makalu case, Himalaya." Earth and Planetary Science Letters **67**: 191-204.

Shuster, D. L. and K. A. Farley (2003). "4He/3He thermochronometry." Earth and Planetary Science Letters **217**: 1-17.

Stockli, D., K. A. Farley, et al. (2005). "He diffusion and (U-Th)/He thermochronometry of monazite and rutile." Geochimica et Cosmochimica Acta **69**: A8.

Wendt, I. and C. Carl (1991). "The statistical distribution of the mean squared weighted deviation." Chemical Geology **86**: 275-285.

Winslow, D. M., P. K. Zeitler, et al. (1994). "Direct evidence for a steep geotherm under conditions of rapid denduation, Western Himalaya, Pakistan." Geology **22**: 1075-1078.

Zeitler, P. K., P. O. Koons, et al. (2001). "Crustal reworking at Nanga Parbat, Pakistan; metamorphic consequences of thermal-mechanical coupling facilitated by erosion." Tectonics **20**(5): 712-728.

Zeitler, P. K., P. O. Koons, et al. (2001). "Crustal reworking at Nanga Parbat, Pakistan: Metamorphic consequences of thermal-mechanical coupling facilitated by erosion." Tectonics **20**(5): 712-728.

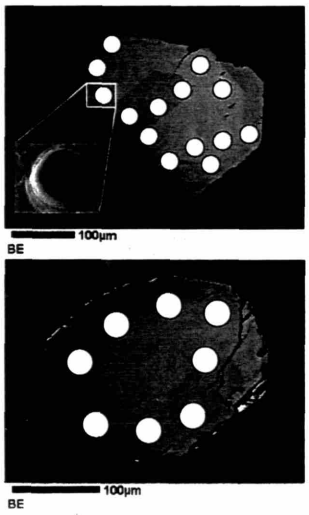

Figure 1

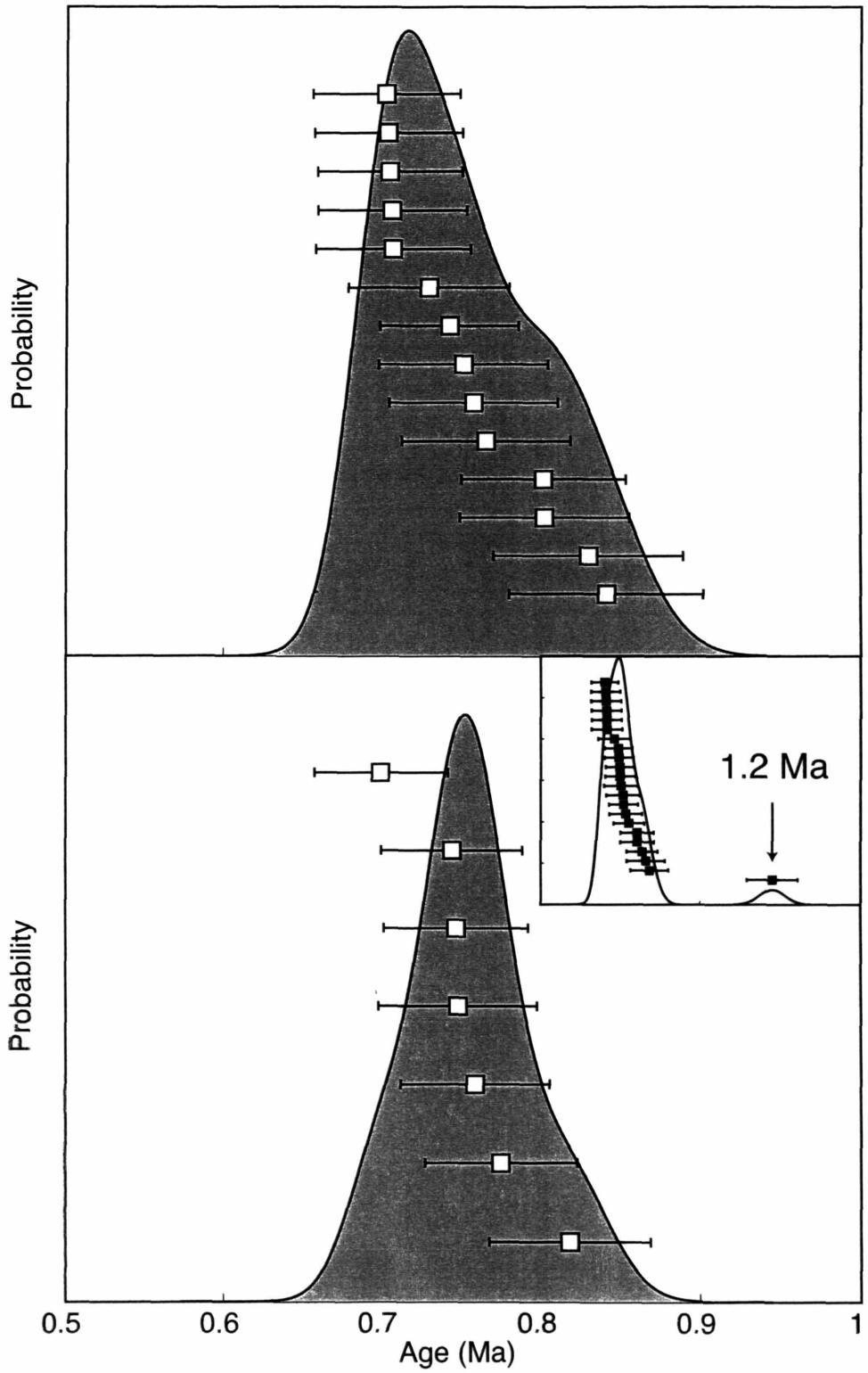

Figure 2

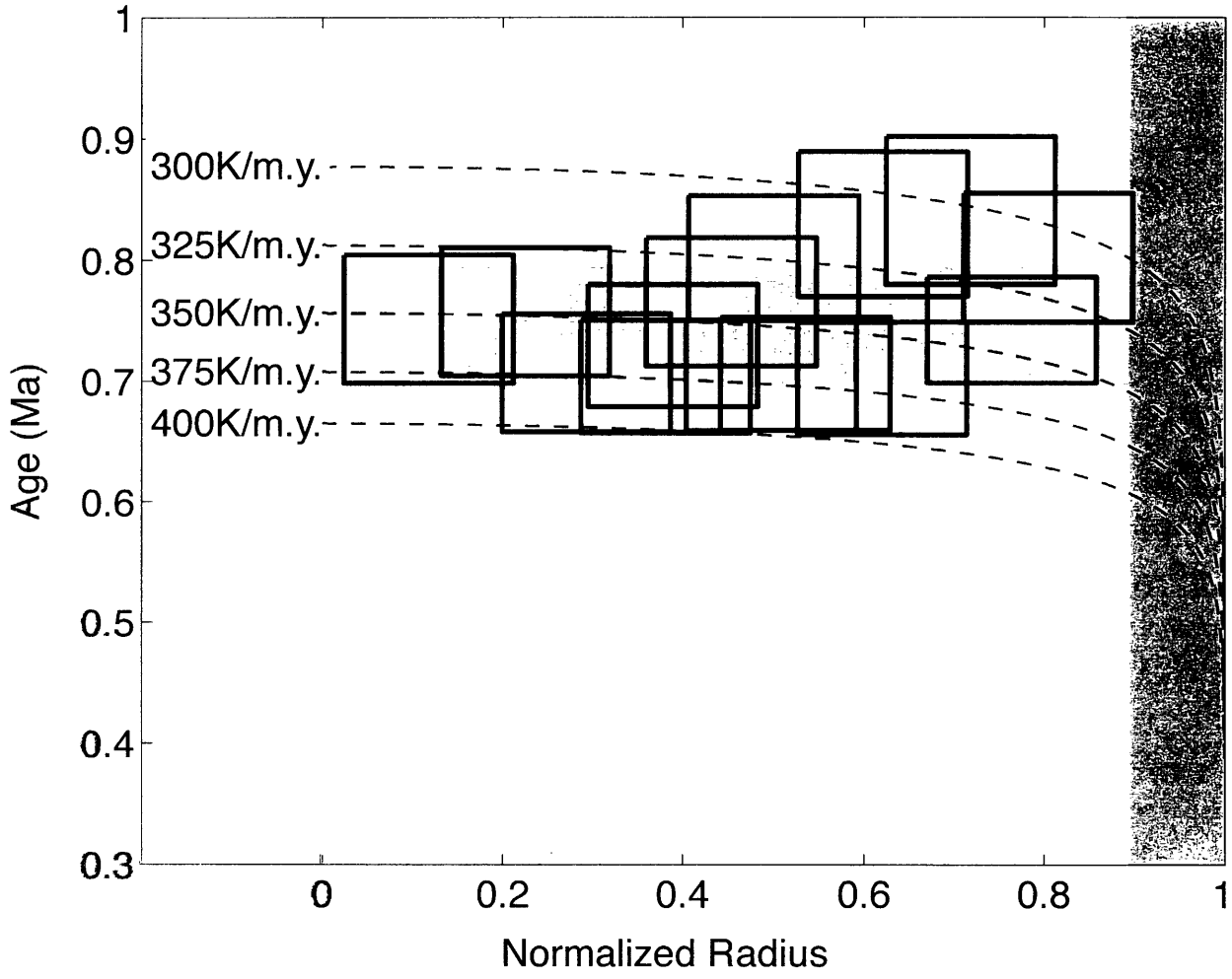
1
0.9
0.8
0.7
0.6
0.5
0.4
0.3
Age (Ma)
300K/m.y.
325K/m.y.
350K/m.y.
375K/m.y.
400K/m.y.
0
0.2
0.4
0.6
0.8
1
Normalized Radius

Figure 3

Supporting Online Material for

Rapid cooling of a Pleistocene granite as revealed by laser microprobe (U-Th)/He thermochronology

*Boyce, J.W., Hodges, K.V., King, D., Crowley, J.L., Jercinovic, M., Chattergee, N., Bowring, S.A., and Searle, M.

*To whom correspondence should be addressed. E-mail: jwboyce@mit.edu

This PDF file contains:

Analytical Protocol

Sample Preparation

Two ~200μm diameter monazite crystals were mounted in epoxy and polished by hand to 0.05μm grit. Crystals were subsequently imaged using backscattered electron techniques (Figure 1), then re-polished to remove the carbon coating required for electron microprobe analysis. This second polishing also reduces the possibility that the material to be dated has not experienced thermally induced helium loss due to the energy imparted by the electron microprobe. Samples were then transferred from epoxy grain mounts to indium mounts. Unlike epoxy and other organic resins, indium is a sufficiently vacuum-friendly media for UHV noble gas analyses. However, indium is not strong enough to hold grains during polishing, necessitating the transfer.

Helium Concentrations

After remounting the crystals in indium, the samples were ablated by a Lambda Physik excimer laser, operating at a nominal wavelength of 193nm (see Figure 1 for spot locations). Ablated pits are ~30μm in diameter, and 12-14μm deep (Figure 1 inset). Radiogenic helium released by ablation was spiked with a known amount of ^{3}He, purified by active metal getters, and measured by isotope dilution on a quadrupole mass spectrometer following the procedures outlined in Boyce et al. (submitted). Ablated volumes were measured by laser confocal microscopy, using a Carl Zeiss Instruments LSM 5 Pascal, allowing the He concentration to be determined. Nominal resolution of this instrument is ~25nm in the vertical direction, and horizontal resolution of < 0.25μm.

U, Th, and Sm Concentrations

U, Th, and Sm concentrations were measured by electron microprobe at The University of Massachusetts, following procedures outlined in Jercinovic and Williams (2005). Care was taken to correct U concentrations for overlap of the Th family of X-ray lines (Th M-γ, Th M3-N4, the associated high energy M3-N4 satellite, and Th M5-P3) on U M-β (our analytical line for uranium).

Calculating effective parent element concentrations

The relevant parent element concentrations for a given spot on the map are not the U, Th, and Sm concentrations at that spot, but are rather a function of the parent element distribution in the region surrounding the spot. This is because the alpha particles in a given spot were actually generated roughly one ejection distance away and ejected (randomly) to that spot. In order to properly account for alpha-recoil from a three-dimensional distribution of parent elements, we must create a model to calculate the "effective" parent element concentrations for each spot on the map of the crystal.

The first step is to create a simplified map of the parent element concentrations in each crystal using the discrete spot analyses of U, Th, and Sm concentrations and the backscattered electron maps from the electron microprobe (Figure S1). Each crystal is defined to have three homogeneous zones, with concentrations defined by electron microprobe analysis. The map of the crystal is surrounded by a zero boundary condition, as the concentrations of U, Th, and Sm outside the crystal were considerably (~1000x) less than the concentrations in the crystal. This assumption is likely true for the major mineral phases (feldspars, quartz, etc.) found in the leucogranite from which these monazites were derived, and is the same assumption made for conventional alpha-ejection corrections (Farley et al. 1996).

Following the model of Boyce and Hodges (2005), we calculate the "effective" concentration of each node in the elemental map by averaging all the parent element concentrations located one ejection distance away from the node of interest. Because this is a three-dimensional problem, we assume that there is no variation out of the plane of the map, a simplification necessary because the true compositions are not available as a function of depth. This assumption is less likely to effect the calculations for shallow pits in crystals with relatively long-wavelength zoning, where changes in composition over the depth of a pit are likely to be minimal. In order to account for out-of-plane effects, we calculate the position in the plane corresponding to the vertical projection of the points on the surface of an imaginary sphere centered on the node of interest. By sampling the sphere at ~10° increments in azimuth and inclination, and finding the nearest Cartesian grid points, we can map 3600 points lying near the surface of the sphere on to the map plane. The elemental concentrations for those points are then averaged, the value stored, and the process repeated for all points in the map.

The results of the model are shown in Figure S2 for each of the parent elements. As one would expect, regions near the edge of a crystal have a low effective parent composition, reflecting the fact that there is no contribution to nodes near the edge from any neighboring nodes outside the crystal. Regions of the crystal near zone boundaries also show effects of alpha-ejection on effective parent element concentrations. Any node near a boundary will receive ^{4}He from both sides of the zone, resulting in an effective parent element concentration that reflects the partial contribution from each zone.

Effective concentrations of U, Th, and Sm for a given analysis are calculated by averaging all the nodes within each ablation pit. Uncertainties are propagated as averages, using the geometric mean of the uncertainties of the individual zones, except in cases where spots were

completely contained within one zone, in which case the uncertainty on the concentrations from only that zone was propagated into the age calculation.

Age Calculations and Error Propagation

Calculating (U-Th)/He ages

Calculation of (U-Th)/He ages is accomplished by iterative application of the ^{4}He production equation (commonly referred to as the "(U-Th)/He age equation") extended to include secular disequilibrium in the intermediate daughter products of ^{238}U, following a conceptualization similar to that of Farley et al (2002). Secular disequilibrium is defined by estimated isotope ratios at the time of crystallization, or by measured isotope ratios at present. The amount of time in between crystallization and the start of the (U-Th)/He clock (the "cooling interval"), decreases the effect of disequilibrium and is also taken into account. For the monazites dated in this study, any excess ^{230}Th initially present has decayed over the ~16-20 half-lives since crystallization at 1.2-1.4 Ma, and cannot be measured. Therefore we use estimated initial ^{230}Th excesses based on Th/U ratios determined for melts in equilibrium with monazites from the host rock, which for these rocks are 0.41 - 1.11.

Ages were calculated in a two-step iterative process: First, an age is calculated with an estimated cooling interval – or a zero value if no estimate is possible. This age is then subtracted from the independently determined crystallization age in order to determine a new improved estimate of the cooling interval. The cooling interval is then plugged into the modified age equation, reducing the effect of ^{230}Th excess on the (U-Th)/He age calculated, resulting in a more refined estimate of the cooling age. This process is repeated several times until the (U-Th)/He

age converges on the correct age for the given crystallization age and amount of initial excess ^{230}Th.

Propagation of Uncertainties

Measurement uncertainties are propagated into the final age by *Monte Carlo* modeling (Press et al. 1992). In brief, the procedure is as follows: For each variable in the (U-Th)/He age equation, a large ($N \geq 10^4$) array of numbers is generated, with each array a finite approximation of a normal distribution about the mean of that variable, with a sample population deviation equal to one standard deviation of the measurement. For each sample, the age calculation (as described above) is repeated ~ 0.5*N times, with each independent age determination sampling randomly from the arrays of variables. The population of ages determined from this random sampling is then used to define the standard deviation of each age. The process is numerically intensive, but because of optimization built into the algorithm, the calculation usually takes < 2 minutes for each (U-Th)/He age, even when the code is run on an Apple ibook 1GHz G4 laptop comuter.

Figures

Figure S1. Simplified U, Th, and Sm maps for recoil-based parent element modeling. Color scale is a function of concentration, chosen so that it mimics backscattered electron intensity: light (bright) grays are higher concentrations, while darker grays are relatively lower concentrations. Color scale is different for each element.

Figure S2. Alpha-recoil corrected maps of effective parent concentrations. Note that zone boundaries modeled as sharp step-functions in true U-Th-Sm concentrations are gradational in "effective concentration".

Tables

Table S1. U and Th measurements for each of the three zones observed in each crystal. Uncertainties reported as two standard deviations from the mean.

Table S2. Data used to calculate laser microprobe (U-Th)/He ages, along with those ages and uncertainties.

Boyce, J. W. and K. V. Hodges (2005). "U and Th zoning in Cerro de Mercado (Durango, Mexico) fluorapatite: Insights regarding the impact of recoil redistribution of radiogenic ^{4}He on (U–Th)/He thermochronology." Chemical Geology **219**: 261-274.

Boyce, J. W., K. V. Hodges, et al. (submitted). "Laser microprobe (U-Th)/He geochronology." Earth and Planetary Science Letters.

Farley, K. A., B. P. Kohn, et al. (2002). "The effects of secular disequilibrium on (U-Th)/He systematics and dating of Quaternary volcanic zircon and apatite." Earth and Planetary Science Letters **201**: 117-125.

Farley, K. A., R. A. Wolf, et al. (1996). "The effects of long alpha-stopping distances on (U-Th)/He ages." Geochimica et Cosmochimica Acta **60**(21): 4223-4229.

Jercinovic, M. J. and M. L. Williams (2005). "Analytical perils (and progress) in electron microprobe trace element analysis applied to geochronology: Background acquisition, interferences, and beam irradiation effects." American Mineralogist **90**: 526-546.

Press, W. H., S. A. Teukolsky, et al. (1992). Numerical Recipes in C: The Art of Scientific Computing. Cambridge, Cambridge University Press.

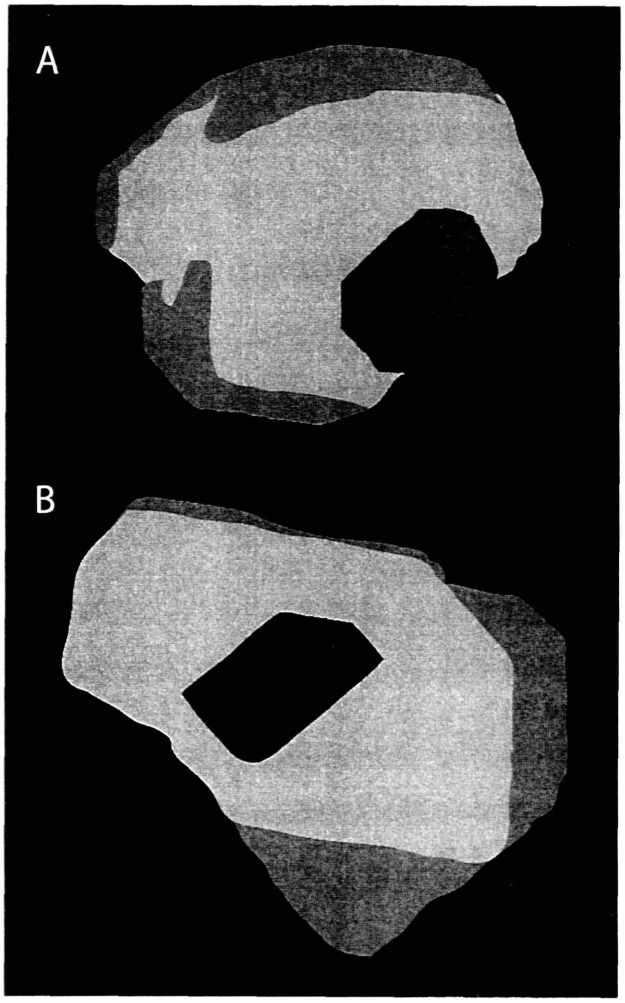

Figure S1

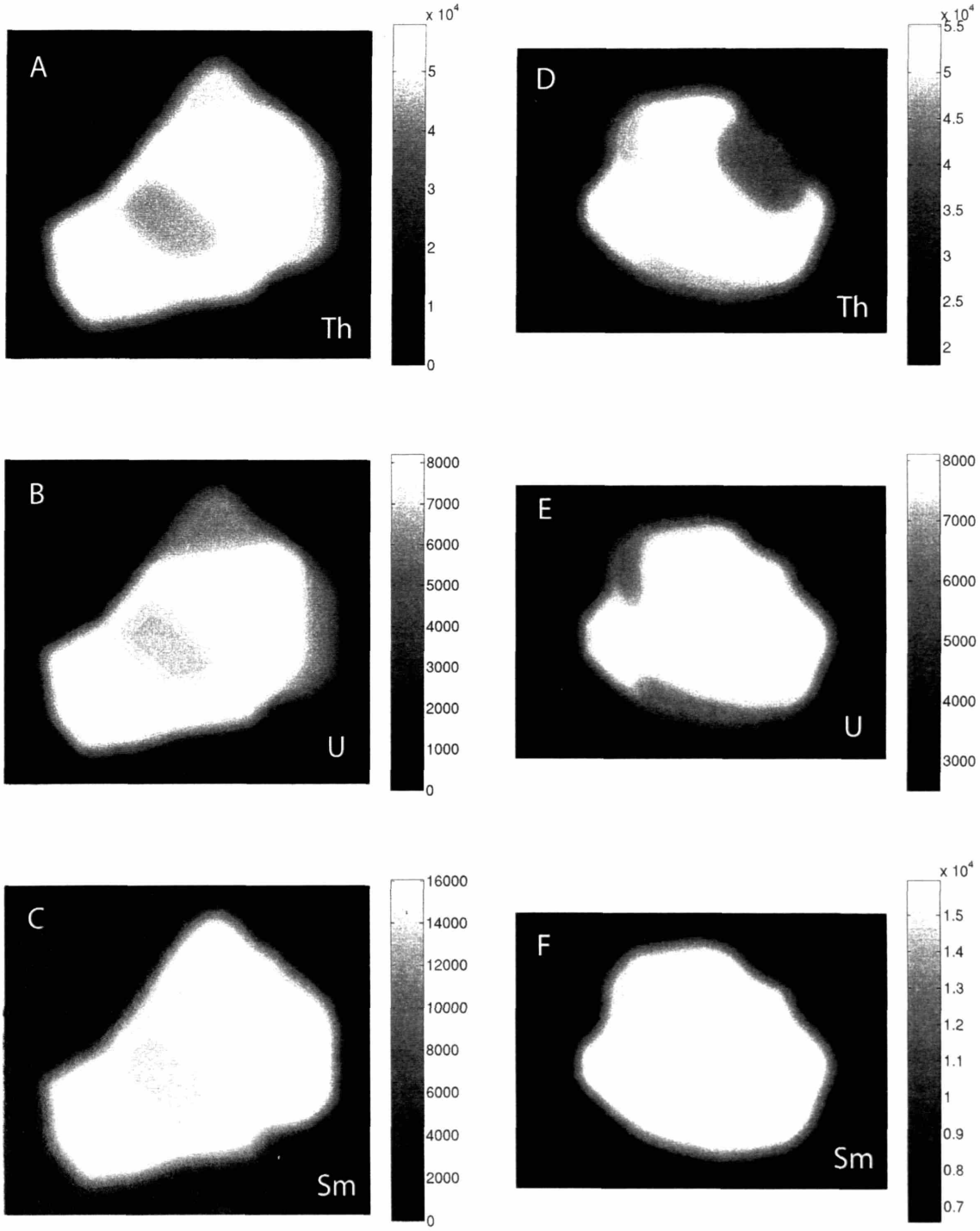
A
Th
x 10^4
5
4
3
2
1
0
D
Th
x 10^4
5.5
5
4.5
4
3.5
3
2.5
2
B
U
8000
7000
6000
5000
4000
3000
2000
1000
0
E
U
8000
7000
6000
5000
4000
3000
C
Sm
16000
14000
12000
10000
8000
6000
4000
2000
0
F
Sm
x 10^4
1.5
1.4
1.3
1.2
1.1
1
0.9
0.8
0.7

Figure S2

TABLE 1

U, Th, and Sm concentrations (ppm) as determined by EMPA

	Domain	U	U 2s	Th	Th 2s	Sm	Sm 2s
Crystal 1	core	7011	492	45719	1108	13584	1290
	middle	8209	540	57943	1294	14830	1282
	rim	6024	218	49376	576	16071	677
Crystal 2	core	7980	276	39176	504	15960	710
	middle	8101	257	55204	591	15968	607
	rim	5689	404	46835	1076	15169	1272

Table 2

Spot	He (mols x 10^{-15})	He (2σ)	volume (μm^3)	volume (2σ)	U (ppm)	U (2σ)	Th (ppm)	Th (2σ)	Sm (ppm)	Sm (2σ)	Age (ka)	Age (2σ)
1a	2.498	0.064	6002	296	6933	381	52984	899	15555	970	765.4	52
1b	2.452	0.093	5772	289	6513	381	49931	899	15159	970	829.7	61
1c	2.660	0.080	6228	311	8130	381	57529	899	14875	970	703.5	47
1d	2.604	0.087	6028	304	8208	381	57922	899	14831	970	706.0	47
1e	2.593	0.071	6195	304	6245	381	48911	899	15373	970	840.9	60
1f	2.473	0.120	5830	292	8092	381	56609	899	14710	970	706.8	48
1g	2.363	0.068	5908	299	7555	381	51059	899	14094	970	729.4	50
1h	2.173	0.063	5679	281	7116	381	46998	899	13694	970	751.2	53
1i	2.250	0.074	5604	285	7322	381	49270	899	13908	970	757.4	53
1j	2.864	0.076	5873	293	8154	381	57628	899	14861	970	801.4	53
1k	2.479	0.081	5801	294	8155	381	57316	899	14817	970	704.5	47
1l	2.559	0.069	5977	299	8194	381	57653	899	14814	970	702.0	45
1m	2.516	0.077	5536	277	8209	270	57943	647	14830	641	742.3	44
1n	2.480	0.062	5171	259	8022	381	56590	899	14808	970	801.9	53
2a	2.540	0.077	5787	289	8082	276	55084	664	15962	789	744.3	46
2b	2.497	0.080	5886	291	7480	276	52982	664	15762	789	758.9	46
2c	2.477	0.068	5630	282	7058	276	51543	664	15623	789	818.1	49
2d	2.653	0.064	6103	305	7941	276	54521	664	15915	789	746.8	44
2e	2.553	0.067	6128	306	8041	276	47359	664	15964	789	775.2	48
2f	3.657	0.098	6149	307	7965	276	39788	664	15921	789	1225.3	79
2g	2.636	0.079	6400	320	8071	276	54969	664	15958	789	699.6	42
2h	2.198	0.073	6005	307	6143	276	48070	664	15245	789	748.0	48

Mean age (crystal 1, N=14)	746	ka	
Two standard deviations	49	ka	6.5%
Two standard errors	26	ka	3.5%
Mean age (crystal 2, N=7)	753	ka	
Two standard deviations	36	ka	4.8%
Two standard errors	33	ka	4.4%
Mean age (both crystals, N=21)	748	ka	
Two standard deviations	44	ka	5.9%
Two standard errors	19	ka	2.5%

CHAPTER 5

Preliminary Investigations into the Feasibility of Laser Microprobe (U-Th)/He Geochronology of Zircon

Boyce, J.W., Hodges, K.V., Olszewski, W.J., Carpenter, B.D., and Hanchar, J. M.

Abstract

Successful application of the laser microprobe to (U-Th)/He for the mineral monazite suggests that other minerals such as zircon also might be amenable to the technique. This chapter describes the first attempt to determine laser microprobe (U-Th)/He dates on zircon crystals. Three suites of apparently rapidly cooled zircons with well-constrained U-Pb and $^{40}Ar/^{39}Ar$ ages from 200 Ma to over 2 Ga were chosen for this study. A fourth suite of volcanic zircons with a poorly constrained eruption age of < 1 Ma was also selected in order to test the ability of the method to date very young samples. Unlike monazite, which typically contains high concentrations of Sm and Th and moderately high concentrations of U, zircon can have relatively low abundances of all three ^{4}He parent elements and thus poses different analytical challenges. In particular, electron probe microanalysis – the method used for measuring parent element abundances for monazite laser microprobe (U-Th)/He studies – is not currently practical for zircon Sm, U, and Th measurements. For our preliminary studies, we turned instead to the method of laser ablation inductively coupled plasma mass spectrometry (LA-ICPMS). U and Th measurements were made in two different LA-ICPMS laboratories (Boston University and Memorial University Newfoundland), using two different analytical protocols. (Very low concentrations of Sm, combined with the small contribution of He from Sm, were thought to render Sm measurements unnecessary for this particular study). One of the LA-ICPMS datasets (BU) was further reduced using two different internal standards (Zr and Hf) to explore the effect of standardization on trace element concentrations. All ^{4}He measurements were conducted at the MIT Noble Gas Geochronology facility using an ArF excimer for gas extraction.

Although our efforts to extract and measure small quantities of radiogenic ^{4}He using the excimer laser microprobe were successful, our efforts to determine meaningful (U-Th)/He ages

for the unknowns were not. Using Zr-normalized, Boston University U and Th data, the calculated dates were significantly different than the predicted ages and replicate U and Th analyses typically yielded internally inconsistent results. Strong correlations between the dates and U and Th measurements for the majority of the samples suggest that the poor reproducibility within each suite is likely caused by the LA-ICPMS measurements. Hf normalization of the same raw datasets from the Boston University facility appeared to improve the accuracy of the calculated dates – presuming that our initial expectations regarding the (U-Th)/He age for each unknown were correct. However, this normalization technique led to large U and Th uncertainties that propagated into large apparent age uncertainties, and did very little too improve the unacceptably large dispersion in the (U-Th)/He dates obtained for each unknown. Re-analysis of selected zircons using different protocols and spot locations at Memorial University resulted in different average (U-Th)/He dates. While closer to the expected ages, these dates are still likely to be geologically meaningless, and the dispersion of (U-Th)/He dates obtained for each unknown was even greater than that obtained using the Boston University data. Our preliminary efforts suggest that developing better microanalytical protocols for quantitative U, Th, and Sm analysis of zircon is essential for successful laser microprobe (U-Th)/He dating of zircon.

Introduction

As outlined in previous chapters of this thesis, it is now possible to determine precise and accurate (U-Th)/He cooling ages for monazite using laser ablation methods. An obvious question is whether or not this technique is capable of yielding equally valuable dates for other materials rich in U and Th. The next logical choice of target mineral is zircon ($ZrSiO_4$), which has been the

subject of several (U-Th)/He chronometry studies (Farley et al. 2002; Tagami et al. 2003; Reiners et al. 2005). This mineral is a nearly ubiquitous accessory phase in crustal rocks, and contains sufficient U and Th to make dating small volumes of even very young material possible. Zircon has also been demonstrated to have U and Th zoning which can compromise (U-Th)/He age calculations (Tagami et al. 2003; Hourigan et al. 2005), making a microanalytical technique potentially advantageous.

In this paper we describe a preliminary attempt to apply laser microprobe (U-Th)/He geochronology to three suites of zircons with well-constrained by $^{40}Ar/^{39}Ar$ and U-Pb ages, and one suite of zircons from the South Biscuit Basin flow, Yellowstone caldera, U.S.A., with a poorly constrained eruption age. Although none of the rocks selected for this study have been previously dated by the (U-Th)/He technique, they are otherwise ideal for our purposes in that they are all thought to have cooled quickly after formation; three of the four suites are from extrusive volcanic rocks, while the fourth is from a bolide impact melt sheet. Therefore, the ages determined by U-Pb and $^{40}Ar/^{39}Ar$ methods can be used as predicted ages for (U-Th)/He determinations. The excimer laser extraction and ablation pit measurement protocols used previously for ^{4}He measurements of monazite proved to be equally successful for zircon analysis. However, the concentrations of U and Th in the zircons were sufficiently different from those in previously measured monazites that we were unable to employ the same electron microprobe methods for U + Th analysis. Our efforts to use laser ablation inductively coupled plasma mass spectrometry (LA-ICPMS) for this purpose were not successful. Although we employed a variety of different analytical protocols and normalization techniques using two different LA-ICPMS facilities, the resulting U and Th measurements – when combined with the ^{4}He data – yielded dates that did not agree with *a priori* expectations and that, in some cases,

were impossibly old. While our efforts do not confirm the viability of laser ablation (U-Th)/He dating of zircon, they illustrate issues still left to be overcome through future research..

Samples

We selected four suites of zircons for this study with over three orders of magnitude variation in age (Figure 1). Three samples (Eglab, Palisade, and Manicouagan) have well-constrained crystallization ages The age of the fourth sample (South Biscuit Basin) is <1 Ma but not well- constrained; it was selected to explore the viability of laser ablation (U-Th)/He dating of very young zircons.

Eglab Porphyry

Located in the West African craton of Algeria, the Requibath Massif consists of slightly metamorphosed to completely unmetamorphosed batholiths and associated extrusive rocks lying in and on metamorphosed sediments (Peucat et al. 2005). The massif is thought to have undergone two distinct orogenic phases, the first from 2.21-2.18 Ga, and the second at 2.07Ga. Felsic volcanic rocks derived from the latter phase comprise the majority of the Eglab series, from which this sample (EGB032, nomenclature of Schoene et al. in press) was derived. Zircons from this sample are small (40 - 100μm), euhedral colorless to light pink prisms with few visible inclusions. ID-TIMS U-Pb geochronology for the sample yields a weighted mean $^{207}Pb/^{235}U$ date of 2069.5 ± 1.7 Ma (Schoene et al. in press, 2σ). This date is in near agreement with the $^{40}Ar/^{39}Ar$ date derived from hornblende from the same sample (2054.6 ± 2.4 Ma, P. Renne personal communication as reported in Schoene et al. in press). The discrepancy between the

two dates is thought to be caused by error in the decay constant for ^{40}K used to calculate the $^{40}Ar/^{39}Ar$ apparent age (Min et al. 2000). This small difference aside, these dates are likely representative of the age of the eruption of the volcanic rocks. Unfortunately, the low-tempertaure thermal history of this sample is not known and it is plausible that EGB032 cooled through the nominal ~220 °C bulk closure temperature for (U-Th)/He zircon (Reiners, 2005) sometime after ca,. 2055 Ma. However, the lack of petrographic evidence for metamorphism of the sample and the similarity of the U-Pb and $^{40}Ar/^{39}Ar$ dates for this sample led us to expect a ca. 2060 Ma (U-Th)/He zircon age for EGB032.

Palisade Rhyolite

The Palisade rhyolite, erupted from the failed Midcontinent rift of North America (Green and Fitz III 1993), has also been the subject of extensive geochronologic studies in recent years: Min et al., (2000) determined a weighted mean $^{40}Ar/^{39}Ar$ date of 1088.4 ± 4.0 Ma for nine, sanidine grains separated from a single sample of Palisade rhyolite. U-Pb geochronology of zircons (Schoene et al. in press) yielded a weighted mean $^{207}Pb/^{235}U$ date of 1094.8 ± 1.2 Ma (2σ). Again, this sample showed no petrographic evidence of significant, post-eruption metamorphism and – if cooling progressed quickly through ~220°C – its expected (U-Th)/He zircon age would be ca.1090 Ma. From sample MS99-30 of Schoene et al, we obtained ~40, rarely included, brownish orange broken zircon crystals, 100 - 300μm in diameter, for our study.

The U-Pb dataset reported by Schoene et al. (in press), in conjunction with estimates of density and volume for the crystals used in that study, permit us to make a rough estimate of ~60 ppm for U concentrations in at least some Pallisades zircons. The reported mean Th/U ratio for the

Schoene et al. (in press) dataset suggests a Th concentration of ~50 ppm. These values are useful for comparison with LA-ICPMS results reported later in this chapter.

Manicouagan Impact Melt Sheet

Preliminary geochronology of the coarse-grained, leuococratic melt sheet of the Manicouagan impact structure, Quebec, Canada, was performed by Hodych and Dunning (1992), and is being confirmed by the work in progress of Ramezani et al., (2005). So far, this study has resulted in a weighted mean $^{206}Pb/^{238}U$ date of 215.56 ± 0.05 Ma. $^{40}Ar/^{39}Ar$ K-feldspar dates from the same unit yield a slightly younger weighted mean age of 214.48 ± 0.48 Ma (Ramezani et al., 2005). As an impact melt, we would expect the Manicouagan sheet to have cooled very quickly and this expectation is supported by the similarity of the U-Pb and $^{40}Ar/^{39}Ar$ dates. From the sample MANIC12 of Ramezani et al., we obtained a number of subhedral zircon fragments from 100-300μm in diameter. These zircons are commonly broken during crushing, likely the result of a lack of structural integrity due to large melt channels observed in many crystals. Despite this, we were able to select a large number of useful fragments, for which we expected to obtain a (U-Th)/He zircon age of ca. 215 Ma. As was the case for the Pallisades zircons, the dataset of Ramezani et al., (2005) permits a rough prediction of parent element concentrations in zircons from the Manicouagan melt sheet: U ~ 500 ppm and Th ~ 1100 ppm.

South Biscuit Basin rhyolite

The South Biscuit Basin rhyolite flow is part of the Yellowstone caldera complex of Wyoming and adjacent Idaho and Montana. The unit was only recently differentiated from its

sister units (North and Middle Biscuit Basin flows) on the basis of oxygen isotope analyses (Bindeman and Valley 2000). Gansecki et al., (1996) obtained a $^{40}Ar/^{39}Ar$ sanidine date of 516 ±7 ka for the Middle Biscuit Basin flow, but there are, as yet, no age constraints for the South Biscuit Basin flow. The lack of field evidence for a significant age difference of the two flows leads us to expect a ca. 500 ka (U-Th)/He zircon age for the South Biscuit Basin flow. The sample YCV-11 from which the zircons for this study were obtained is a fresh, unmetamorphosed, crystal-poor vitrophyric rhyolite.

General notes on sample selection

The zircons chosen for this sample are all amenable to laser microprobe analysis, but might have proven variably difficult to date accurately via conventional methods (House et al. 2000). Optimal crystals for conventional analysis are euhedral, with simple, easily defined geometries which permit accurate ejection corrections (Farley et al. 1996). In contrast, the Manicouagan and Palisade rhyolite zircons studied here were at least somewhat damaged during crushing. Crystals below 100μm in their minimum dimension (such as the majority of the Eglab zircons) are also not ideal for conventional analyses because the ejection correction increases with decreasing size. The ability to accurately date zircons by conventional (U-Th)/He means is also compromised by strong zoning in U and Th (Hourigan et al. 2005), which may be the case for at least the one (South Biscuit Basin) of the four zircon suites studied here.

Methods

Sample Preparation

Individual zircon crystals were liberated from their host rocks via standard crushing and separation techniques. Approximately 40 individual crystal and crystal fragments were picked by hand for a paucity of visible inclusions at 150x magnification. Following the procedure of Boyce et al., (in review), the zircons were mounted in epoxy, and polished by hand using successively finer diamond grits down to a minimum size of 0.05μm. Crystals were imaged via backscattered electrons and cathodoluminescence (CL) using the JEOL JXA - 733 SuperProbe at MIT (Figure 1). During image acquisition, the beam accelerating voltage was 15 keV, the beam current was 10- 20 nA, the dwell time was 0.2 s, and the image resolution was set to 400 lines per image. Samples were then removed from the epoxy mount, and remounted in indium metal discs. While indium is not strong enough to hold samples during polishing, it is an ideal medium for ultra-high vacuum applications such as noble gas measurement.

Helium analyses

Indium discs containing zircon crystals were loaded onto a copper planchette in a chamber with a UV-transparent glass window, again following the procedures of Boyce et al., (in review). Roughly cylindrical ablation pits were created by applying 30 – 150 pulses of an excimer laser operating at a nominal wavelength of 193nm and a pulse frequency of 3 - 15 Hz.

Radiogenic ^{4}He liberated during laser ablation was spiked by adding a known quantity of ^{3}He, then purified by exposure to active metal getters for 3 minutes. ^{4}He/^{3}He ratios were measured on a Blazers Prisma 200 quadrupole mass spectrometer using an signal processing algorithm written at MIT. The Balzers quadrupole is limited to increments of mass (per charge) of 0.03 AMU. This can be problematic because the peaks observed at masses 3 and 4 are typically quite narrow, and are subject to small shifts even during analyses. Several hundred

replicate analyses of double-spiked "standard" $^4He/^3He$ ratios indicate a propensity for a bimodal distribution of $^4He/^3He$ ratios, as the peak shifts between the two nearest fractional masses. In order to account for this, an algorithm was devised to measure a series of masses near the mass of interest, and then a polynomial fit to those masses was used to calculate a maximum interpolated peak height. With this approach, the distribution of $^4He/^3He$ ratios was found to be unimodal, and the measured variation was reduced from 0.5% to 0.1% (2σ). This ability to more precisely measure our "standard" aliquot of ^4He increases our confidence in the measured ^4He of unknowns (Table 1), as discussed later in the paper when we analyze the measured ages for potential sources of error.

Volume measurements

In order to calculate ^4He concentrations from molar data, we must quantify the volume of material excavated during the analysis. Ablation pit volumes were measured by optical interferometeric microscopy on an ADE Phase Shift MicroXAM microscope, with a methodology identical to that of Boyce et al., (in review).

LA-ICPMS measurements of U and Th

Unlike previous laser microprobe studies of monazite (Boyce et al. in preparation; Boyce et al. in review) which utilized the electron microprobe to measure U and Th, we have chosen laser-ablation inductively coupled plasma mass spectrometery (LA-ICPMS). U, Th, and Sm concentrations in zircon can be too low (10 - 50 ppm) to accurately measure with the electron microprobe under standard operating conditions, and this represents the fundamental difference between this study and previous successful applications of laser microprobe (U-Th)/He. The

potential application of high-sensitivity electron microprobes such as the Cameca Ultrachron at the University of Massachusetts at Amherst, for future work is discussed in a later section of the paper.

Two different sets of analyses were performed at two different LA-ICPMS laboratories. The first set of measurements (Table 1) were made in the Department of Earth Sciences at Boston University (analyses which are here abbreviated BU). Samples were placed in a helium gas stream, and ablated by a frequency-quintupled (213nm) Nd-YAG laser operating at ~0.6 mJ energy, with the following additional settings: iris = 80; beam expander = 100; power = 40%; frequency = 5 or 10Hz. We measured the following elements (masses in parentheses) during the each ablation: Si (29, 31); Ti (47, 49); Zr (96); In (113); Hf (177, 178, 179); Pb (204, 206, 207, 208); Th (232); U (235, 238). Sm concentrations are very typically low in zircon, usually at least an order of magnitude below U and Th concentrations (Thomas et al. 2002; Hoskin and Schaltegger 2003; Amelin 2004), and therefore not easily measured using LA-ICPMS. However, low concentrations of Sm likewise mean that it does not contribute significantly to calculated ages, an assertion discussed below.

Each analysis consisted of 60 seconds of blank run and 60 second of sample measurement (during lasing). Measurements were made via rapid peak hopping with 0.1 ms measurements. External standardization was accomplished via bracketing every ~10 zircon analyses with measurements of standard glasses NIST 610 and 612. Internal standardization was accomplished by two different methods. First, we attempted to use stoichiometric Zr as our internal standard, and corrected iteratively for Hf, which is assumed to most abundantly substitute for Zr. In this case, we assume that the Zr concentration in these zircons is nearly stoichiometric, with the major substitution being Hf, as it is unlikely that any other cation is

present any of the three Zr sites in zircon in a sufficient quantity to measurably change the overall concentration of Zr (~ 50% by weight of $ZrSiO_4$). The same data were then reduced using Hf as the internal standard, referenced to Hf measurements made on the JEOL Superprobe at MIT (Table 2). As discussed below, the choice of Zr or Hf as the internal standard element has a significant effect on the resulting U and Th concentrations. Reduction of data from BU performed with LasyBoy 3.0 software, written by Joel Sparks at Boston University. Uncertainties in U and Th concentrations reflect a combination of the counting statistics on $^{238}U/^{96}Zr$ and $^{232}Th/^{96}Zr$ or $^{238}U/^{178}Hf$ and $^{232}Th/^{178}Hf$ ratios, the error on measured NIST glass compositions with respect to known NIST concentrations, and the uncertainty in the electron microprobe measurements of Hf (where applicable). Total uncertainties range from 1-15%, and are largely a function of the internal standard used. As demonstrated here, using Hf as the internal standard results in more reasonable U and Th estimates, but at the cost of larger uncertainties because the uncertainty in the Hf measurement is larger than the uncertainty in the Zr estimate. Beyond the method used to normalize the data, uncertainties are a function of composition, with large concentrations being easier to measure precisely than small concentrations. Unfortunately, this assessment of uncertainty does not take into account any problems in the accuracy of the technique beyond the ability to reproduce glass standards. The possible difference between analyses of zircon and glasses is discussed below.

Selected zircons were also analyzed in the Department of Earth Sciences at Memorial **University, Newfoundland,** Canada (MUN). The analytical system used at MUN is a HP4500 ICP-MS instrument coupled to a NUWAVE UP 213nm Nd-YAG laser. Ablations were performed in helium carrier gas, which was combined with argon just prior to the feed to the torch. Nebulizer flow rates were 0.91 l/min He and 0.74 l/min Ar. Laser energy varied from

approximately 0.06 mJ (about 9 J/cm2) at a laser repetition rate of 10 Hz, producing a 30 μm diameter spot on the sample. Time resolved intensity data were acquired by peak-jumping in pulse-counting mode with 1 point measured per peak for masses ^{172}Yb, ^{175}Lu, ^{178}Hf, ^{179}Hf, ^{232}Th, and ^{238}U. (While unnecessary for Th and U analytical purposes, the measurement of ^{172}Yb was designed to increase the quadrupole settling time after the jump from high to low mass in each sweep). Quadrupole settling time was 1 msec and the integration (or dwell) time was 10 msec on Yb and Lu and 100 msec for Hf, Th and U. The total sampling time for this analysis was 0.4335 s with an acquisition window of about 100 s.

Gas background data were collected for approximately 33 s with the laser beam blocked prior to each 66-s ablation of standards and unknowns. NIST glass 610 was used as reference material and analyzed in the first and last two positions of each run. Zircon reference material 91500 (MUN Chip 3) was analyzed as an unknown three times during each run. The Hf abundance in 91500 (5649 ppm as determined by electron microprobe analysis at Memorial University) was used as an internal standard for data correction. Previous MUN studies on 91500 (Chip 3) yielded a Th/U ratio of 0.3465. Replicate analyses of this standard during the present study yielded an average Th/U ratio of 0.3403, a difference of less than 2%.

Data were reduced using MUN's in-house CONVERT and LAMTRACE spreadsheet programs, which employ procedures described by Longerich et al. (1996). The total uncertainty for the method is estimated to be better than 10% relative based on the reproducibility of results for various reference materials measured from day to day over several months in our laboratory. For this reason, uncertainties in U and Th concentrations were estimated at 10% (2σ) for the purposes of calculating (U-Th)/He dates.

One procedural challenge associated with laser microprobe (U-Th)/He geochronology is that He and U + Th cannot be analyzed in the same aliquot of extracted gas. When LA-ICPMS is used for U + Th measurements, there are two alternative strategies to maximize the likelihood that the measured parent element abundances are representative of the abundances found in the material that was previously ablated for ^{4}He analyses: 1) the laser connected to the inductively coupled plasma mass spectrometer can be targeted at the pre-existing ^{4}He ablation pits; or 2) new pits can be ablated as closely as possible to the pre-existing pits. Both approaches were employed at Boston University and Memorial University. In several cases, where it was permitted by grain size, a second or third ablation for U + Th measurement was performed adjacent to the ^{4}He pit, in order to evaluate the intragrain variations. Values are reported in Table 1 with 2σ uncertainties which include counting statistics and the uncertainty associated with the measured reproducibility of standards.

Age calculations

Concentration data for U, Th, and He are combined in the standard decay equation for production of ^{4}He, modified to account for secular disequlibrium (Farley et al. 2002). The density of zircon was assumed to be 4700 kg/m^3, which may contribute to the error in the ages, a possibility discussed below. Ages are shown in Figures 2 – 4 and Table 1, with all uncertainties reported at 2σ.

Results

Cathodoluminescence Images

The four zircon suites studied here each have very different chemical structures, as evidenced by different patterns of CL intensity. Eglab zircons (Figure 1a) are typified by small (< 20 μm) homogeneous euhedral cores, surrounded by apparently oscillatory zoning on the scale of ~ 5 μm. Zoning of this type is typically interpreted as the representative of magmatic growth (Corfu et al. 2003). In contrast, the larger Palisade zircons (Figure 1b) are dominated by large (≥ 100 μm) cores that appear either homogeneous or weakly zoned cores; weakly defined oscillatory zones, ranging from ~10μm to less than 1μm, occur near the grain edges. In several grains, well-developed sector zoning was observed. Manicouagan zircons (Figure 1c) are very weakly zoned in CL intensity, with a few grains showing apparently homogeneous cores. The most dramatic zoning is observed in the images of zircons from the South Biscuit Basin flow (Figure 1d), as a combination of concentric and sector zoning. Euhedral dark cores are surrounded by brighter rims with even brighter thin sector zones often observed parallel to prism faces. These zones are often, in turn, surrounded by darker sectors at the crystal edges. Although CL zoning is not simply a reflection of U zoning (Nasdala et al. 2003), we assume here that darker (CL-suppressed) regions are enriched in U relative to lighter regions in the same crystal. The reader is warned, however, that no relative U-concentration relationship between grains can be determined using two different CL images, because the images have had their contrast and brightness adjusted both during and after the course of the imaging.

Helium measurements

Blanks at masses 3 and 4 were typically < 2 x 10^{-18} and < 2 x 10^{-16} moles, respectively (Table 1). Radiogenic He measurements range from 3 x 10^{-16} to 5 x 10^{-14} moles, with most uncertainties under 1% (2σ), except for YCV11 (South Biscuit Basin), which has uncertainties

from 3 - 9%, due to the smaller amount of ^{4}He being measured. This increased uncertainty stems from the small signal to blank ratios for the YCV11 spots, which averages ~3:1. ^{3}He spike quantities are ~ 8 x 10^{-14} moles for all analyses, and are always > 4 orders of magnitude greater than the blanks at mass 3, which includes hydrogen species such as HD^+ and H_3^+.

Volume measurements for ^{4}He Ablation Pits

Excimer laser ablation using the operating specifications described above resulted in pits with diameters ranging from ~30-60 μm and with depths of ~3-15 μm. Pit depths scaled linearly with the number of pulses fired, with the mean depth per burst of ~ 0.1 μm. This is comparable to the depth/pulse observed for monazite (Boyce et al. in review), suggesting that the interaction of the laser with zircon is roughly comparable to the interaction with monazite. As was the case with monazite, replicate optical interferometric measurements of the excimer ablation pits in zircon were generally quite reproducible, with a precision of $\leq$ 2% at 2σ.

U and Th measurements (Boston University – Zr internal standard)

U and Th concentrations normalized to Zr show the widest range of any parameter measured in this study (Table 1). Eglab zircons have consistently low U (23 – 63 ppm) and Th (18 – 40 ppm) concentrations, except for EGB032-39, which has concentrations higher by a factor of roughly five: U = 175 ppm, Th = 130 ppm. Palisade zircons have similarly low concentrations of U (15 – 50 ppm) and Th (10 – 37 ppm, with one outlier at 90 ppm), lower than the ~60 ppm U and higher than the ~50 ppm Th calculated from the Schoene et al. (2005) dataset. Manicouagan zircons display a much wider range of apparent U and Th concentrations (U = 183 – 899 ppm; Th = 378 – 3342 ppm) than would be expected from the low contrast observed in CL images. Multiple analyses of one single crystal indicated a factor of two variation

in Th concentration. The wide range of concentrations observed does overlap the average concentrations for both U and Th predicted by the Ramezani et al. (2005) dataset. South Biscuit Basin zircons show an even greater apparent range of concentrations, with U values ranging from 93 – 3212 ppm, and Th from 34 – 2214 ppm. Interestingly, while these grains might be expected to show large variations within single grains because of the large CL contrast observed, multiple analyses on two different crystals show very little variation.

U and Th measurements (Boston University – Hf internal standard)

Use of Hf as the internal standard results in consistently higher U and Th concentrations for the Palisade, Manicouagan, and South Biscuit Basin samples. Palisade zircon U concentrations ranged from 47–118 ppm, while Th concentrations varied from 33–216 ppm. Manicouagan zircons had consistently higher and more variable concentrations (U = 440–2144 ppm; Th = 890–3564 ppm) than the Palisade zircons, while we observed an even greater range of concentrations for the South Biscuit Basin zircons: U = 208 – 7513 ppm; Th = 89 – 5180 ppm.

U and Th measurements (Memorial University – Hf internal standard)

Significantly fewer measurements were made at MUN, so it is difficult to directly compare the ranges of U and Th concentrations observed. For the Palisade rhyolite zircons, concentrations varied from 30–79 ppm U, and 17–68 ppm Th. On average, these values are much lower than the Hf normalized concentrations obtained from BU, but closer to the values estimated from thermal ionization mass spectrometry data (Schoene et al., 2005). Concentrations obtained for Manicouagan zircons are similar to or higher than the BU values,

and generally higher than the TIMS-derived estimates. South Biscuit basin rhyolite zircons show the largest change in U and Th values, with MUN concentrations being roughly two-thirds to three-quarters lower than those determined at BU on the same grains. The possible causes of these variations are discussed below.

(U-Th)/He dates (Boston University - Zr)

(U-Th)/He dates calculated for the four suites of zircons are given in Table 1 and compared with U-Pb crystallization ages for zircons from the same samples in Figure 2. Dates for zircons from the Eglab porphyry ranged from 1174 ± 214 Ma to 3077 ± 412 Ma. While this large range includes the expected age (ca. 2060 Ma), many calculated dates are impossibly old and no single date is within 380 m.y. of the expected age. Zircons from the Palisade rhyolite yielded apparent ages ranging from 1577 ± 41 Ma to 2388 ± 52 Ma. In this case, all dates are impossibly older than the crystallization age. Ablation pits in the Manicouagan zircon had (U-Th)/He apparent ages ranging from 271 ± 6 Ma to 510 ± 13 Ma, with no analyses within uncertainty of the expected age of ca. 215 Ma. (U-Th)/He dates for the < 1Ma South Biscuit Basin flow zircons are scattered between 0.7 to 20.7 Ma.

(U-Th)/He dates (Boston University - Hf)

Using the Hf-normalized U and Th concentrations, we can recalculate the ages based on improved estimates of U and Th (Figure 3). In this case, the weighted mean (U-Th)/He date for the Palisade rhyolite is 831 ± 303 Ma (2σ) or ± 64 Ma at two standard errors of the mean (2SE). While this date is not demonstrably impossible, it seems unlikely to be correct given the probable rapid cooling of this volcanic sample. The weighted mean of the Manicouagan zircons (again

using the Hf – normalized U and Th concentrations, but deleting two statistically defined outliers) is 177.5 ± 44 Ma (2σ) or ± 9.6 Ma (2SE). Again, this apparent age is not impossible, but it is significantly lower than expected. South Biscuit Basin zircons yielded a weighted mean age of 0.41 ± 3.4 (2σ) or ± 0.43 Ma (2SE), which is suggestive of a correct age determination, but with an unacceptable amount of dispersion about the mean. This value is also heavily influenced by one date with a small uncertainty: the unweighted mean of these same dates is 3.0 Ma.

(U-Th)/He dates (Memorial University - Hf)

For a selected number of zircons from three of the four samples, we were able to recalculate the ages based on the U and Th values determined at Memorial University (Figure 4). This exercise yields a weighted mean age for the Palisade rhyolite of 1059 ± 1201 Ma (2σ) or ± 390 (2SE). To fairly compare this smaller dataset with the BU results, we can select from the BU-derived ages only the spots that were repeated at MUN. This results in a modified BU weighted mean (N = 6) of 801 ± 349 Ma (2σ) or ± 110 Ma (2SE), which is actually within uncertainty of the MUN-Hf result but substantially lower than the expected result. Average date based on all MUN data is only ~3% less than the predicted age of 1095 Ma, but with a distribution of ages resulting in a two standard deviation value greater than the age.

The five analyses on Manicouagan zircons repeated at MUN yield a mean date of 168 ± 125 Ma (2σ) or ± 54 Ma (2SE). This mean date is similar to the mean of the same spots using BU concentrations of U and Th: 175 ± 35 Ma (2σ) or ± 23 Ma (2SE), but individual ages are considerably more dispersed, resulting in the significantly larger standard deviation of the sample population.

Only three South Biscuit Basin analyses were amenable to reanalysis at MUN, yielding a mean age of 6.7 ± 4.2 Ma (2σ) or ± 5.2 Ma (2SE), a dramatically different value than both the BU weighted mean date (0.41 Ma) or the directly comparable subset of the BU dataset: 2.1 ± 2.1 Ma (2σ) or ± 2.2 (2SE).

Discussion

The most important result of our study is that we do not yet have a fully effective laser ablation protocol for (U-Th)/He zircon geochronology. Presuming that our *a priori* assumptions regarding the (U-Th)/He ages of the zircons are correct, none of the protocols we tried yielded satisfactory results. The Zr-normalized BU data generated the least accurate weighted mean dates, albeit with the smallest uncertainties on the individual spot dates because of false precision on the U and Th analyses. Recalculating the U and Th concentrations measured at BU using Hf as an internal standard yields much more accurate mean dates, which in all three cases were within two standard deviations of the expected ages of the crystals. However, in all cases the individual spot ages displayed an unacceptable amount of dispersion, resulting in the very large standard deviations on each sample population. Reanalysis of selected zircons at MUN resulted in weighted means that were significantly different in all samples but the Manicouagan zircons. In all cases the mean squared weighted deviations for the data were higher for the MUN analyses than the BU analyses, suggesting either an underestimation of the actual imprecision of the MUN data or substantial (and otherwise inexplicable) intracrystalline variations in (U-Th)/He age.

Our inability to attain reasonable results could be due to incorrect expectations regarding the ages of the analyzed zircons, errors in ^{4}He measurements, errors in ^{4}He ablation pit volume measurements, or errors in LA-ICPMS measurements of parent element concentrations. We have

no way to assess the first of these assumptions because there are no conventional (U-Th)/He data available for these materials, but we note that – even if the assumptions are erroneous – the observed variation of laser ablation ages for individual zircon samples is unacceptably high. It seems likely, therefore, that measurement errors have played an important role in our failure to make accurate and precise age determinations. Below we explore each potential source of measurement error.

Helium Measurements

It is difficult to envision a scenario in which the helium measurements could be the source of errors of the magnitude required to generate the observed discrepancies in apparent age. Although the laboratory for noble gas geochronology at MIT recently changed measurement protocols, hundreds of standard (double-spiked) measurements demonstrate that the new protocol can retrieve more precise $^4He/^3He$ ratios than the peak fitting routines used in previous, successful laser microprobe (U-Th)/He studies. In addition, ^3He measurements were within the expected range based on estimated sensitivities and molar quantities of ^3He introduced during analyses. Finally, there is no correlation between ^4He measurements and (U-Th)/He dates (Figures 5-7) for any suite of zircons analyzed here, which would be expected in ^4He were responsible for the scatter in the dates. Therefore we conclude that the ^4He measurements are not responsible for the lack of accuracy in the calculated dates.

Volume Measurements

^4He ablation pit volumes for this study spanned a wide range – approximately a factor of 5 in depth and factor of 7 in volume. This range overlaps with volumes from the study of Boyce

et al., (in review), which yielded reliable cooling age determinations on monazite. Given that the two studies utilized the same volume measurement protocols, we find it unlikely that the poor accuracy and precision of the mean (U-Th)/He dates were caused by the volume measurements. The second line of evidence for this, at least with regard to precision, is the lack of a correlation ($R^2 < 0.2$) of age with volume^{-1} (Figures 5-7) for all studied zircons – again with the exception of MUN-derived ages. All the samples, save the Eglab zircons, have at least a factor of two variation in volume, and we would expect to see a relationship between age and volume if those measurements were responsible for the scatter observed.

A second possibility is that the measured volume and the volume from which the ^{4}He was liberated are not the same. If excess ^{4}He were liberated from the zircon outside of the pit, we would expect the ages to be too old, as the ^{4}He concentration would be overestimated. The magnitude of the effect of excess ^{4}He should be a function of the amount of heating of the sides and bottom of the pit, the diffusivity of ^{4}He in zircon, and the ratio of the surface area to volume of each pit. With regard to heating, we observe that the interaction of the laser with zircons is approximately as efficient as it was with monazite, resulting in ~ 0.1μm of ablation depth per pulse. If ablation depth per pulse is an effective measure of coupling efficiency, then we can assume that the laser behaved as well for this study as it did for Boyce et al., (in review). As no evidence for incidental heating was observed for monazite (and the two minerals are unlikely to have significantly different thermal diffusivities), we regard this as an unlikely cause, with the caveat that the diffusivity of He in zircon is slightly higher than for monazite, and thus helium will diffuse slightly faster in zircon at any given temperature.

An additional line of evidence exists with regard to this hypothesis. As the volume of a pit increases, the ratio of surface area to volume decreases, and therefore any ^{4}He released by

incident heating becomes less significant with respect to the total ^{4}He released. Thus, we would expect to see a relationship between volume and age, with older ages corresponding to smaller pits which have lower surface areas per volume. As previously mentioned, there is no such correlation. We conclude that errors in ^{4}He ablation pit volume measurements are not the major cause of the erroneous ages obtained in this study.

Uranium, Thorium and Samarium Measurements

U and Th show the largest percent variation of any variable used to calculate the dates reported here, and are therefore likely suspects in the hunt for sources of error. In addition, the change in U and Th measurement technique is one of the most apparently significant differences between this study and previous successful applications of laser microprobe (U-Th)/He. Here we explore the relationships between the calculated (U-Th)/He dates and the U and Th concentrations measured at Boston University (using both Zr and Hf as the internal standard), and Memorial University (using only Hf). Note that the paucity of MUN analyses makes any correlation analyses on those few data suspect at best.

1. External Standardization – Use of NIST glasses

A likely source of error in the LA-ICPMS measurements involves the standard glasses used as external standards. NIST standard glasses 610 and 612 are silicate glasses doped with ~400 and ~40 ppm (respectively) of more than 40 trace elements including U, Th, and the rare earth elements. Because the ratios of Th/Zr and U/Zr in these glasses (~1) and the zircons (~10^{-4} to 10^{-2}) are very different, the calibration requires extrapolation over several orders of magnitude.

The same can be said of the U/Hf and Th/Hf ratios which are different in the glass standards (~1) and in zircon (variable, between 1 and 50).

Although their geologically unusual compositions make NIST glasses useful standards for analysis of many different elements, it is at the expense of significant matrix effects (Hirata and Nesbitt 1995). Physical evidence for matrix effects stems from observations that the interaction of the quintupoled ND-YAG laser with the NIST glasses is measurably poorer than with natural glasses, resulting in irregular ablation pits and lower yields. Similar observations were made with regard to the zircons in this study, which showed much more regular ablation characteristics than the NIST glasses.

Elemental fractionation has been observed in many previous quadrupled and quintupled Nd-YAG ICPMS studies (see summary in Gunther and Hattendorf 2001). Although elemental fractionation can be reduced significantly by the use of internal and external standards as was done here, the character of both standards is important. With regard to the internal standard, the ideal element has a fractionation index (Fryer et al. 1995) similar to the elements of interest. In our case, Zr and Si are the only two elements available in sufficient quantities in the zircon to be used as a standard without employing the electron microprobe for standard composition measurements, and Si isotopes are less useful because of high backgrounds. If one wishes to use the electron microprobe to determine an independent internal standard composition, Hf is the only element with high enough concentration to be useful.

With regard to external standards, no zircons homogeneous in their trace elements have been observed by myself or my colleagues, forcing the use of NIST glasses. Unfortunately, NIST glasses have been demonstrated ineffective as external standards for precise measurements

of Pb/U and Pb/Th ratios in zircon (Hirata and Nesbitt 1995), which may translate to the Th and U measurements made here as well.

2. U and Th (Boston University – Zr)

Using Zr as the internal standard yields a set of dates that are not only very different from the expected dates, but also correlate very strongly with U^{-1} and Th^{-1}. Significant correlation between U^{-1} or Th^{-1} and (U-Th)/He date is observed for Eglab (R^2 = 0.37 for U, R^2 = 0.62 for Th), Palisade rhyolite (0.60, 0.26), and South Biscuit Basin (0.72, 0.72) zircons, but not for Manicouagan zircons (0.05, 0.06). This suggests strongly that, for three of the four samples, the variation in apparent age can be in large part attributed to the U and or Th measurements. However, although this may explain a large part of the variations seen within each suite, and it is suggestive of larger problems, it does not specifically explain the overall offset to older dates observed for each rock.

3. U and Th (Boston University –Hf)

Recalculation of (U-Th)/He dates using the BU-derived U and Th values (with respect to Hf) yields weak correlations for the Manicouagan and Palisade dates (all $R^2 < 0.23$), while South Biscuit basin dates show moderate correlation with U and with Th with R^2 values of approximately 0.5. This could be interpreted as suggesting that the U and Th concentrations using Hf as the standardization element are contributing much less to the dispersion in the observed (U-Th)/He dates, with the exception of the South Biscuit Basin samples, which may

still be influenced by variations in U and Th concentrations. This assertion is validated by the ages themselves, which are for the most part much greater than the expected age (Figure 3).

4. U and Th (Memorial University – Hf)

Because only a few data were amenable to being reproduced at MUN, the value of a correlation analysis is suspect: Random distributions can show apparently strong correlations for small N even in cases where no true correlations exist (and *vice versa*). This concern notwithstanding, strong correlations (all $R^2 > 0.88$) are observed for Palisade and South Biscuit basin suites (N = 6 and N = 3, respectively), while the Manicouagan samples (N = 5) show weak correlations between dates and U and Th values (both $R^2 < 0.12$)

5. Intragrain Variations in U and Th

Although the Boston University U and Th measurements were located in such a way as to most closely approximate the volume of the crystal that would have contributed to the ^{4}He production in the pit, it is possible that the scatter observed is due (at least in part) to measuring He and U+Th to different domains of chemically zoned crystals. For example, the LA-ICPMS pits may have been too large or not large enough to sample the volume of material appropriate to the size of the pit. The ideal diameter is equal to the diameter of the helium measurement pit plus twice the ejection distance, which for zircon is ~18μm. The 213nm system at BU does not have precise beam diameter control, and thus we used settings that generated ablation pits that were ~70μm in diameter. This diameter is appropriate for the majority of the 30-40μm ablation pits in this study, but because of the possibility of sharp U and Th concentration changes important source zones of ^{4}He (such as monazite inclusions or small zones of higher U or Th concentration) may have been inadvertently included or omitted where not appropriate. Another

possibility is that there may have been very small inclusions or zones (perhaps below the surface) within the regions ablated for He analyses, which contributed to the ^{4}He production but were destroyed during the laser ablation required for He analysis. This is a totally untestable hypothesis because the two-dimensional CL map for each grain is neither a map of U and Th variation, nor a reliable predictor of the distribution of U and Th below the surface imaged.

For the measurements repeated at MUN, the U and Th analyses were necessarily located at least ~50μm away from previous holes. While every effort was made to use CL images to locate regions of the crystal with similar CL characteristics (and therefore presumably U and Th concentration), this does not mean that intracrystalline U and Th variations did not affect the dates. In fact, differing U and Th from place to place within these crystals is a likely explanation for the increase in the MSWD of ages determined with MUN values of U and Th with respect to the BU measurements made on the same crystals.

6. The Possible Effect of Samarium

Samarium concentrations in zircons are typically an order of magnitude lower than U and Th, and therefore Sm plays only a minor role in alpha production (Amelin 2004). In part this is due to the fact that Sm only generates one alpha particle per ^{147}Sm, as opposed to U and Th, which generate 6-8 ^{4}He per parent atom. ^{147}Sm is also only 15% of all Sm atoms, further reducing the impact of Sm on (U-Th)/He dates. Finally, the difference between the decay rates of U, Th, and Sm also limits the effect of Sm: The mean life of Th is only ~3 times longer than that of U, but the mean life of Sm is a factor of ~24 longer, further reducing ^{4}He production by over an order of magnitude.

That being said, it is still a useful exercise to calculate the increase in Sm concentration that would be necessary to bring the (U-Th)/He dates into agreement with the known ages of these zircons. Only zircons with (U-Th)/He dates in excess of the predicted age could possibly be explained by Sm-produced alpha particles. As an example, consider the dates generated using the Zr- normalized Boston University U and Th data. In the case of the Eglab zircons, ~28,000 ppm would be required to "correct" the mean date, while for Palisade and Manicouagan zircons, ~35,000 and 40,000 ppm would have to be added to make the (U-Th)/He dates and predicted ages agree. For the South Biscuit Basin zircons, even if they were composed of 100% Sm, they could still not have produced the required number of alpha particles in less than 1 Ma. Obviously only unreasonably large concentrations of Sm (orders of magnitude greater than the typical values, see reference above) could significantly change the calculated (U-Th)/He dates.

7. Density of Zircon

In order to convert the ppm concentrations derived from LA-ICPMS analyses to moles, we had to assume a density for the zircons we analyzed. We have used 4700 kg/m^3 for these calculations, but this value may be slightly too high, depending on the degree of metamictization and elemental substitution in these particular zircons. However, zircons are not likely to vary greatly in density within a single sample, making density and unlikely explanation for the variability observed in the (U-Th)/He dates for individual units. This complication could be avoided entirely if U and Th data could be reduced as mole fractions instead of the more common mass fractions (parts per million, or grams per 10^6 grams).

Conclusions and ruminations

Laser microprobe (U-Th)/He geochronology on four suites of zircons yields dates that are all significantly different than the expected ages. The data for different suites demonstrate different amounts of variability in addition to inaccurate weighted means, making it likely that there is more than one source of error affecting the ages. Depending on the choice of analytical protocol and internal standard, variably strong correlations are observed between parent elements and apparent age for three of the four samples, suggesting that calibrations are incorrect or that intragrain variations affect (U-Th)/He dates to a greater extent than is accounted for by the U and Th measurements.

In order to more closely examine of the effect of U and Th measurements of (U-Th)/He dates, three different analytical protocols were used to determine the U and Th concentrations. First, stoichiometric Zr (corrected for Hf) was used as the internal ICPMS standard, resulting in strong correlations with the (U-Th)/He dates, and large offset between (U-Th)/He dates and predicted ages. These same data were then reduced using Hf as the internal standard instead. The result was an increase in U and Th uncertainties, but (U-Th)/He dates that are much closer to the predicted ages. Finally, several samples were reanalyzed in a different facility using different laboratory and data reduction protocols, yielding a third set of (U-Th)/He dates that in two of the three cases differed significantly from previous (U-Th)/He estimates in this study. Using U and Th concentrations derived from ID-TIMS analyses yields a mean date for the Palisade rhyolite within 5% of the known age, a significant improvement over the estimates derived from the various LA-ICPMS U and Th values. A similar improvement was observed for Manicouagan (U-Th)/He ages (errors reduced from >18% to only 12%).

The Future of Laser Microprobe (U-Th)/He of Zircon

We regard the principal obstacle to successful laser ablation (U-Th)/He zircon geochronology as the need to obtain better U and Th microanalytical measurements. One strategy to improve the current situation while still focusing on LA-ICPMS technology is to abandon NIST glass standards in favor of zircon mineral standards. The problem with this is that no natural zircons have been identified that are homogeneous in U and Th to better than a few percent. It may be possible to grow homogeneous zircons, though previous attempts using flux-melting techniques have produced crystals zoned in rare earth elements (Hanchar et al. 2001), leading us to believe that U and Th would be similarly (and possibly more strongly) fractionated. Other techniques exist for growing crystals – including hydrothermal precipitation (Manning 1994) and flame fusion in a vernueil furnace (Gentile et al. 1963) – but neither technique has demonstrated the capability to grow crystals unzoned in volatile trace dopants such as U. An alternative to growing a homogeneous zircon might be to crush natural heterogeneous zircons into a sub-micrometer powder and then fuse it into a solid strong enough to ablate like a crystal of zircon during LA-ICPMS. However, it is not known if a sample can be given sufficient strength by sintering without U volatilization and loss. Perhaps a zircon powder could be deformed at high enough temperature so that it behaves plastically, but not so high that U is volatilized out of the structure of the zircon powder, allowing the mechanical mixture to be pressed into a solid suitable for LA-ICPMS.

Secondary ion mass spectrometry (SIMS) provides an alternative to LA-ICPMS. The ability of SIMS to accurately and precisely measure rare earth elements in apatite and zircon is somewhat questionable, with deviations from ID-TIMS values of up to 30% reported (Sano et al.

2002), but given appropriate standards, it mat be able to outperform the LA-ICPMS, and is worth exploration.

Finally, we must consider the possibility that employing the electron microprobe, per the original methodology of Boyce et al. (in review), might have worked better than using LA-ICPMS. With extended counting times, measurements of U and Th concentrations as low as 10 ppm should be feasible using the most recent generation of electron microprobes, such as the Cameca Ultrachron at the University of Massachusetts, Amherst (M. Jercinovic, personal communication, 2005). The greatest impediments to measuring U and Th in this manner are the interferences created by high Th/U ratios, which decrease the accuracy of the U measurement. However, this effect is anticipated to be insignificant for Th concentrations below ~0.5 % by weight. Future attempts to apply laser microprobe (U-Th)/He to zircon should make an attempt to use the UMASS Ultrachron for U and Th measurements, if for no other reason than that the technique is non-destructive, and measurements can subsequently be duplicated by SIMS or LA-ICPMS.

Acknowledgements

Terry Plank is thanked for her gracious use of the LA-ICPMS at Boston University. Additional appreciation goes to Louise Bolge and Jennifer Wade for their technical assistance. Blair Schoene, Jim Crowley, and Jahan Ramezani graciously provided samples for this study. Drs. Schoene (almost), Crowley, and Ramezani, and also Malcolm Pringle are thanked for providing unpublished U-Pb and $^{40}Ar/^{39}Ar$ ages for these samples. Mike Tubrett and his colleagues at MUN are thanked for their assistance in obtaining and reducing the results of the additional LA-ICPMS study.

Figure Captions

Figure 1. Cathodoluminescence images of the zircons dated in this study, with He analysis spot locations shown as dashed circles (circles are black or white only in order to maximize contrast with image). A) Eglab. B) Palisade. C) Manicouagan. D) South Biscuit Basin.

Figure 2. Plot of laser microprobe (U-Th)/He dates (derived from Boston University U and Th values normalized to Zr) versus known ages for zircons in this study. A) Linear scale. B) Same data, but plotted in log – log space.

Figure 3. Plot of laser microprobe (U-Th)/He dates (derived from Boston University U and Th values normalized to Hf) versus known ages for zircons in this study. A) Linear scale. B) Same data, but plotted in log – log space.

Figure 4. Plot of laser microprobe (U-Th)/He dates (derived from Memorial University U and Th values normalized to Hf) versus known ages for zircons in this study. A) Linear scale. B) Same data, but plotted in log – log space.

Figure 5. Plots of (U-Th)/He dates (derived from Boston University U and Th values normalized to Zr) versus key variables involved in the calculations of those dates. Reference "true" ages plotted as dashed vertical lines. Variables appearing in the denominator of the age

equation (U, Th, and volume) are plotted to the -1 power. A) Eglab. B) Palisade. C) Manicouagan. D) South Biscuit Basin.

Figure 6. Plots of (U-Th)/He dates (derived from Boston University U and Th values normalized to Hf) versus key variables involved in the calculations of those dates. Reference "true" ages plotted as dashed vertical lines. Variables appearing in the denominator of the age equation (U, Th, and volume) are plotted to the -1 power. A) Palisade. B) Manicouagan. C) South Biscuit Basin.

Figure 7. Plots of (U-Th)/He dates (derived from Memorial University U and Th values normalized to Hf) versus key variables involved in the calculations of those dates. Reference "true" ages plotted as dashed vertical lines. Variables appearing in the denominator of the age equation (U, Th, and volume) are plotted to the -1 power. A) Palisade. B) Manicouagan. C) South Biscuit Basin.

Table Captions

Table 1. U, Th, He and volume analyses for zircons in this study, along with dates calculated from that data. All uncertainties shown at 2σ.

Table 2. Hafnium analysis for selected Palisade, Manicouagan, and South Biscuit Basin zircons. Uncertainties (not shown) are estimated at 5%, and are based on counting statistics only, and do not include uncertainties in standard compositions.

References

Amelin, Y. (2004). "Sm-Nd systematics of zircon." Chemical Geology **211**: 375-387.

Bindeman, I. N. and J. W. Valley (2000). "Formation of low-$d^{18}O$ rhyolites after caldera collapse at Yellowstone, Wyoming, USA." Geology **28**(8): 719-722.

Boyce, J. W., K. V. Hodges, et al. (in preparation). "Laser microprobe (U-Th)/He of monazite from Nanga Parbat, Pakistan Himalaya." Science.

Boyce, J. W., K. V. Hodges, et al. (in review). "Laser microprobe (U-Th)/He geochronology." Geochimica Cosmochimica Acta.

Corfu, F., J. M. Hanchar, et al. (2003). Atlas of zircon textures. Reviews in Mineralogy: Zircon. J. M. Hanchar and P. W. O. Hoskin, Mineralogical Society of America. **53:** 468-500.

Farley, K. A., B. P. Kohn, et al. (2002). "The effects of secular disequilibrium on (U-Th)/He systematics and dating of Quaternary volcanic zircon and apatite." Earth and Planetary Science Letters **201**: 117-125.

Farley, K. A., R. A. Wolf, et al. (1996). "The effects of long alpha-stopping distances on (U-Th)/He ages." Geochimica et Cosmochimica Acta **60**(21): 4223-4229.

Fryer, B. J., S. E. Jackson, et al. (1995). "The design, operation and role of laser-ablation microprobe coupled with an inductively couple plasma mass spectrometer (LAM-ICP-MS) in the earth sciences." The Canadian Mineralogist **33**(2): 303-312.

Gansecki, C. A., G. A. Mahood, et al. (1996). "$^{40}Ar/^{39}Ar$ geochronology of rhyolites erupted following collapse of Yellowstone caldera, Yellowstone Plateau volcanic field: implications for crustal contamination." Earth and Planetary Science Letters **142**: 91-107.

Gentile, A. L., D. M. Cripe, et al. (1963). "The flame fusion synthesis of emerald." American Mineralogist **48**: 940-944.

Green, J. C. and T. J. Fitz III (1993). "Extensive felsic lavas and rheoignimbrites in the Keweenawan Midcontinent Rift plateau volcanics, Minnesota: petrographic and field recognition." Journal of Volcanology and Geothermal Research **54**: 177-196.

Gunther, D. and B. Hattendorf (2001). Elemental fractionation in LA-ICP-MS. Laser ablation ICPMS in the Earth sciences: Principles and applications. P. Sylvester, Mineralogical Association of Canada. **29**.

Hanchar, J. M., R. J. Finch, et al. (2001). "Rare earth elements in synthetic zircon: Part 1. Synthesis, and rare earth element and phosphorus doping." American Mineralogist **86**.

Hirata, T. and R. W. Nesbitt (1995). "U-Pb isotope geology of zircon: Evaluation of laser probe-inductively coupled plasma mass spectrometry technique." Geochimica Cosmochimica Acta **59**: 2491-2500.

Hodych, J. P. and G. R. Dunning (1992). "Did the Manicouagan impact trigger the end-of-Triassic extinction." Geology **20**(1): 51-54.

Hoskin, P. W. O. and U. Schaltegger (2003). The composition of zircon and igneous and metamorphic petrogenesis. Reviews in Mineralogy and Geochemistry: Zircon. J. M. Hanchar and P. W. O. Hoskin, Mineralogical Society of America. **53:** 27-62.

Hourigan, J. K., P. W. Reiners, et al. (2005). "U-Th zonation-dependent alpha-ejection in (U-Th)/He chronometry." Geochimica Cosmochimica Acta **69**(13): 3349-3365.

House, M. A., K. A. Farley, et al. (2000). "Helium chronometry of apatite and titanite using Nd-YAG laser heating." Earth and Planetary Science Letters **183**: 365-368.

Longerich, H. P., D. Gunther, et al. (1996). "Laser ablation inductively coupled plasma mass spectrometric transient signal data acquisition and analyte concentration calculation." Journal of Analytical Atomic Spectrometry **9**: 899-904.

Manning, C. E. (1994). "The solubility of quartz in H_20 in the lower cryst and upper mantle." Geochimica Cosmochimica Acta **58**(22): 4831-4839.

Min, K. W., R. Mundil, et al. (2000). "A test for systematic errors in 40Ar/39Ar geochronology through comparison with U/Pb analysis of a 1.1-Ga rhyolite." Geochimica et Cosmochimica Acta **64**(1): 73-98.

Nasdala, L., M. Zhang, et al. (2003). Spectroscopic methods applied to zircon. Reviews in Mineralogy and Geochemistry. J. M. Hanchar and P. W. O. Hoskin, Mineralogical Society of America. **53:** 427-467.

Peucat, J. J., R. Capdevila, et al. (2005). "The Eglab massif in the West African Craton (Algeria), an original segment of the Eburnean orogenic belt: petrology, geochemstry, and geochronology." Precambrian Research **136**: 309-352.

Ramezani, J., S. A. Bowring, et al. (2005). "The manicouagan impact melt rock: A proposed standard for the intercalibration of U-Pb and $^{40}Ar/^{39}Ar$ isotopic systems." Geochimica Cosmochimica Acta **69**: A321.

Reiners, P. W., I. H. Campbell, et al. (2005). "(U-Th)/(He-Pb) double dating of detrital zircons." American Journal of Science.

Sano, Y., K. Terada, et al. (2002). "High mass resolution ion microprobe analysis of rare earth elements in silicate glasses, apatite and zircon: lack of matrix dependency." Chemical Geology **184**: 217-230.

Schoene, B., J. L. Crowley, et al. (in press). "Reassessing the uranioum decay constants for geochronology using ID-TIMS U-Pb data." Geochimica Cosmochimica Acta.

Tagami, T., K. A. Farley, et al. (2003). "(U-Th)/He geochronology of single zircon grains of known Tertiary eruption age." Earth and Planetary Science Letters **207**(1-2): 57-67.

Thomas, J. B., R. J. Bodnar, et al. (2002). "Determination of zircon/melt trace element partition coefficients from SIMS analysis of melt inclusions in zircon." Geochimica Cosmochimica Acta **66**: 2887-2901.

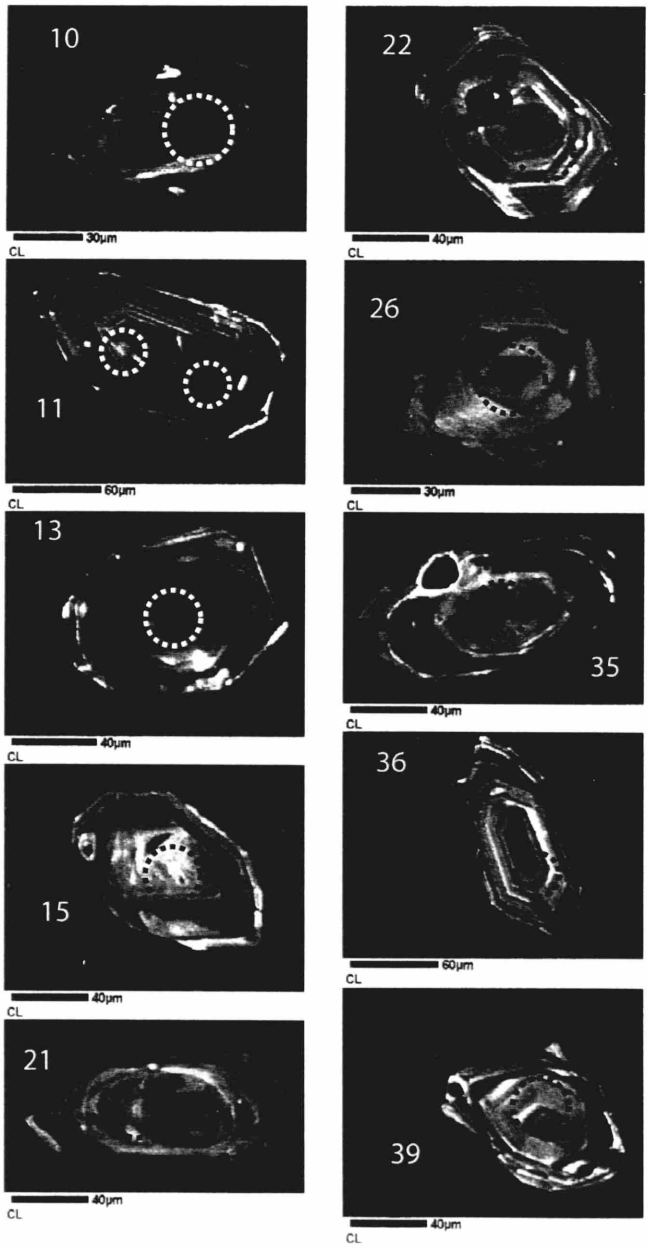
10
30µm
CL
22
40µm
CL
11
60µm
CL
26
30µm
CL
13
40µm
CL
35
40µm
CL
15
40µm
CL
36
60µm
CL
21
40µm
CL
39
40µm
CL

Figure 1a

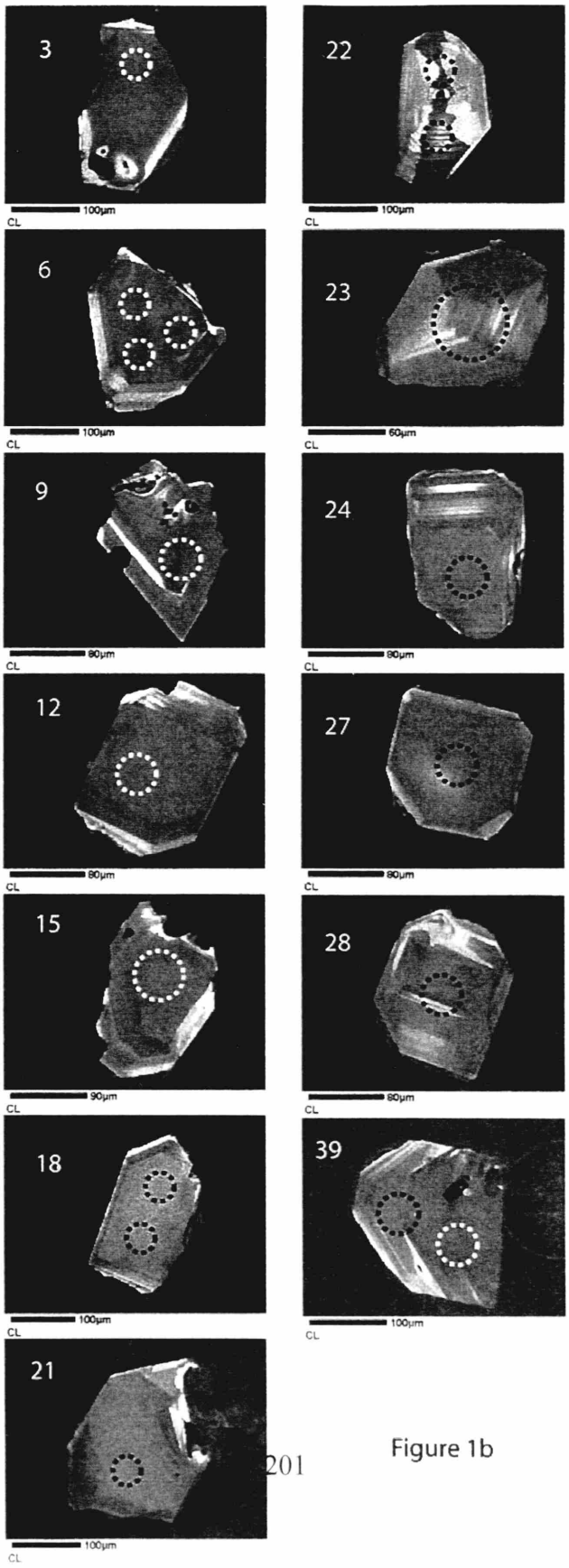
3
100µm
CL
22
100µm
CL
6
100µm
CL
23
60µm
CL
9
80µm
CL
24
80µm
CL
12
80µm
CL
27
80µm
CL
15
90µm
CL
28
80µm
CL
18
100µm
CL
39
100µm
CL
21
100µm
CL

Figure 1b

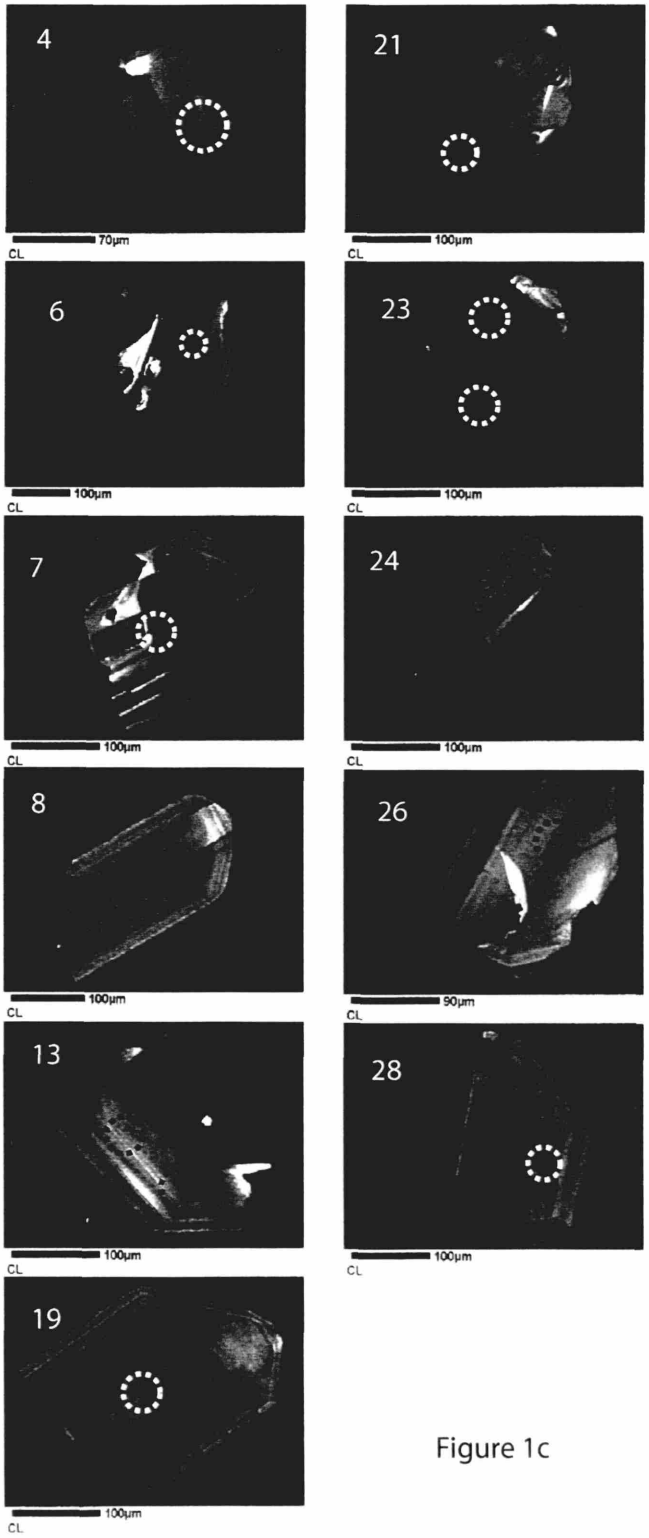
4
70µm
CL
21
100µm
CL
6
100µm
CL
23
100µm
CL
7
100µm
CL
24
100µm
CL
8
100µm
CL
26
90µm
CL
13
100µm
CL
28
100µm
CL
19
100µm
CL

Figure 1c

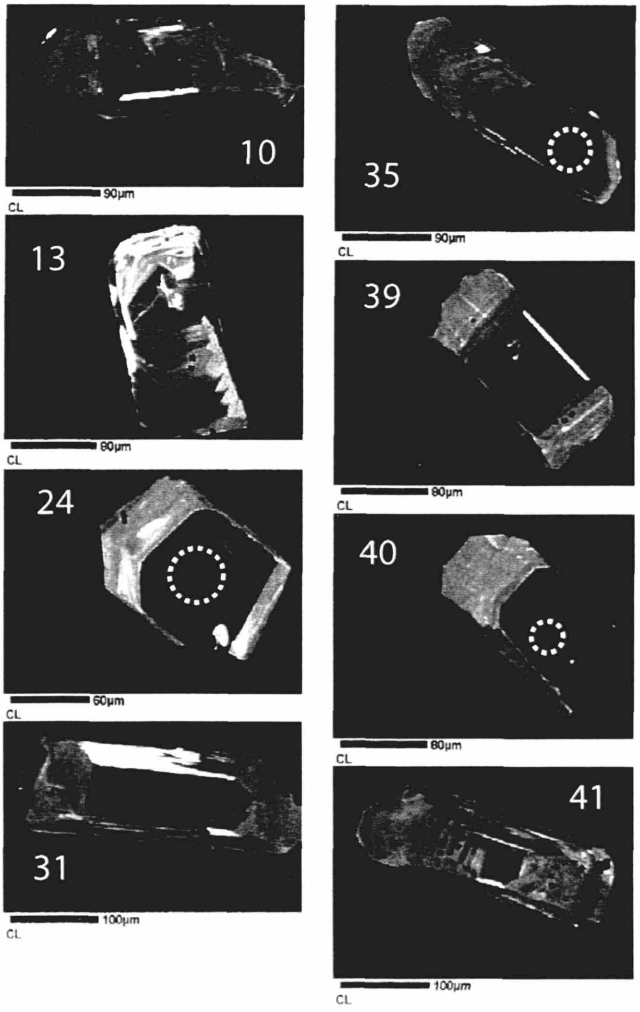
10
90µm
CL
13
80µm
CL
24
60µm
CL
31
100µm
CL
35
90µm
CL
39
80µm
CL
40
80µm
CL
41
100µm
CL

Figure 1d

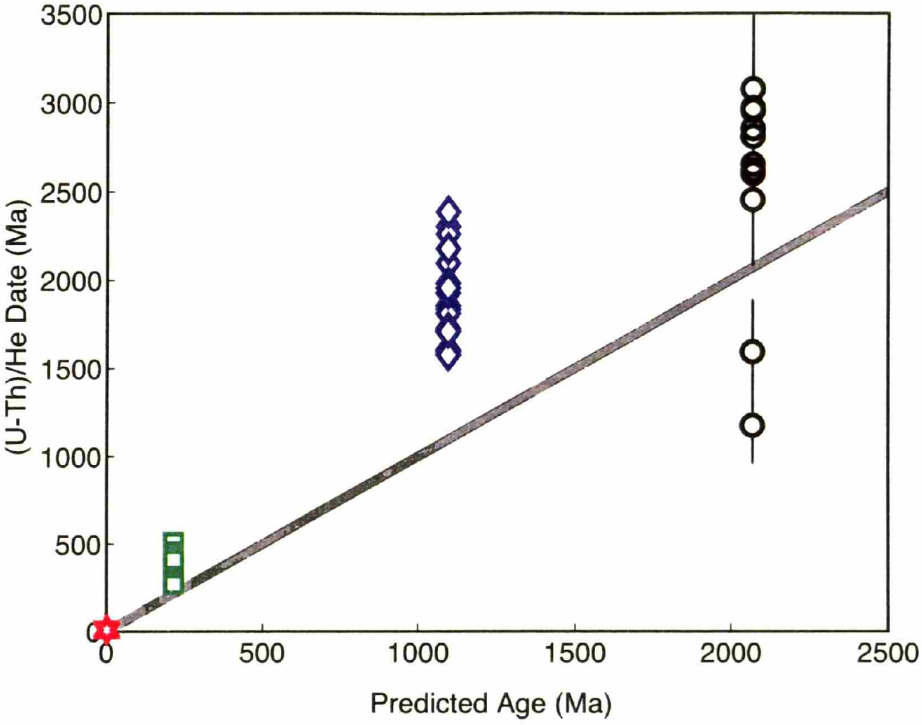
3500
3000
2500
2000
1500
1000
500
0
(U-Th)/He Date (Ma)
0
500
1000
1500
2000
2500
Predicted Age (Ma)

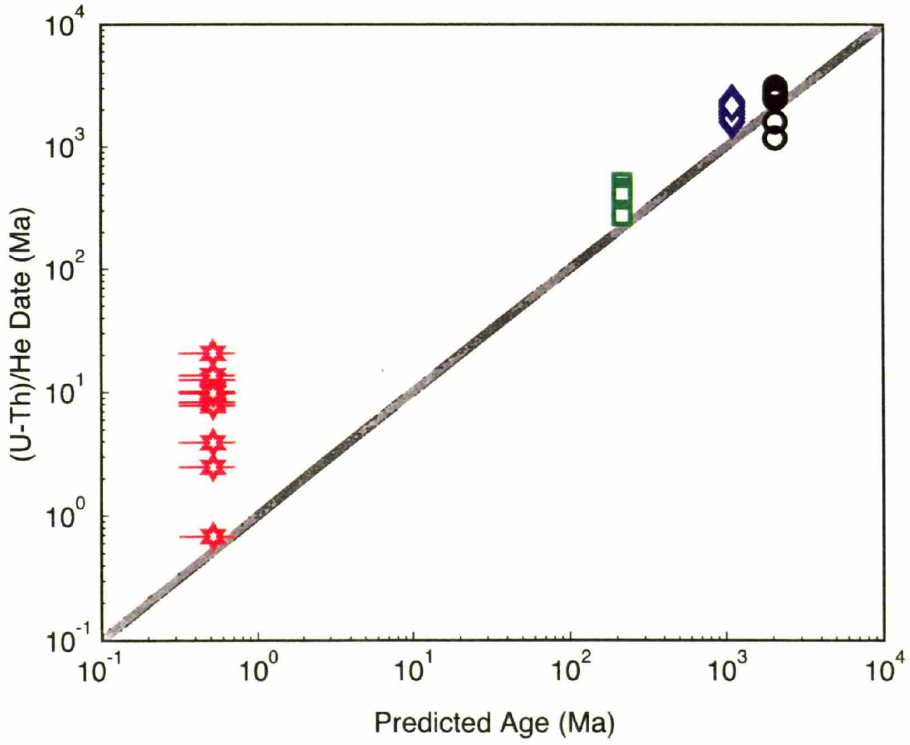
10^4
10^3
10^2
10^1
10^0
10^{-1}
(U-Th)/He Date (Ma)
10^{-1}
10^0
10^1
10^2
10^3
10^4
Predicted Age (Ma)

Figure 2

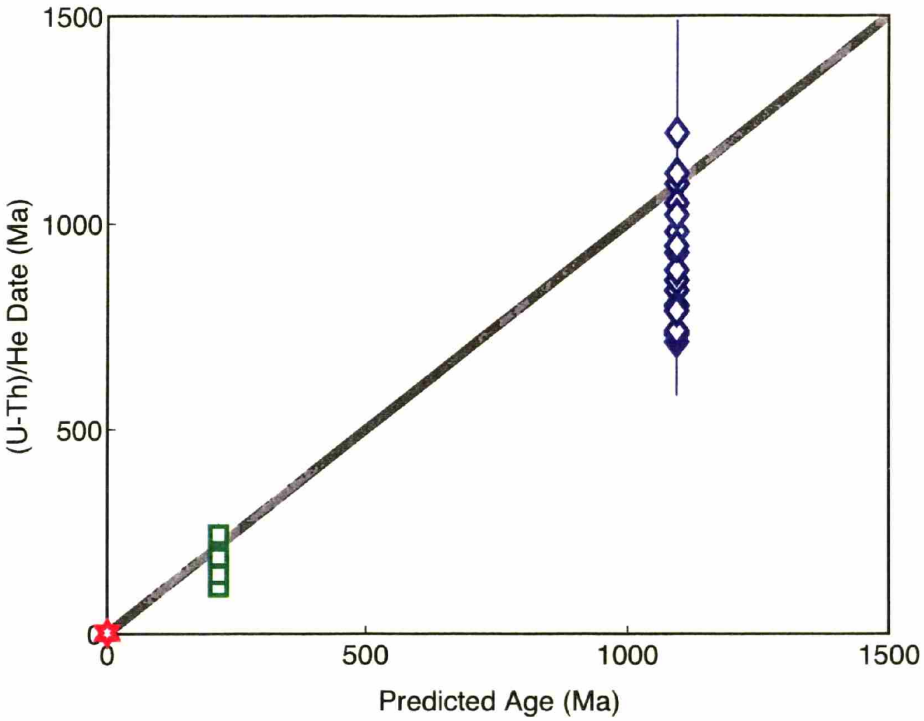
1500
1000
500
0
(U-Th)/He Date (Ma)
0
500
1000
1500
Predicted Age (Ma)

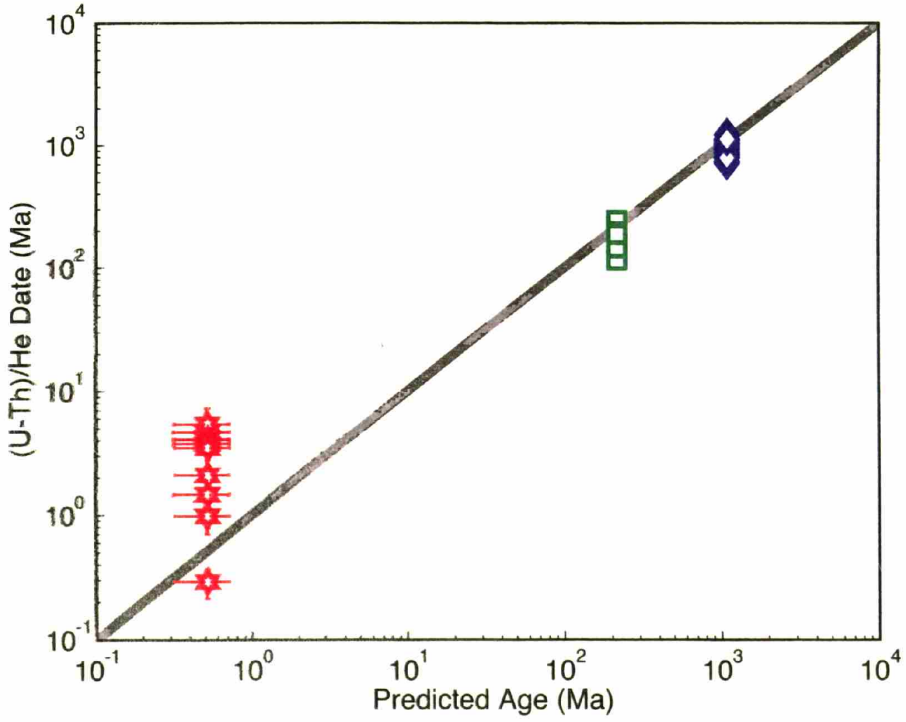
10^4
10^3
10^2
10^1
10^0
10^{-1}
(U-Th)/He Date (Ma)
10^{-1}
10^0
10^1
10^2
10^3
10^4
Predicted Age (Ma)

Figure 3

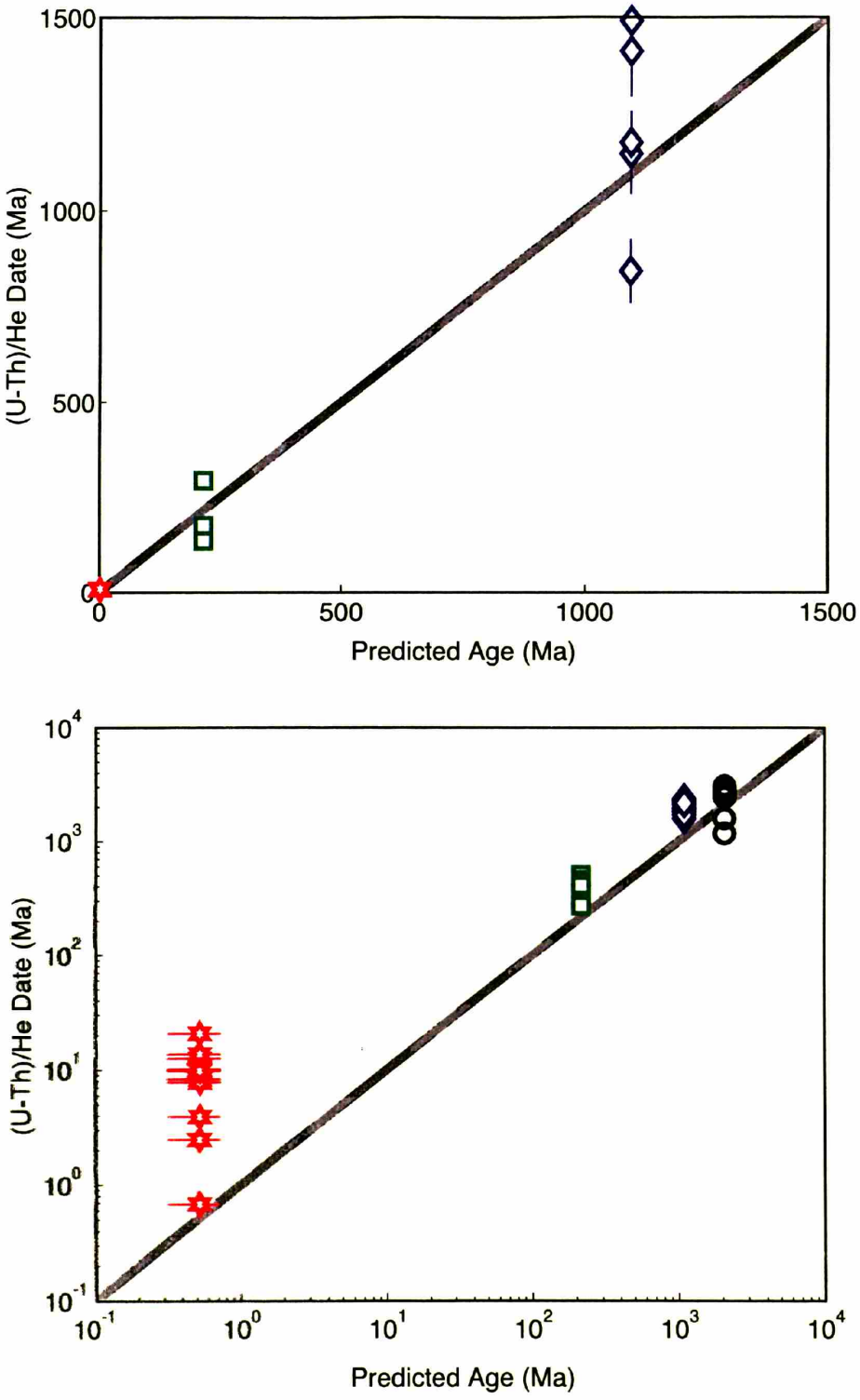
1500
1000
500
0
(U-Th)/He Date (Ma)
0
500
1000
1500
Predicted Age (Ma)
10^4
10^3
10^2
10^1
10^0
10^{-1}
(U-Th)/He Date (Ma)
10^{-1}
10^0
10^1
10^2
10^3
10^4
Predicted Age (Ma)

Figure 4

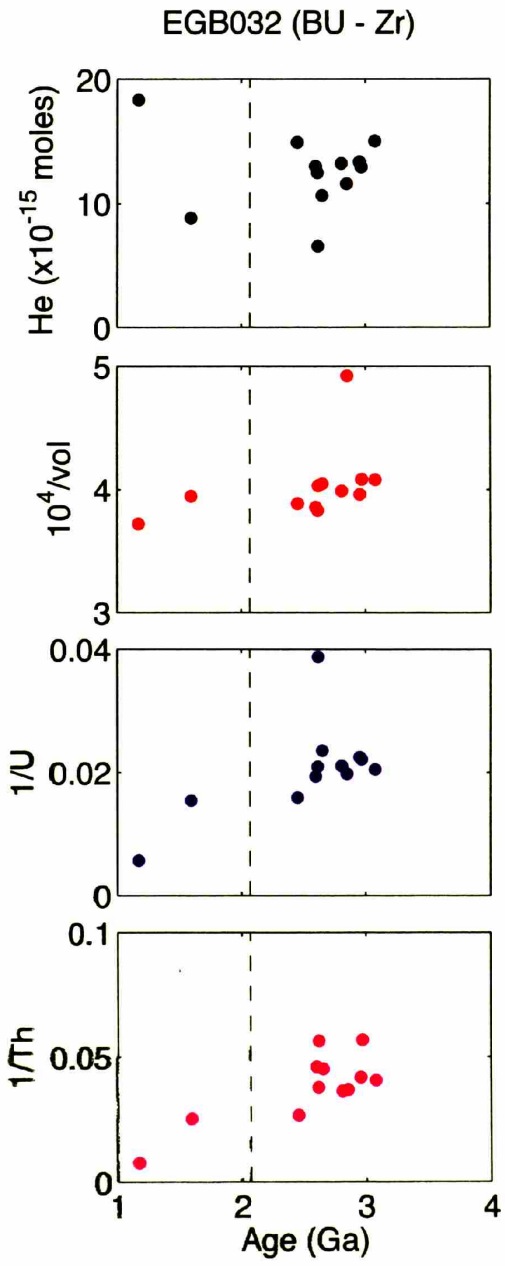
EGB032 (BU - Zr)
He (x10^-15 moles)
20
10
0
10^4/vol
5
4
3
1/U
0.04
0.02
0
1/Th
0.1
0.05
0
1
2
3
4
Age (Ga)

Figure 5a

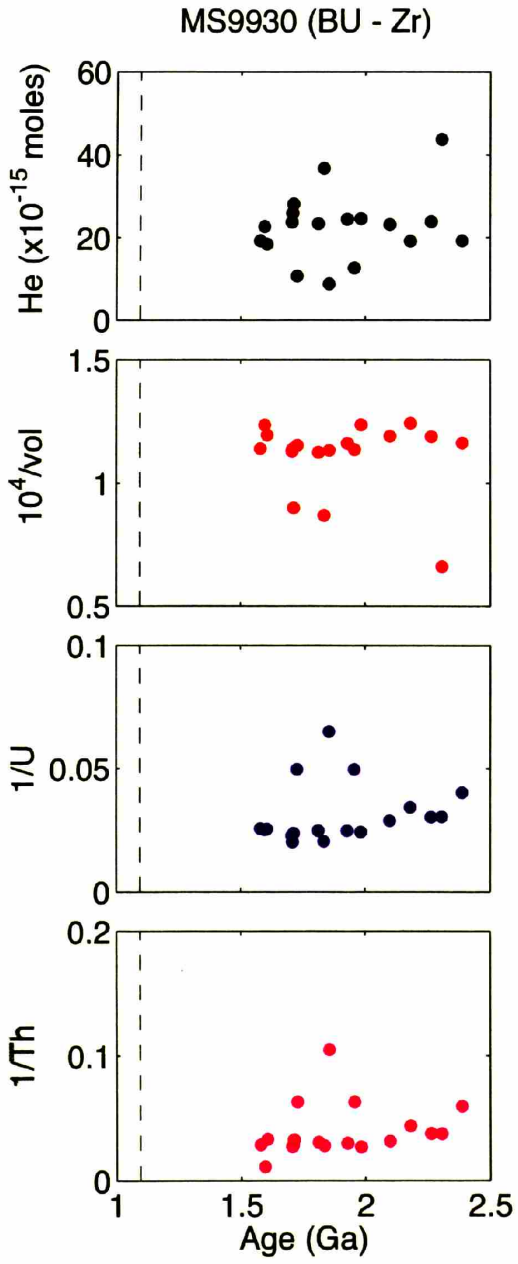
MS9930 (BU - Zr)
He (x10^-15 moles)
60
40
20
0
10^4/vol
1.5
1
0.5
1/U
0.1
0.05
0
1/Th
0.2
0.1
0
1
1.5
2
2.5
Age (Ga)

Figure 5b

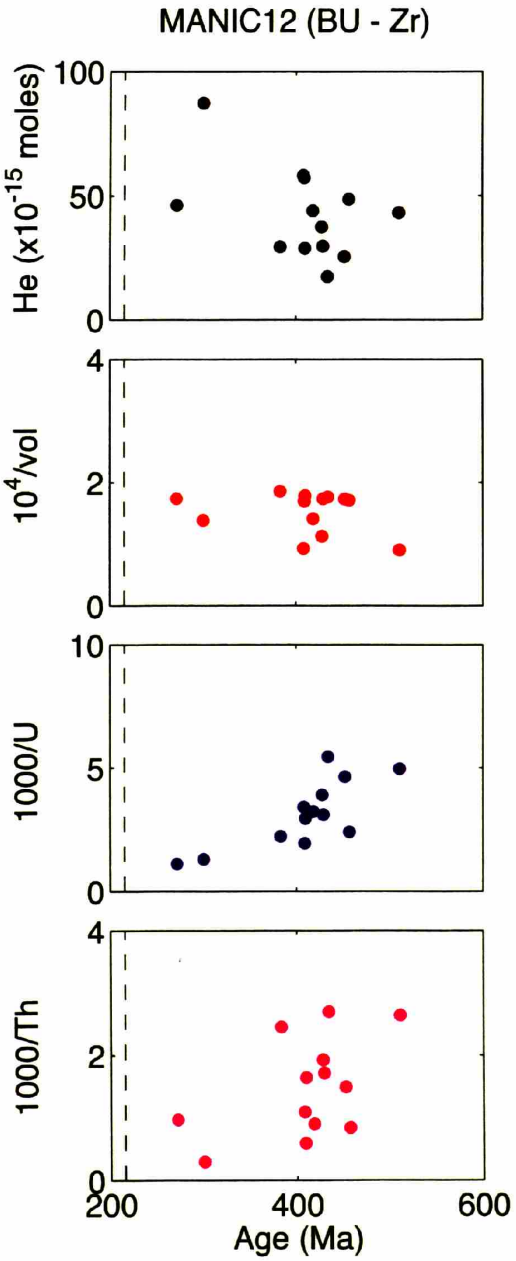
MANIC12 (BU - Zr)
He (x10^-15 moles)
100
50
0
10^4/vol
4
2
0
1000/U
10
5
0
1000/Th
4
2
0
200
400
600
Age (Ma)

Figure 5c

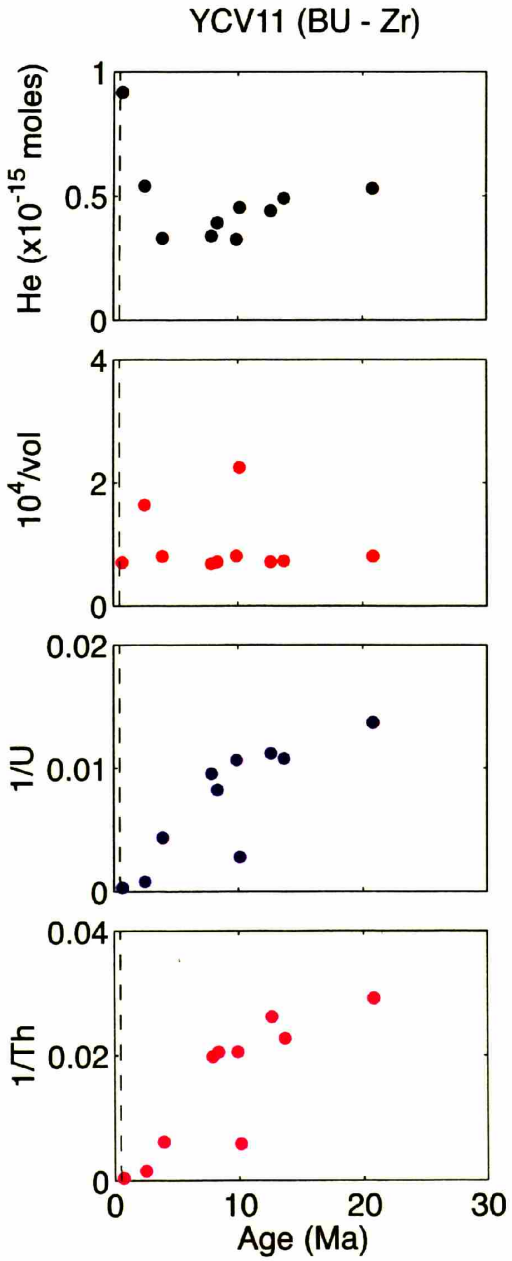
YCV11 (BU - Zr)
He (x10^-15 moles)
1
0.5
0
10^4/vol
4
2
0
1/U
0.02
0.01
0
1/Th
0.04
0.02
0
0
10
20
30
Age (Ma)

Figure 5d

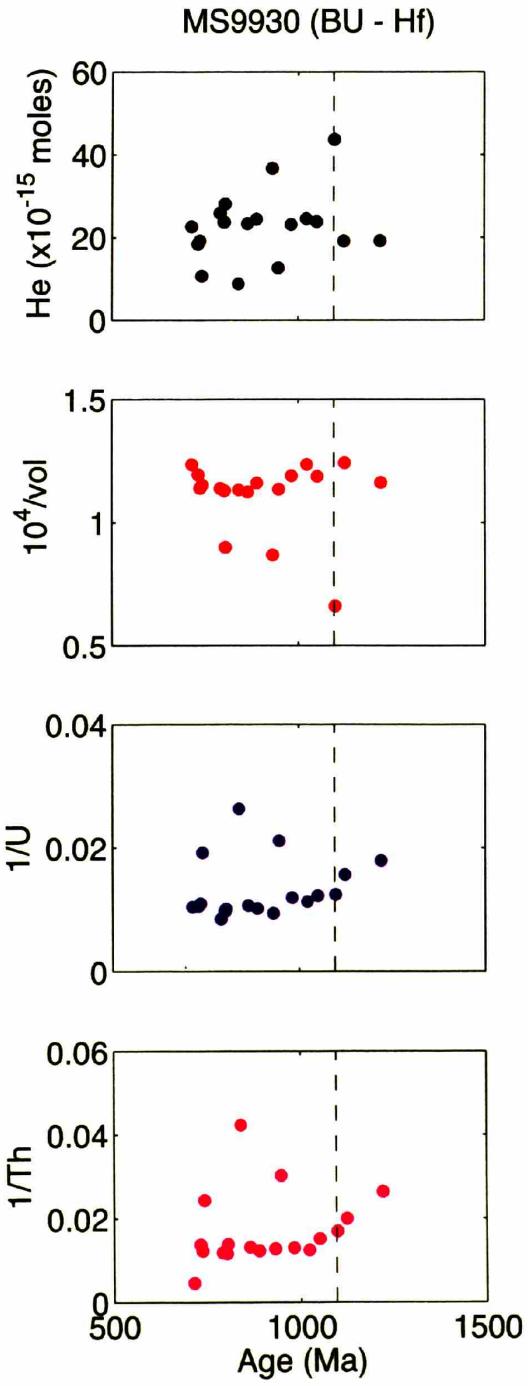
MS9930 (BU - Hf)
He (x10^-15 moles)
60
40
20
0
10^4/vol
1.5
1
0.5
1/U
0.04
0.02
0
1/Th
0.06
0.04
0.02
0
500
1000
1500
Age (Ma)

Figure 6a

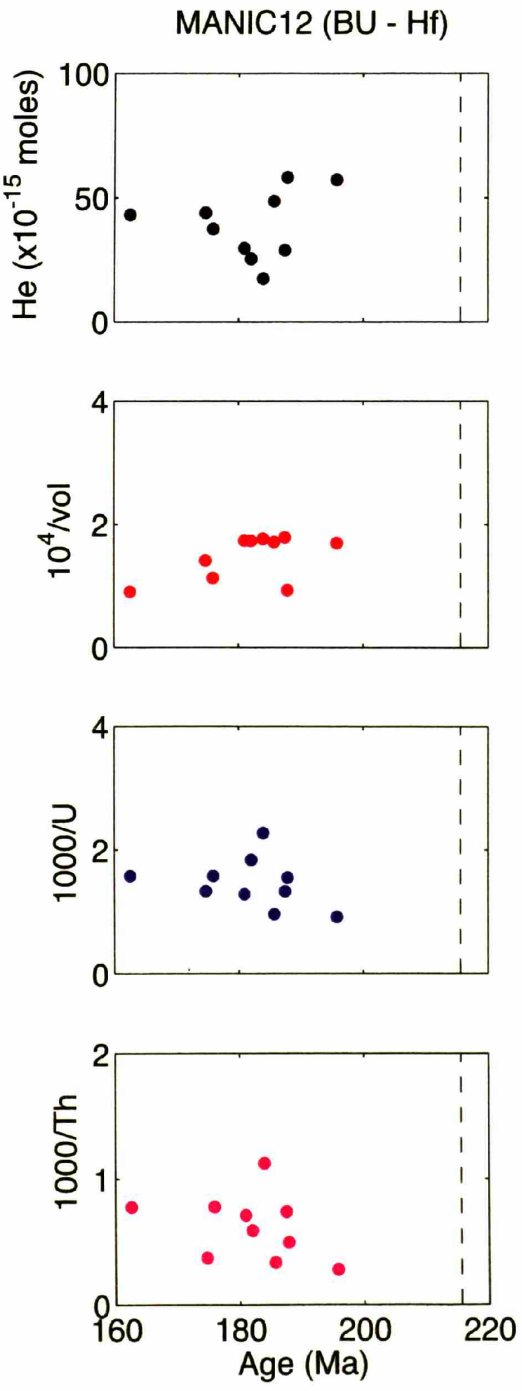
MANIC12 (BU - Hf)
He (x10^-15 moles)
100
50
0
10^4/vol
4
2
0
1000/U
4
2
0
1000/Th
2
1
0
160
180
200
220
Age (Ma)

Figure 6b

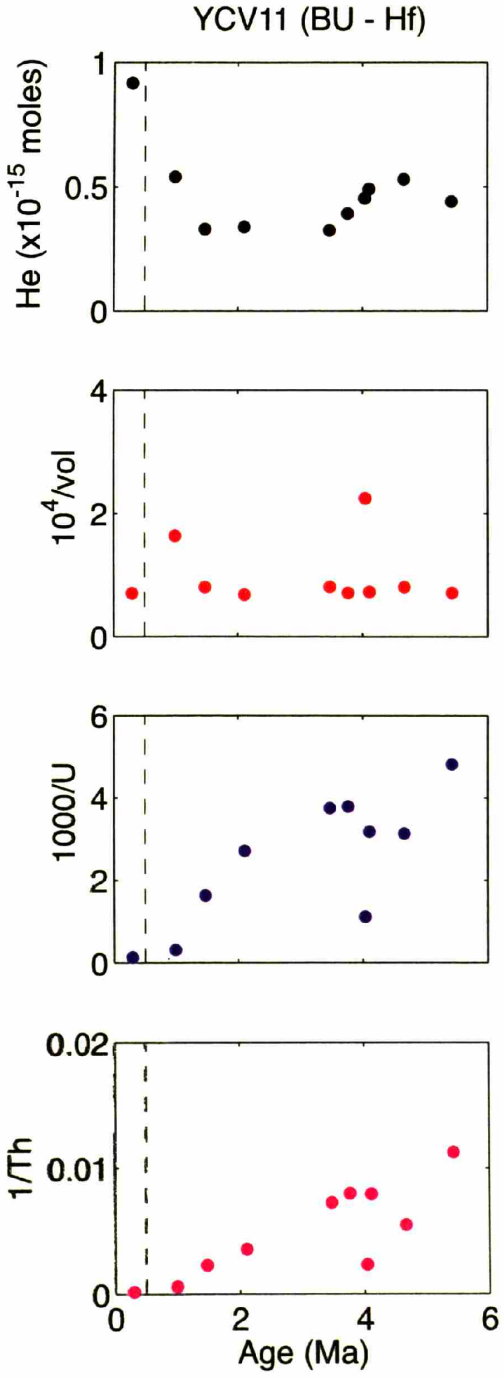
YCV11 (BU - Hf)
He (x10^-15 moles)
1
0.5
0
10^4/vol
4
2
0
1000/U
6
4
2
0
1/Th
0.02
0.01
0
0
2
4
6
Age (Ma)

Figure 6c

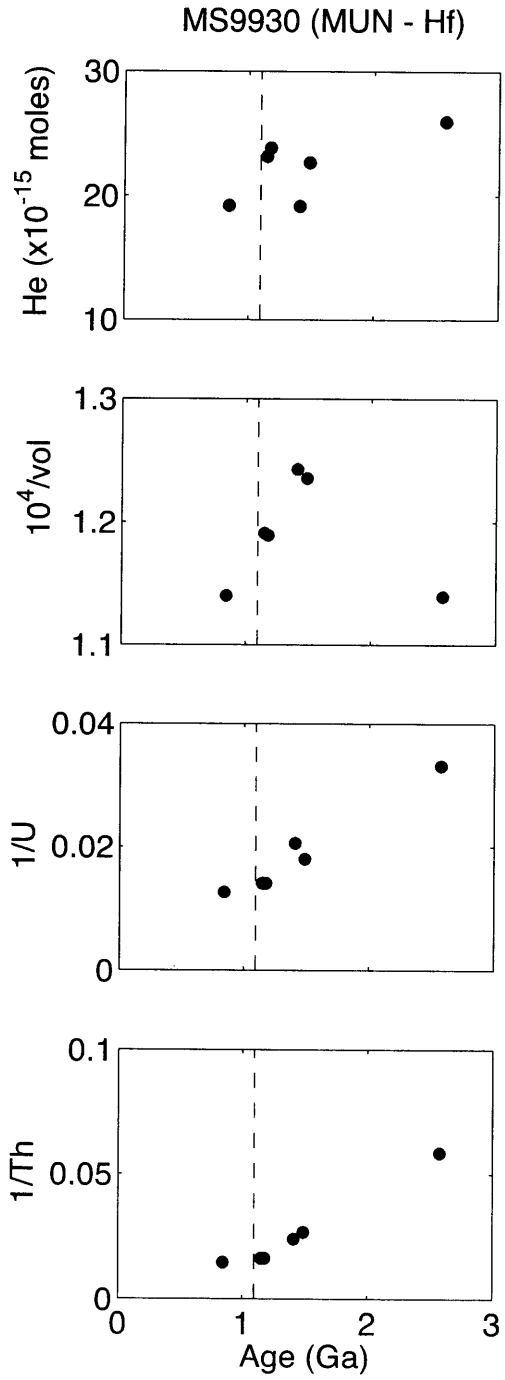
MS9930 (MUN - Hf)
He (x10^-15 moles)
30
20
10
10^4/vol
1.3
1.2
1.1
1/U
0.04
0.02
0
1/Th
0.1
0.05
0
0
1
2
3
Age (Ga)

Figure 7a

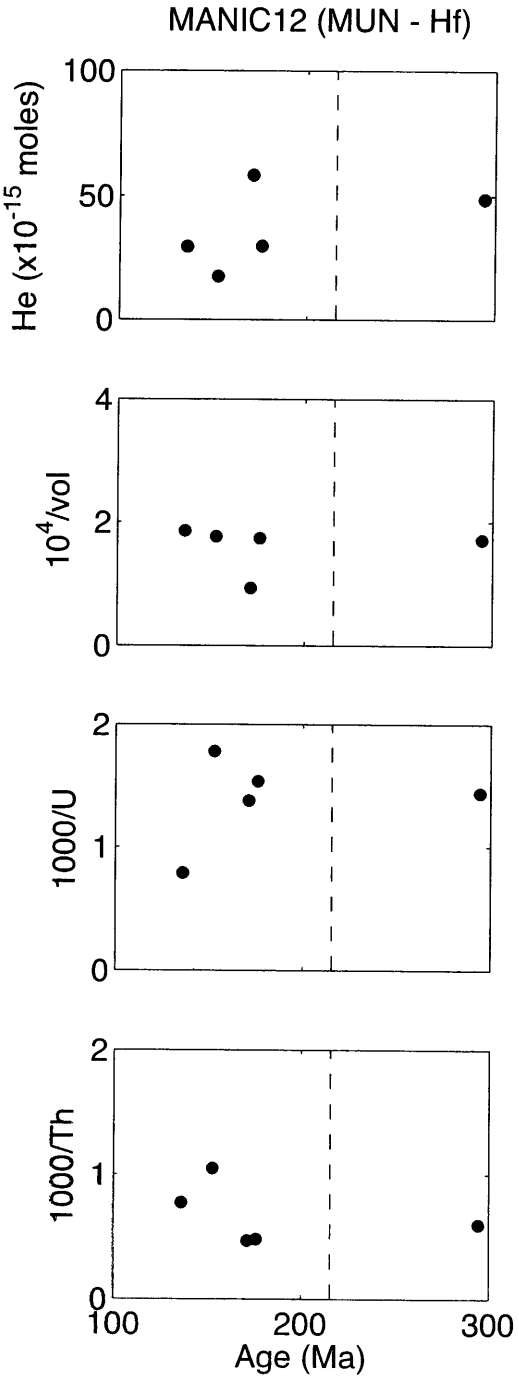
MANIC12 (MUN - Hf)
He (x10^-15 moles)
100
50
0
10^4/vol
4
2
0
1000/U
2
1
0
1000/Th
2
1
0
100
200
300
Age (Ma)

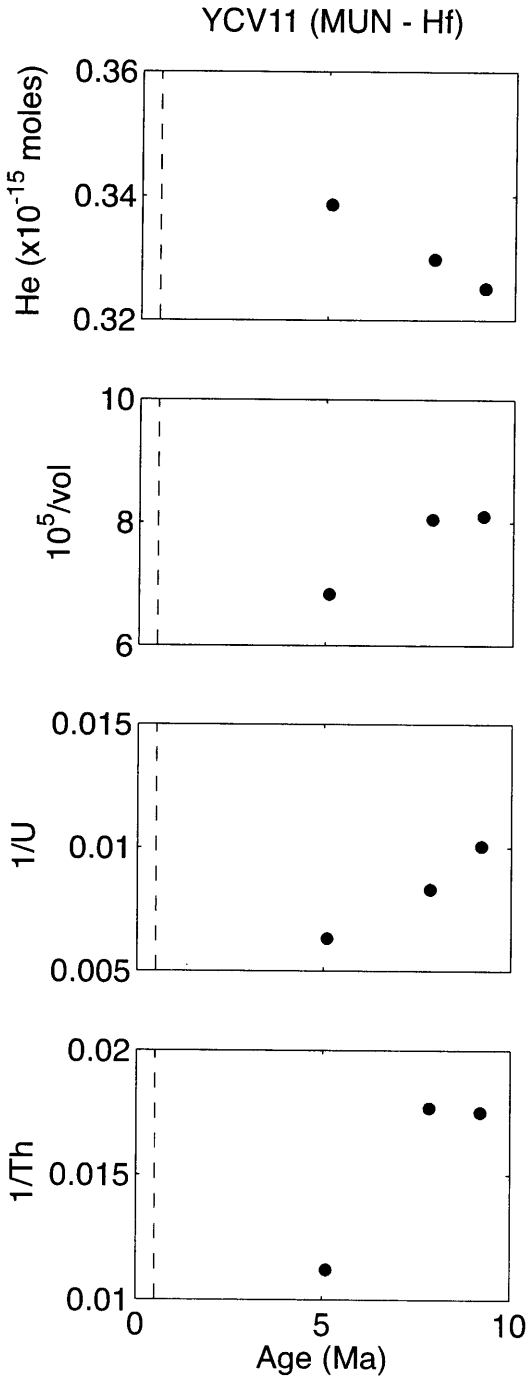
YCV11 (MUN - Hf)
He (x10-15 moles)
0.36
0.34
0.32
10
8
6
10^5/vol
0.015
0.01
0.005
1/U
0.02
0.015
0.01
1/Th
0
5
10
Age (Ma)

Figure 7c

Table 1 Boston University (Zr)

Sample name	hole#	^{4}He (mols x 10^{14})	^{4}He (2s)	volume (μm^3)	vol (2s)	U	U (2s)	Th	Th (2s)	Age (Ma)	Age (2s)
EGB032	10a	0.88	0.008	2533	507	64.8	2.9	39.5	2.3	1593	295
	11a	1.16	0.009	2031	406	50.6	2.3	27.1	1.6	2853	414
	11b	1.29	0.010	2448	490	45.2	2.1	17.6	1.1	2970	416
	12a	1.32	0.010	2506	501	47.5	2.2	27.5	1.7	2811	387
	13a	0.66	0.005	2480	496	25.8	1.2	17.7	1.1	2621	396
	15a	1.50	0.012	2450	490	48.8	2.2	24.6	1.5	3077	412
	21a	1.06	0.009	2469	494	42.5	2.9	22.1	2.0	2654	380
	22a	1.25	0.010	2610	522	47.8	2.0	26.5	1.5	2617	380
	26a	1.30	0.010	2592	518	51.7	2.2	21.8	1.3	2600	418
	35a	1.49	0.012	2573	515	62.9	2.6	37.6	2.1	2454	365
	36a	1.33	0.011	2524	505	44.5	2.1	23.9	1.5	2955	416
	39a	1.83	0.014	2688	538	175.4	7.2	130.3	6.7	1174	214
MS9930	03a	1.91	0.014	8045	161	29.2	0.7	22.9	0.7	2180	48.7
	06a	2.37	0.017	8850	177	44.0	1.0	36.7	1.1	1707	45.8
	06b	2.34	0.018	8887	178	40.4	1.0	32.7	1.0	1812	53.1
	06c	1.92	0.015	8596	172	24.8	0.6	16.8	0.6	2388	51.8
	09a	2.60	0.020	8776	176	49.6	1.4	35.4	1.2	1710	55.3
	12a	2.46	0.018	8084	162	41.2	1.0	37.1	1.1	1983	44.5
	15a	4.4	0.13	15114	302	32.9	0.8	26.7	0.8	2304	71.6
	18a	2.32	0.020	8396	168	34.7	0.8	31.8	0.9	2098	51.1
	18b	2.38	0.019	8409	168	33.0	0.8	26.6	0.8	2262	49.5
	21a	2.27	0.017	8093	162	39.7	0.9	89.9	2.4	1596	34.0
	22a	1.26	0.010	8802	176	20.2	0.6	15.9	0.6	1957	50.8
	22b	1.07	0.008	8673	173	20.2	0.6	15.9	0.6	1728	54.4
	23a	0.88	0.021	8825	177	15.4	0.5	9.5	0.4	1856	50.1
	24a	1.84	0.015	8367	167	39.4	1.1	30.2	1.1	1606	43.3
	27a	1.92	0.014	8772	175	39.1	1.1	34.8	1.2	1577	41.5
	28a	2.45	0.018	8607	172	40.3	1.1	33.5	1.2	1929	55.8
	39a	2.81	0.059	11114	222	42.2	1.2	30.8	1.1	1714	48.7
	39b	3.7	0.09	11507	230	49.0	1.4	35.9	1.3	1835	56.7
MANIC12	04a	2.89	0.022	5589	112	338.9	3.3	609.3	6.5	410	13.4
	06a	2.94	0.023	5376	108	449.4	4.3	407.9	4.5	383	8.8
	07a	2.97	0.024	5751	115	322.2	3.1	583.1	6.2	429	9.6
	08a	5.82	0.043	10757	215	292.8	2.9	914.7	9.3	408	9.2
	13a	4.32	0.032	11046	221	201.6	2.3	378.3	4.7	510	12.5
	13b	3.75	0.028	8851	177	256.0	2.6	519.2	5.6	428	8.8
	19a	4.62	0.037	5751	115	899.2	8.2	1031	11	271	6.0
	21a	4.40	0.032	7073	141	309.5	3.0	1106	11	418	9.9
	23a	8.73	0.064	7209	144	771.1	6.9	3342	32	300	7.0
	23b	5.73	0.043	5892	118	515.3	4.7	1683	16	409	8.2
	24a	2.55	0.021	5775	116	215.4	2.2	670.1	7.0	452	8.0
	26a	1.74	0.015	5657	113	183.3	1.9	370.5	4.2	434	11.2
	28a	4.86	0.038	5838	117	415.7	3.9	1189	12	457	11.7
YCV11	10a	0.033	0.0027	12417	248	229.3	6.6	161.9	5.6	3.9	0.36
	13a	0.034	0.0031	14633	293	104.9	3.1	50.5	1.9	7.8	0.71
	24a	0.092	0.0022	14186	284	3212	25.9	2214	21	0.68	0.022
	31a_a	0.033	0.0019	12341	247	94.0	2.7	48.7	1.8	9.8	0.71
	35a	0.049	0.0021	13720	274	92.8	2.6	44.0	1.6	13.7	0.91
	35b	0.039	0.0032	14021	280	121.6	3.3	48.7	1.7	8.3	0.64
	39a	0.045	0.0012	4448	89	358.5	3.3	170.5	5.5	10.1	0.33
	40a	0.054	0.0028	6103	122	1262	10.6	633.1	6.4	2.5	0.16
	41a_a	0.053	0.0022	12392	248	73.0	2.3	34.3	1.4	20.8	1.10
	41b_a	0.044	0.0026	14014	280	89.4	2.7	38.2	1.5	12.6	0.90

Table 1 Boston University (Hf)

Sample name	hole#	^{4}He (mols x 10^{14})	^{4}He (2s)	volume (μm^3)	vol (2s)	U	U (2s)	Th	Th (2s)	Age (Ma)	Age (2s)
MS9930	03a	1.91	0.014	8045	161	63.9	8.5	50.1	5.3	1121	489
	06a	2.37	0.017	8850	177	103.2	13.8	86.1	9.0	799	361
	06b	2.34	0.018	8887	178	93.6	12.5	75.9	8.0	862	387
	06c	1.92	0.015	8596	172	55.8	7.5	37.8	4.0	1219	543
	09a	2.60	0.020	8776	176	118.2	9.0	84.5	6.4	788	201
	12a	2.46	0.018	8084	162	88.6	11.8	79.9	8.4	1021	442
	15a	4.4	0.13	15114	302	80.4	10.7	58.8	6.2	1096	476
	18a	2.32	0.020	8396	168	83.8	11.2	76.7	8.1	980	427
	18b	2.38	0.019	8409	168	81.6	10.9	65.8	6.9	1049	457
	21a	2.27	0.017	8093	162	95.8	12.8	216.8	22.8	713	260
	22a	1.26	0.010	8802	176	47.3	5.0	33.1	3.5	945	331
	22b	1.07	0.008	8673	173	52.0	5.5	41.1	4.3	740	268
	23a	0.88	0.021	8825	177	38.0	4.0	23.6	2.5	837	304
	24a	1.84	0.015	8367	167	94.6	7.2	72.6	5.5	730	182
	27a	1.92	0.014	8772	175	91.2	7.0	81.3	6.2	735	187
	28a	2.45	0.018	8607	172	97.9	7.5	81.4	6.2	887	224
	39a	2.81	0.059	11114	222	99.0	7.6	72.3	5.5	802	207
	39b	3.7	0.09	11507	230	106.4	8.1	78.1	5.9	929	241
MANIC12	04a	2.89	0.022	5589	112	753	60	1354	94	187.5	22
	06a	2.94	0.023	5376	108	1209	96	1097	76	145.3	20
	07a	2.97	0.024	5751	115	778	62	1408	98	180.9	21
	08a	5.82	0.043	10757	215	645	51	2015	140	187.9	21
	13a	4.32	0.032	11046	221	634	50	1286	89	162.5	20
	13b	3.75	0.028	8851	177	634	50	1286	89	175.9	21
	19a	4.62	0.037	5751	115	2144	170	2458	171	115.3	15
	21a	4.40	0.032	7073	141	752	60	2689	187	174.7	19
	23a	8.73	0.064	7209	144	1091	86	3564	248	243.1	26
	23b	5.73	0.043	5892	118	1091	86	3564	248	195.8	22
	24a	2.55	0.021	5775	116	544	43	1694	118	182.0	20
	26a	1.74	0.015	5657	113	440	35	890	62	184.0	22
	28a	4.86	0.038	5838	117	1041	83	2978	207	185.7	21
YCV11	10a	0.033	0.0027	12417	248	613	129	433	63	1.5	0.68
	13a	0.034	0.0031	14633	293	369	62	280	29	2.1	0.69
	24a	0.092	0.0022	14186	284	7513	1084	5180	574	0.29	0.077
	31a_a	0.033	0.0019	12341	247	267	38	138	15	3.5	1.00
	35a	0.049	0.0021	13720	274	314	58	126	19	4.1	1.64
	35b	0.039	0.0032	14021	280	264	49	125	19	3.8	1.53
	39a	0.045	0.0012	4448	89	898	167	427	65	4.0	1.57
	40a	0.054	0.0028	6103	122	3181	459	1596	177	1.0	0.28
	41a_a	0.053	0.0022	12392	248	319	54	183	19	4.7	1.54
	41b_a	0.044	0.0026	14014	280	208	35	89	9	5.4	1.90

Table 1 Memorial University (Hf)

Sample name	hole#	^{4}He (mols x 10^{14})	^{4}He (2s)	volume (μm^3)	vol (2s)	U	U (2s)	Th	Th (2s)	Age (Ma)	Age (2s)
MS9930	03a	1.91	0.014	8045	161	48.6	4.9	41.5	4.2	1413	118
	09a	2.60	0.020	8776	176	30.2	3.0	17.1	1.7	2576	193
	18a	2.32	0.020	8396	168	71.1	7.1	61.2	6.1	1148	104
	18b	2.38	0.019	8409	168	71.1	7.1	61.2	6.1	1177	82
	21a	2.27	0.017	8093	162	55.54	5.554	37.31	3.7312	1491	116
	27a	1.92	0.014	8772	175	79.2	7.9	68.1	6.8	843	42
MANIC12	04a	2.89	0.022	5589	112	726.6	72.66	2140	214	171	13
	06a	2.94	0.023	5376	108	1265	126.5	1293	129.28	136	12
	07a	2.97	0.024	5751	115	651.5	65.15	2084	208.36	176	13
	26a	1.74	0.015	5657	113	561.9	56.19	951.8	95.182	152.4389	12
	28a	4.86	0.038	5838	117	696.2	69.62	1673	167.28	294.5333	22
YCV11	10a	0.033	0.0027	12417	248	120.3	12.03	56.55	5.6546	7.8	0.87
	13a	0.034	0.0031	14633	293	158.3	15.83	89.25	8.9252	5.1	0.66
	31a_a	0.033	0.0019	12341	247	99.45	9.945	57.1	5.7102	9.2	1.1

Table 2 Hafnium concentrations (weight percent oxide)

MS9930	HfO2 (wt%)	MANIC12	HfO2 (wt%)	YCV11	HfO2 (wt%)
3	0.798	4	0.794	10	0.954
3	0.805	4	0.853	10	1.031
6	0.889	6	1.004	10	1.080
6	0.815	7	0.795	13	1.117
9	0.805	8	0.903	13	0.931
12	0.779	8	0.779	31	1.002
15	0.827	13	0.845	31	0.912
15	0.810	19	0.827	40	1.073
18	0.831	21	0.906	40	1.085
18	0.899	23	0.666	41	1.127
21	0.893	23	0.874	41	1.110
21	0.817	23	0.866	41	1.029
24	0.868	24	0.986	41	1.033
24	0.801	24	0.920		
27	0.851	26	0.891		
28	0.851	28	0.904		
39	0.834	28	0.869		
39	0.807				
39	0.888				

All uncertainties are ~5%, and only include counting statistics, not uncertainties in standard compositions